SPIN DEPENDENT TRANSPORT IN FERROMAGNETIC PARTICLES

A Thesis
Presented to
The Academic Faculty

by

Wenchao Jiang

In Partial Fulfillment
of the Requirements for the Degree
Doctor of Philosophy in the
School of Physics

Georgia Institute of Technology
August 2014

SPIN DEPENDENT TRANSPORT IN FERROMAGNETIC PARTICLES

Approved by:

Professor Dragomir Davidovic,
Advisor
School of Physics
Georgia Institute of Technology

Professor Arun Gokhale
School of Material Science and
Engineering
Georgia Institute of Technology

Professor Phillip N. First
School of Physics
Georgia Institute of Technology

Professor Michael Pustinik
School of Physics
Georgia Institute of Technology

Professor Zhigang Jiang
School of Physics
Georgia Institute of Technology

Date Approved: 1 May 2014

To my parents Zhibin Jiang and Xiaofang Jiang,

and people who believed in me.

ACKNOWLEDGEMENTS

I sincerely thank my advisor Dr. Dragomir Davidović for his trust, advice, and support. I would still be stuck somewhere in my research without his guidance. He helps me to establish a right attitude toward things more than just physics, for which I am very grateful. I appreciate all my committee members: Dr. Phillip First, Dr. Arun Gokhale, Dr. Zhigang Jiang, and Dr. Michael Pustinik for their time and consideration. I thank Dr. Roman Grigoriev for his Electricity & Magnetism class, and Dr. Kurt Wiesenfeld for his Statistical Mechanics class. Those courses are very useful to me in how to solve problems. I thank Dr. Zangwill for his help in my course selections. Specially, I thank Dr. Zhigang Jiang for taking his time to give me advice about my career.

Great thanks to Dr. Felipe Tijiwa Birk, and Dr. Christopher Malec for their lab training and help in the research. Thanks to the hard work of Patrick Gartland, Dogukan Deniz, Bradley Elkus, and Shuai Sun, so my lab work becomes a lot easier. I would like to thank my colleagues and friends Dr. Yike Hu, Dr. Lede Xian, Wenlong Yu, Feng Wang, James Palmer, Zelei Guo, Xunchi Chen, Alex Lesov, Yuntao Li, Di Chen, Chen Yang, and Shangguo Zhu for their help in my research, advice in my career, and company in my life. I thank all my friends in China, US, and other countries for their support over the years.

I would like to acknowledge Scott Centers for repairing our equipment, Keith Garner for keeping the water and lights on, Jeffery Sullivan for the computers, Victoria Speights and Mary Helen Hayes for all the financial work, and Sam Mize for the machining and bolts. I would like to thank all the custodians for keeping our lab and this building clean. I thank Mel Pinson at Air Gas for all the conveniences he

provided.

Last but not least, I want to to thank my parents for defining who I am.

TABLE OF CONTENTS

LIST OF TABLES

LIST OF FIGURES

SUMMARY

Spintronics is an emerging technology that arises from the interplay between spin of the charge carrier and the magnetic property of the materials. The miniaturization of spintronic devices requires a deep understanding of ferromagnetic materials at the nanometer scale. This thesis studies the properties of ferromagnetic particles (2-5nm in diameter) using electron transport measurements. A technique to fabricate nanoparticle devices and incorporate microwave in the electron tunneling measurement of the particles is presented. Repeated microwave pulses can directly excite the magnetization of the particles without heating the electrons. Results of the transport measurements on Co particles will be discussed, which demonstrate that electron tunneling through a ferromagnetic particle can induce magnetization excitations in that particle. A physical model regarding the mesoscopic fluctuations is presented to address the current driven magnetization noise. Numerical simulations based on that model are performed to explain the experimental data and validate the model. Electron transport measurements on Ni, Fe, and $Ni_{80}Fe_{20}$ are conducted. The hysteretic behaviors of the particles in presence of electron tunneling have strong material dependence, which is mainly due to the magnetic shape anisotropy. Electron tunneling is a main source of magnetization noise, while other sources still need to be identified. Some data we collected from literature will be included in this thesis as an appendix.

CHAPTER 1

INTRODUCTION

The discovery of giant-magnetoresistance (GMR) in 1988 initiated the research and development in spin-based electronics, i.e., spintronics.[3, 30] Grünberg and Fert were awarded the 2007 Nobel Prize in Physics for this discovery. A typical GMR-based spin valve device has two ferromagnetic layers spaced by a thin normal metal layer. The resistance of the spin valve changes when the relative orientations of the magnetization in the two ferromagnetic layers changes between "parallel" and "anti-parallel" states. If the normal metal layer is replaced by a thin insulating layer, we can build a magnetic tunnel junction (MTJ) where tunneling-magnetoresistance (TMR) is the main effect.[47, 63] The successful application of GMR and TMR in the Hard-Disk-Drive industry has greatly increased the data storage density of the disk, which has enabled the Big-Data era. In addition to being a measurement probe in GMR and TMR, electronic current can also manipulate the magnetization orientation of the ferromagnetic layers, through a process known as "spin-transfer-torque" (STT). STT has been theoretically investigated,[84, 85, 7] and experimentally realized in both metallic multilayer devices and MTJ devices.[94, 89, 64, 48] STT opens the possibility to build small, fast, and energy-efficient magnetic devices.

As the size of spintronics devices approaches the quantum mechanical regime, it is necessary to fundamentally understand the magnetic mechanism that governs the dynamics in those devices. A lot of research has been done on ferromagnetic particles at the nanometer scale. Micro-SQUID measurements on single Co nanoparticles have been performed by Wernsdorfer's group to understand the magnetic anisotropy

and magnetic switch (a sudden change in the magnetization direction) in ferromagnetic nanoparticles.[106, 41, 42, 91, 90] Electron tunneling measurements on single Co nanoparticles were conducted by Ralph's group, which revealed rich quantum mechanical phenomena, such as abundance of low-energy excitations and hysteresis in energy levels.[31, 19] Theoretical effort has been devoted to this field to address those experimental findings.[18, 15, 14, 50, 102, 62] Similar to STT, electron transport, which was solely used as a probing method in those works, can also perturbs the system. For example, Ref. [10] predicts that electron transport can fully randomize the magnetization in a ferromagnetic particle. However, those prior studies ignore the perturbation from electron transport and are limited to Co particles. Therefore, we perform electron tunneling experiments on different ferromagnetic particles to understand the interaction between electron transport and magnetization dynamics.

In this thesis, I will present the study of Co, Ni/Ni-61 isotope, and Permalloy($Ni_{80}Fe_{20}$) particles using electron transport measurements. Coupling between magnetization dynamics and electron transport will be a main focus. Microwave induced magnetic excitation is also included. Magnetic anisotropy modeling and numerical simulation of the magnetization dynamics in the presence of electron transport will be discussed. In this chapter, I will briefly introduce some background information about ferromagnetic particles and transport measurements.

1.1 Single Electron Tunneling

1.1.1 Coulomb Blockade

The device we studied is usually composed of a ferromagnetic particle attached between two aluminum leads via aluminum oxide tunnel barriers. It can be modeled as in Figure 1.1. The tunnel barrier can be seen as a small capacitor with a very large "tunnel resistance" (R_L, R_R). It is worth noting here that the resistance of

a tunnel barrier is fundamentally different from that of a regular resistor. Tunneling through the barrier is an elastic process: the electron wavefunction is partially transmitted/reflected at the barrier, while the energy of the electron does not change. The tunnel resistance is inversely proportional to the transmission probability, which decreases exponentially with the thickness of the barrier. A bias voltage is applied across the tunnel junction to enable electron transport. Let n and n_0 be the number of electrons in the particle at finite V and $V = 0$, respectively. Under an applied voltage V, the charge of the particle will split to the left and right plate of the capacitors: $-(n - n_0)e = Q_L + Q_R$. Also, the total voltage drop across C_L and C_R is V: $Q_L/C_L - Q_R/C_R = V$. The total charging energy stored in two capacitors is $Q_L^2/2C_L + Q_R^2/2C_R$. Since the electron keeps its energy when tunneling through the barrier, the work done by the battery VQ_L should be included in the total energy. Therefore, the total energy $U(n, V)$ of a particle with n electrons can be written as[52, 34]:

$$U(n, V) = \frac{[(n - n_0)e + VC_L]^2}{2C} + \sum_{i=1}^{n} E_i(\vec{B}) \tag{1.1}$$

Here, e is the elementary charge, $C = C_R + C_L$. Due to the 3D confinement of the particle, the electrons occupy discrete electron-in-a-box states, which will be referred to as energy levels in this thesis. $\sum_{i=1}^{n} E_i(\vec{B})$ sums over all the occupied energy levels under an applied magnetic field $\vec{B}$.

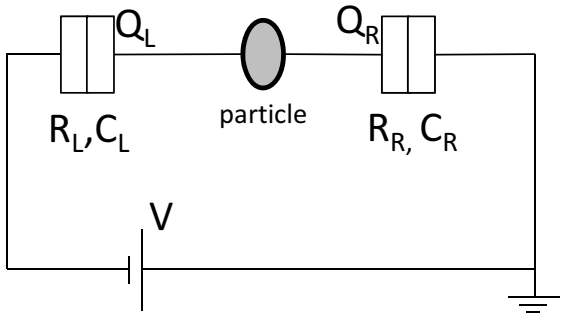

Figure 1.1: Model of a nanoparticle device

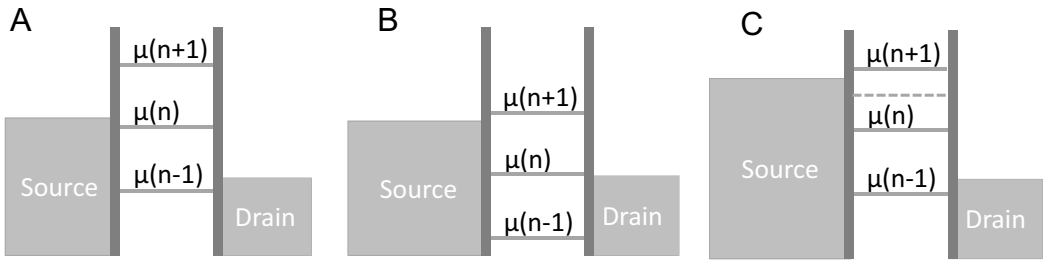

Figure 1.2: A and B: Schematics for the two scenarios of the onset of electron tunneling. C: Schematic about the electron tunneling at high bias region. The dashed line denotes a transition involving an excited state.

The energy required to add one electron onto the particle (electrochemical potential) $\mu(N)$ can thus be defined:

$$\begin{aligned} \mu(n) &= U(n+1) - U(n) \\ &= \tfrac{e}{C}[(n - n_0 + \tfrac{1}{2})e + C_L V)] + E_{n+1}(\vec{B}) \end{aligned} \tag{1.2}$$

There are two scenarios when the sequential tunneling process starts at low temperature ($k_B T \ll e^2/C$). The first is that an electron tunnels onto the particle from one lead, then tunnels off the particle through the other lead (Figure 1.2A). Alternatively, the conduction can be initiated by an electron tunneling off the particle through one lead, which lowers the electrochemical potential of the particle to $\mu(n)$. Then, another electron can tunnel onto the particle from the other lead (Figure 1.2B). Assuming that the electrons always tunnel onto the particle from the left lead and tunnel off of the particle to the grounded right lead, the conditions for electron tunneling to occur are $\mu_L = eV > \mu(n)$ for the first scenario (Figure 1.2A) and $\mu_R = 0 < \mu(n)$ for the second scenario (Figure 1.2B). It can be easily seen that, when ramping up the bias voltage from zero, there will be no tunneling current until one of those two conditions is met. This suppression of electron tunneling before the bias voltage reaches a certain threshold is defined as Coulomb Blockade (CB), as shown in the blue region in Figure 1.3 around zero bias. The voltage threshold corresponding to the onset of electron tunneling is referred to as CB threshold.

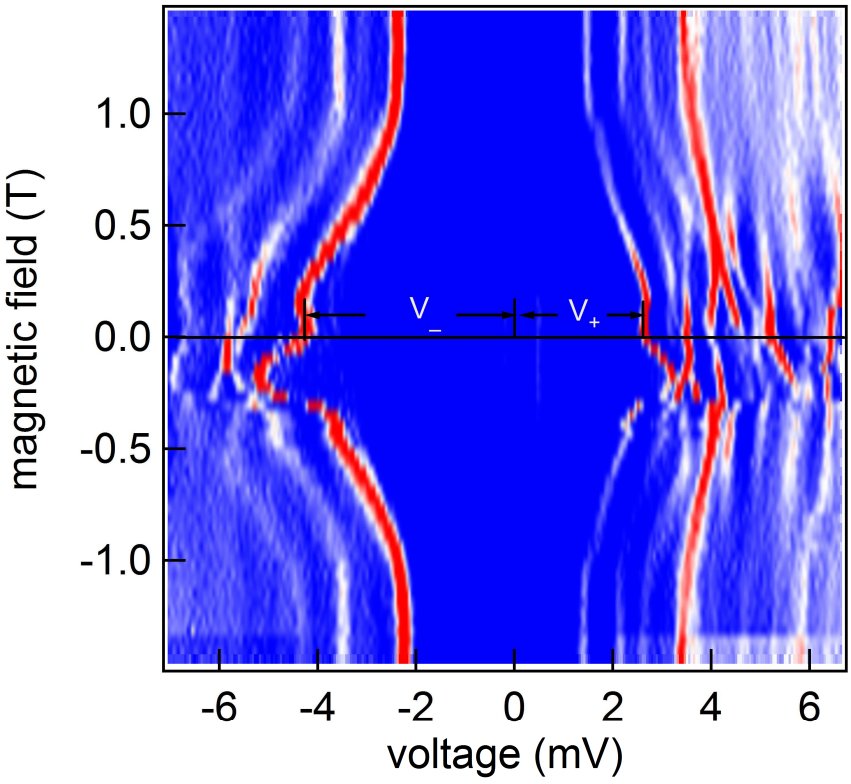

Figure 1.3: An example of electron tunneling spectrum. Blue(red) color represents low(high) conductance.

To observe the CB effect in experiments, there are two requirements that need to be fulfilled. The first is that the thermal fluctuations should be much less than the charging energy, namely $k_BT \ll e^2/C$. The second is that the tunnel barrier is opaque enough so that quantum fluctuations in the number of electrons on the particle n is much weaker than the change of n due to tunneling current I.[1, 5, 52] For a tunnel resistance R, the typical charging time is $\Delta t = RC$. From the Heisenberg uncertainty principle, we obtain $\Delta E \Delta t > h$. Thus, in order to have $\Delta E \ll e^2/C$, the tunnel resistance R should be much larger than the resistance quantum h/e^2.

After the bias voltage overcomes the CB threshold, sequential electron tunneling occurs, where electrons tunnel onto(off) the particle, then tunnel off(onto) it one after another. As the bias voltage further increases, excited states with $n+1$ electrons could participate in the electron tunneling process, as shown in Figure 1.2C. Usually, this will lead to changes in the tunneling current, which enables explorations of the excited states using electron tunneling spectroscopy. The magnetic field dependence of the energy levels involved in electron tunneling can be obtained from the evolution of corresponding voltages (e.g., the red/white lines in Figure 1.3).

From Eq. 1.2, a bias voltage V can increase the electrochemical potential of the particle by eVC_L/C. It means that the energy scale of the particle is magnified by C/C_L in the reading from the voltage source. The capacitance ratio $c = C_L/C_R$ needs to be obtained to correct this effect. It can be done by looking at the CB threshold for positive and negative bias voltage. Let's take Figure 1.3 as an example, the CB threshold at zero field for positive and negative bias are V_+ and V_-, respectively. Based on the model in Figure 1.1 and the conditions for the onset of electron tunneling, it can be easily shown that $c = |V_+/V_-|$. Thus, the voltage at positive (negative) bias divided by $1 + c$ $(1 + 1/c)$ is the electron energy in the particle in unit of eV.

1.1.2 Tunneling current

As we discussed before, a tunneling current will be observed once the bias voltage satisfies the condition for electron tunneling. Here I will briefly review the calculation of that tunneling current and its relation with the bias voltage.[2, 5, 52]

Let's start by assuming an electron tunnels from the left lead onto one energy level of the particle with n electrons, which changes the particle from state $|\varphi>$ to a final state $|\varphi'>$. The energy difference involved in this transition is $\Delta E_p^j = e/C[(n-n_0+1/2)e+C_LV)]+E_j(\vec{B})$, where j is the index of the energy level that the electron tunnels onto. At the same time, the left lead will change from $|\psi>$ to $|\psi'>$ with an energy difference $\Delta E_L = E_{\psi'} - E_\psi - eV$, where eV is the charging energy of that electron. Using the Fermi's golden rule, the tunneling rate from $|\varphi>$ to $|\varphi'>$ can be written as[52]:

$$\gamma^+_{L,\varphi'\varphi} = \frac{2\pi}{\hbar}\sum_{\psi\psi'}\rho_L(\psi)|\left\langle\psi'\varphi'|\mathcal{H}_t|\psi\varphi\right\rangle|^2\delta(\Delta E_p+\Delta E_L) \tag{1.3}$$

$\rho_L(\psi)$ is the density of states in the left lead, $\mathcal{H}_t$ is the Hamiltonian describing the tunneling process. The lead is very large so the electrons in it follow the Fermi-Dirac distribution. Because one electron is removed from the left lead to the particle, ΔE_L is equivalent to the energy of the removed electron. Since the Fermi level of the left lead is eV, the maximum of ΔE_L should be eV. Therefore, sum over all the initial states $|\psi>$ and bringing the form of $\mathcal{H}_t$ into Eq. 1.3 will give us[52]:

$$\gamma^+_{L,\varphi'\varphi} = \sum_j \Gamma_{L,j}|<\varphi'|a^\dagger_{pj}|\varphi>|^2 f_L^+ \tag{1.4}$$

where $\Gamma_{L,j}$ is the electron tunneling rate from the left lead to the jth energy level of the particle, and $a^\dagger_{pj}$ is the electron creation operator for that level. $f_L^+ = f(\Delta E_p^j - eV)$ is the Fermi distribution function of lead L(left), with $f_L^- = f(eV-\Delta E_p^j)$. Similarly, the rate for transition from $|\varphi'>$ to $|\varphi>$ by an electron tunneling off the particle to

the left lead is:

$$\gamma^{-}_{L,\varphi\varphi'} = \sum_j \Gamma_{L,j} | < \varphi' | a^{\dagger}_{pj} | \varphi > |^2 f^{-}_{L} \tag{1.5}$$

The same argument can be applied to the right lead if we replace eV with 0, because the Fermi level for the right lead is 0(grounded). Now, let $P(\varphi)$ denote the probability to find the particle in $|\varphi>$ state. When the system reaches equilibrium, $\partial P(\varphi)/\partial t = 0$, and $I_L + I_R = 0$. Thus, the tunneling current can be represented by either I_L or I_R. Easily, we can write I_l as

$$\begin{aligned} I_l &= e \sum_{\varphi\varphi'} [\gamma^{+}_{l,\varphi'\varphi} P(\varphi) - \gamma^{-}_{l,\varphi'\varphi} P(\varphi')] \\ &= e \sum_j \sum_{\varphi\varphi'} \Gamma_{l,j} | < \varphi' | a^{\dagger}_{pj} | \varphi > |^2 [f^{+}_{l} P(\varphi) - f^{-}_{l} P(\varphi')] \\ &= e \sum_j \sum_{\varphi\varphi'} \Gamma_{l,j} | < \varphi' | a^{\dagger}_{pj} | \varphi > |^2 [f^{+}_{l} [P(\varphi) + P(\varphi')] - P(\varphi')], \quad f^{+}_{l} + f^{-}_{l} = 1 \end{aligned} \tag{1.6}$$

Here, $l = L, R$ stands for the left and right lead, respectively. From Eq. 1.6, it is clear that the tunneling current is strongly dependent on the Fermi distribution function of the lead. For instance in the left lead, $f^{+}_{L} = [1+\exp((\Delta E^{j}_{p} - eV)/k_B T)]^{-1}$. At low temperature where $k_B T$ is much smaller than the average spacing η between the particle's energy levels, only energy levels with $\Delta E^{j}_{p} - eV < 0$ contribute to electron tunneling. As the bias voltage slowly increases so that another level $j+1$ is available for tunneling, i.e., $e/C[(n - n_0 - 1/2)e + C_L V)] + E_{j+1}(\vec{B}) < eV$, the current will make a jump. The current step in the IV curve resembles the shape of $f(\Delta E^{j+1}_{p} - eV)$ as eV rises across ΔE^{j+1}_{p}. The size of the step depends on the tunneling rate $\Gamma_{L,j+1}$ and the matrix element $| < \varphi' | a^{\dagger}_{pj+1} | \varphi > |^2$.

1.2 Magnetic Hamiltonian

A ferromagnetic particle with a diameter of 2-5nm is usually a single domain magnet. The magnetic energy of a particle comes from three parts: magnetic shape anisotropy (MSA), magnetocrystalline anisotropy (MCA), and mesoscopic anisotropy.

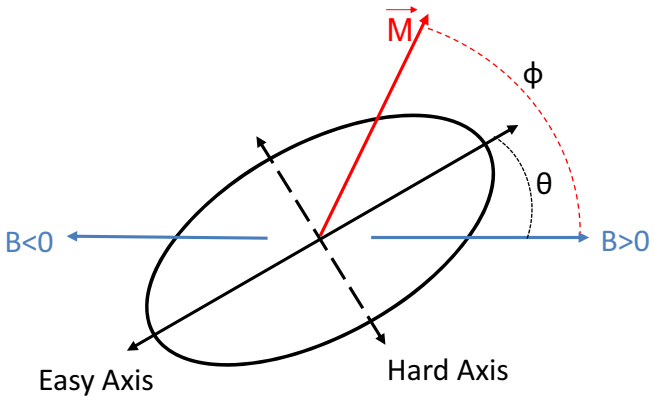

Figure 1.4: Sketch of Stoner-Wohlfarth Model. $\vec{M}$ represents the magnetization.

Let's first take a look at the shape anisotropy due to the long range interactions between magnetic dipoles inside the particle. Assuming $T = 0$K and the magnetization is saturated and uniformly distributed in the particle, the internal *demagnetization field* $H_d = -\hat{N} \cdot \vec{M}$ leads to a self-energy $E_d = 1/2\mu_0 V \vec{M}\hat{N}\vec{M}$ of the magnet, where $\hat{N}$ is the *demagnetization tensor* and $\vec{M}$ is the magnetization vector. Since $\hat{N}$ is determined by the shape of the magnet, E_d is often referred to as the "magnetic shape anisotropy". Like a lot of things in physics, the $\hat{N}$ of an arbitrary shaped magnet is very difficult to calculate. So, most of the time, we assume an ellipsoid shape for a particle to simplify the problem. In this case, the three axes of the ellipsoid are also the principle axes of $\hat{N}$, which reduces $E_d = 1/2\mu_0 V \vec{M}\hat{N}\vec{M}$ to $E_d = 1/2\mu_0 V(N_x M_x^2 + N_y M_y^2 + N_z M_z^2)$ with $M_x^2 + M_y^2 + M_z^2 = M_s^2$, where M_s is the saturation magnetization. $N_{x,y,z}$ are the three eigenvalues for the tensor $\hat{N}$, and $N_x + N_y + N_z = 1$ in SI units. A detailed calculation of $N_{x,y,z}$ is available in Ref. [6]. From the expression of E_d, it is easy to see that the magnetization of a particle would prefer the axis with the lowest N to minimize the self-energy. That axis with the lowest N value is usually referred to as the "easy axis", while the axis with the largest N is the "hard axis". In an ellipsoid magnet, the longest axis is usually the "easy axis" and the shortest axis is the "hard axis". Because of the constrain

$N_x + N_y + N_z = 1$, only two out of the three eigenvalues are independent. If we further assume that the ellipsoid is prolate (one long axis and two equal short axes), the *demagnetization tensor* $\hat{N}$ becomes "uniaxial" and $E_d = 1/2\mu_0(N_h M_h^2 + N_e M_e^2)$ with $2N_h + N_e = 1, M_h^2 + M_e^2 = M_s^2$. $N_{h(e)}$ is the eigenvalue for hard axis(easy axis) and $M_{h(e)}$ is the projected magnetization on hard axis(easy axis). Using the symbols in Figure 1.4, we obtain $E_d = 1/4\mu_0 M_s^2 V[(N_h + N_e) - (N_h - N_e)\cos^2(\phi - \theta)]$. By adding the energy associated with the applied magnetic field, we reach the Stoner-Wohlfarth (SW) model,[88] which is widely used to describe the magnetic field dependence of the magnetization in such a uniaxial magnetic system:

$$E = -K_u V \cos^2(\phi - \theta) - M_s B V \cos(\phi) \tag{1.7}$$

Here, $K_u = 1/4\mu_0 M_s^2(N_h - N_e)$ is the "uniaxial anisotropy constant", B is the magnitude of the applied magnetic field, and V is the volume of the magnet (Figure 1.4). In this model, the magnetization within the particle has a constant magnitude and only rotates according to the applied field. The magnetization is in an equilibrium direction if the magnetic energy is minimized, meaning the first derivative of the energy respect to the direction of magnetization is zero:

$$\frac{\partial E}{\partial \phi} = K_u V \sin 2(\phi - \theta) + M_s B V \sin(\phi) = 0 \tag{1.8}$$

If the magnetic field is small and not parallel or perpendicular to the easy axis, Eq. 1.7 has two energy minima (Figure 1.5A to C). As the magnetic field sweeps from positive to negative in Figure 1.5, the stable minimum evolves into a meta-stable state (with an energy larger than the other energy minimum). However, the magnetization cannot change to the stable state because of the energy barrier lies in between the meta-stable and stable state. When the applied field exceeds a certain value, the meta-stable state and the energy barrier disappear. At this point, the magnetization will jump to the stable state, which is often referred to as a "switch" or "reversal"

of the magnetization. The field at which the magnetization switch happens is called the "coercive field " or "switching field". For a given θ, the switching field can be obtained from Eq. 1.8. The solution is:

$$B_{sw} = \frac{1}{2}\mu_0 M_s \frac{(1 - t^2 + t^4)^{1/2}}{1 + t^2} \tag{1.9}$$

where $t = \tan^{1/3}\theta$. If the magnetic field is in parallel with the easy axis ($\theta = 0, \pi$), the magnetization will not rotate before it switches. At the other extreme condition where the field is perpendicular to the easy axis ($\theta = 1/2\pi, 3/2\pi$), the magnetization will only rotate according to the magnetic field without making a switch.

In ferromagnetic particles, the number of total spins S_0 is a preferred quantity to use instead of V. If we assume that the spins in a particle forms a "big" vector $\vec{S}$ with a constant magnitude $S_0 = M_s V/g\mu_B, g \approx 2$ (macro-spin assumption), we can rewrite Eq. 1.7 to:

$$\mathcal{H}(\vec{B}, \vec{S}) = \frac{K_s}{S_0}\vec{S}\hat{N}\vec{S} - g\mu_B \vec{S} \cdot \vec{B} \tag{1.10}$$

where $K_s \approx \mu_0 \mu_B M_s$ is the MSA constant, and μ_B is the Bohr magneton. $\vec{S}$ is the total spin vector $\left\{\hat{S}_x, \hat{S}_y, \hat{S}_z\right\}$ with $\hat{S}_{x,y,z}$ being the spin operator.

Compared to the magnetic shape anisotopy, the magnetocystalline anisotropy (MCA) appears to be more complicated, especially in particles. The bulk MCA for hexagonal system (Co) and cubic system (Ni, Fe) is very well described in Ref. [49]. To write the MCA in terms of S_0, one can use the following equations:

$$\mathcal{H}(\vec{S}) = -S_0[K_1\gamma^2 + K_2\gamma^4] \tag{1.11}$$

$$\begin{aligned}\mathcal{H}(\vec{S}) = S_0[K_1(\alpha^2\beta^2 + \alpha^2\gamma^2 + \gamma^2\alpha^2 + \beta^2\gamma^2 + \gamma^2\beta^2) + \frac{K_2}{6}(\alpha^2\beta^2\gamma^2 \\ + \alpha^2\gamma^2\beta^2 + \beta^2\alpha^2\gamma^2 + \beta^2\gamma^2\alpha^2 + \gamma^2\beta^2\alpha^2 + \gamma^2\alpha^2\beta^2)]\end{aligned} \tag{1.12}$$

where $\alpha, \beta, \gamma = \hat{S}_x/S_0, \hat{S}_y/S_0, \hat{S}_z/S_0$ and $K_{1,2}$ are the MCA constants. Eq. 1.11 is for hexagonal system (Co) and Eq. 1.12 is for cubic system (Ni, Fe). The MCA constants $K_{1,2}$, saturation magnetization M_s, and MSA constant K_s for Co, Ni, Fe, and Permalloy are available in Appendix A.

The MCA originates from the single electron anisotropy (exchange energy) caused by the spin-orbit (SO) interactions. The MCA is a mean contribution from all the singly occupied electrons, so MCA per atom is very small compared to the single electron anisotropy, which is on the order of $\hbar/\tau_{SO} \approx 1\text{mV}$ (τ_{SO} is the spin-orbit scattering lifetime).[15] Since the SO interaction is sensitive to bulk-symmetry, facet-orientations, and the shape of the particle, a satisfactory calculation of MCA is very difficult to achieve even in bulk.[87] It suggests that the $K_{1,2}$ derived from the bulk value should not be directly applied in the magnetic Hamiltonian of particles. On the other hand, Ref. [11] finds out that for Co, Ni, and Fe particles with diameters of 2-5nm, the contribution from MCA to the total magnetic anisotropy is insignificant. Thus, we can safely drop the MCA in the calculation of magnetic anisotropy for particles.

The symmetry of a ferromagnetic particle can be broken by nonmagnetic disorder or defects on its boundary. A mesoscopic anisotropy is created through the scattering of the electron orbital wave functions on those disorder or defects.[11] The mesoscopic anisotropy does not scale with S_0 in a particle. In Co particle with about 10^2 atoms and larger Ni, and Fe particles, the mesoscopic anisotropy has a dominant contribution to the total anisotropy.

During the electron transport measurement, single electron tunnels onto and off the particle sequentially. Since a single electron is more likely to tunnel into a minority state,[19, 14, 50] the electron tunneling-on event tends to reduces the total spin in a particle to $S_0 - 1/2$. Therefore, the sequential tunneling events will make the number of spins in the particle hop between S_0 and $S_0 - 1/2$. The single electron

anisotropy associated with the tunneled on/off electron will contribute to the total magnetic anisotropy of the particle. Because of the chaotic electron wave function inside the particle, that contribution creates fluctuations in the magnetic anisotropy of the particle, which is referred to as "magnetic anisotropy fluctuations" or "mesoscopic fluctuations".[11, 15, 19, 98] The contribution from the single electron anisotropy varies weakly among different transition metals, so the effects of the mesoscopic fluctuations on the magnetic dynamics in a particle is determined by the relative strength of particle's total magnetic anisotropy. Nevertheless, the mesoscopic fluctuations show the coupling between the magnetic system and the electronic environment. Thus, the magnetic Hamiltonian needs modification to accommodate mesoscopic fluctuations. The simplest way is to make the K_s in the SW model dependent on the number of electrons in the particle [19, 50, 44, 45], then we can rewrite Eq. 1.10 into:

$$\mathcal{H}(\vec{B}, \vec{S}, n) = \frac{K_n}{S_0}\vec{S}\hat{N}\vec{S} - 2\mu_B\vec{S}\cdot\vec{B} \tag{1.13}$$

where n is the number of electrons in the particle, and K_n varies between n and $n+1$-electron states. Note that the MSA does not fluctuate during electron tunneling process, the mesoscopic fluctuations is mainly caused by the MCA being perturbed by the tunneled on/off electron.

1.3 Magnetization Dynamics

Different methods can be used to measure the magnetization dynamics, such as optical magnetometry, superconducting quantum interference device, and Mössbauer spectroscopy. Since the experimental data only reflect the "average" behavior of system over the time period of the measurement, the experimental result has strong dependence on the measurement time τ_m of the experimental method. For example, the mean time between two magnetic switches for a particle at finite temperature T, i.e., the Néel relaxation time τ_N is obtained as $\tau_N = \tau_0 \exp(E_B/k_BT)$.[65] Here, τ_0

is called the attempt time with a typical value $\approx 10^{-9}$s. So, if $\tau_m \gg \tau_N$, the measurement is too "slow" to reflect the magnetization dynamics because the measured magnetization will average to about zero. At this point, the ferromagnetic particle is said to be in a superparamagnetic state.[28] The τ_m for our transport measurement is on the order of 1s, which is much longer than the average time for electron tunneling ($\approx 1\mu$s) and the attempt time. On the other hand, it is shown that magnetization dynamics and electronic environment are coupled during the electron tunneling process.[19, 98] Numerical simulations can be used to help people better study the magnetization dynamics under the influence of tunneling electrons. Thus, models for magnetization dynamics need to be developed and understood.

1.3.1 Landau−Lifshitz−Gilbert Equation

Under the macro-spin assumption, the magnetization of a particle will rotate in response to the applied magnetic field and external noise. Landau-Lifshitz-Gilbert (LLG) equation is a phenomenological description of that rotation. It can be written in different forms in different circumstances. Because $\vec{S}$ is often used in prior works rather than $\vec{M}$, we write the LLG equation as:

$$\frac{\partial \vec{m}}{\partial t} = -\vec{m} \times [\vec{h}_{eff} + \alpha \vec{m} \times \frac{\partial \vec{m}}{\partial t}] \tag{1.14}$$

Here, $\vec{m} = \vec{S}/S_0$ is the unit vector for spin. $\vec{h}_{eff} = \nabla_{\vec{m}} \mathcal{H}(\vec{B}, \vec{S}, n)/S_0$ is the effective magnetic field, which includes applied field, demagnetizing field, and the effective field due to thermal fluctuations and SO interactions. α is the Gilbert damping parameter indicating the relaxation rate of the spin vector towards its equilibrium state. The mechanism for damping is not very clear at this moment. Possible origins include, but are not limited to, coupling to nuclear spin, electromagnetic environment, phonon bath, and scattering off of the paramagnetic impurities/interface.[97, 37, 38] The LLG equation has been successfully applied in the research of spin transfer torque,[94, 89, 64, 48] where the current needs to overcome a certain threshold so that the

current-induced torque can beat the damping and enable the magnetic switch. That threshold can be obtained using the LLG equation if a proper model of damping is assumed.[84, 101, 74] To accommodate different applications, multiple extensions of the LLG equation have been proposed.[86, 77, 79, 112] Those extensions are made to include the effect from different factors such as conduction electrons and thermal bath of elastic modes.

1.3.2 Master Equation

The number of spins in a particle with 2-5nm in diameter is on the order of 10^2 to 10^3. In this range, the dynamics of the spin vector in response to electron transport and magnetic field can also be described using quantum mechanics. The indicator of the magnetization dynamics thus becomes the changing probability distribution of different magnetic states, i.e., eigenstates of the magnetic Hamiltonian. That probability distribution can be predicted by the master equation,[102]

$$\frac{\partial P_\alpha}{\partial t} = \sum_{\alpha'} \sum_{l=L,R} \sum_{j} \sum_{\sigma=\uparrow,\downarrow} \Gamma_{jl\sigma} \Big\{ |<\alpha'|c_{j\sigma}|\alpha>|^2 \left[-(1-f_l(E_\alpha - E_{\alpha'}))P_\alpha + f_l(E_\alpha - E_{\alpha'})P_{\alpha'}\right] + |<\alpha'|c^\dagger_{j\sigma}|\alpha>|^2 \left[-f_l(E_{\alpha'} - E_\alpha)P_\alpha + (1-f_l(E_{\alpha'} - E_\alpha))P_{\alpha'}\right] \Big\}. \tag{1.15}$$

P_α is the probability of the particle staying at state $|\alpha>$. In sequential tunneling process, the number of electrons only changes between n and $n+1$, so α and α' extends over all the magnetic states with n and $n+1$ electrons. f_l is the Fermi-distribution function for left ($l = L$) and right ($l = R$) leads. $\Gamma_{jl\sigma}$ sets the tunneling rate for electrons with spin $\sigma =\uparrow,\downarrow$ at lead $l = L, R$. $c_{j\sigma}$ ($c^\dagger_{j\sigma}$) is the annihilation (creation) operator for an electron with spin σ at j-th energy level. $|<\alpha'|c^\dagger_{j\sigma}|\alpha>|^2$ are the tunneling matrix elements that govern the transition between different magnetic states. There is one important assumption about the time scale in the master equation: the time of transition $|<\alpha'|c^\dagger_{j\sigma}|\alpha>|$ ($|<\alpha'|c_{j\sigma}|\alpha>|$) is much shorter than the electron tunneling time(Γ^{-1}), meaning the magnetic system is in equilibrium before the next

electron tunneling event. The matrix elements$| < \alpha' | c^{\dagger}_{j\sigma} | \alpha > |^2$ reflect the magnetic structure of the particle including the effects of magnetic field, anisotropy and electron tunneling. They can be easily calculated based on the Clebsch-Gordan coefficients, if we decompose the magnetic states into eigenstates of $\hat{S}_z$. From the numerical simulation using the master equation, it is shown that the spins inside the particle can be fully randomized by the tunneling electrons.[102] If the magnetic Hamiltonian includes terms for mesoscopic fluctuations, the matrix elements could be very different from Clebsch-Gordan coefficients. I will present a more detailed discussion about the master equation in Chapter V.

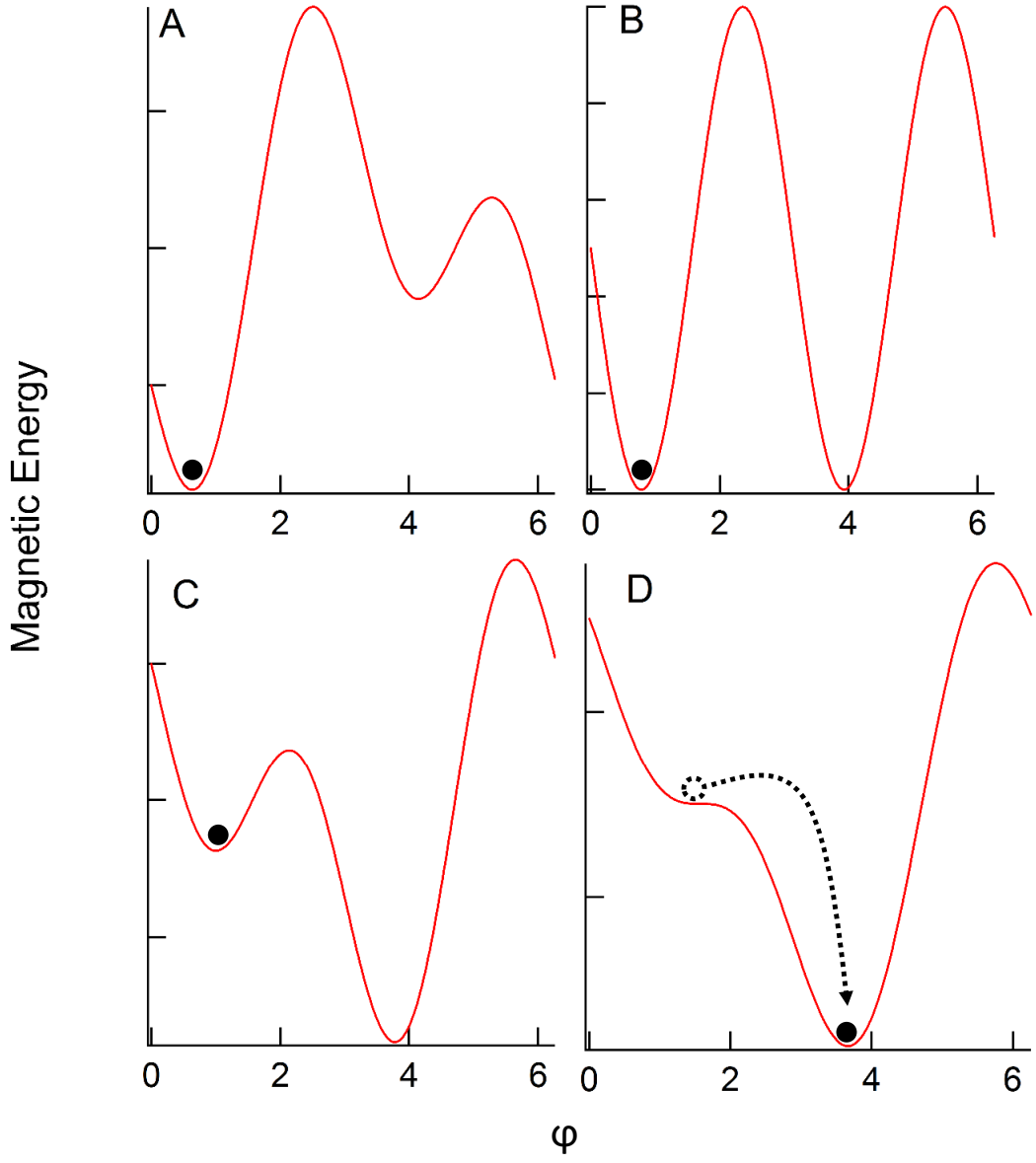

Figure 1.5: Magnetic energy versus ϕ at $B = 1/8\mu_0 M_s(N_h - Ne)$, 0, $B = -1/8\mu_0 M_s(N_h - Ne)$, and $B = -1/4\mu_0 M_s(N_h - Ne)$ for A to D, respectively. $\theta = 1/4\pi$. The black ball represents the direction of the magnetization.

CHAPTER 2

EXPERIMENTAL TECHNIQUES

2.1 Electron Beam Lithography

Electron Beam Lithography (EBL) is a method that uses a focused beam of electrons to generate patterns on a surface covered with an electron-sensitive film. This film is often referred to as a resist. In my lab, EBL is done using a Scanning Electron Microscope (SEM) (JEOL JSM5910), which can also be used to image a sample. In that SEM, electrons are thermally emitted from a tungsten filament which is heated up by a current. After being an accelerated by a very high acceleration voltage (30kV in our case), those electrons are then focused by several apertures and electric/magnetic-lenses on their way to the surface of sample. EBL does not require a mask, which brings a lot of flexibility in the pattern designing. Due to the short wavelength of a accelerated electron ($\approx$ 10pm), EBL can achieve very high resolution, but the final resolution also depends on the interaction between electrons and the resist. Since the operation principle and description of a typical SEM has been covered in Refs. [93, 58], I will skip those parts and focus on the EBL. Figure 2.1 displays a typical flow of EBL including metal deposition and lift-off process.

2.1.1 Preparation of the wafer/chip

Before putting a wafer/chip into the SEM and exposing it with electrons, one needs to form a layer of resist on the surface of the wafer/chip. The formation of a correct resist with proper thickness and bake time is important for writing small features close to the limits of a given SEM. A bilayer configuration is commonly used for the lift-off process where methyl methacrylate (MMA) is the first layer and poly(methyl methacrylate) (PMMA) is the second layer (Figure 2.1A). The advantage of this

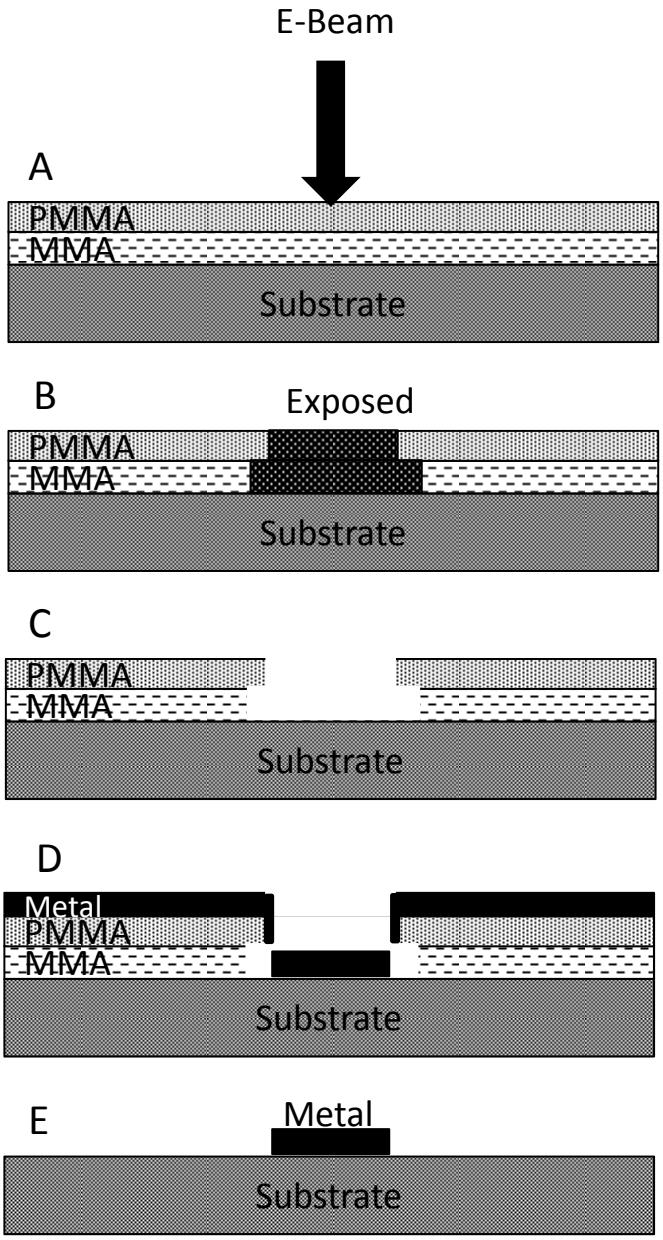

Figure 2.1: A and B: PMMA and MMA bilayer resist is exposed to the electron beam. C: The exposed area is removed during the development. D: A metal film is deposited on the sample. E: Excess metal is removed during the lift-off process leading to the final structure.

configuration is that, because MMA is more sensitive to electrons than PMMA, a inverse "T" shaped void will be formed after the electron exposure and development step (Figure 2.1C), which can improve the yield of lift-off process. Usually spin coating is used to make the resist layer on the surface of the wafer/chip. Before the coating process, the wafer/chip should be quickly cleaned by flushing it with acetone for 10s, then rinsing with IPA for 10s, and letting it dry while spinning the wafer/chip at 2000 RPM. During the spinning, the wafer/chip is held on the chuck of the spinner by vacuum pulling. This cleaning step can remove the dust on the wafer/chip. Otherwise, dust can cause serious defects on the resist layer. In the spin coating process, a solution of the resist is first deposited on the wafer/chip. Then, the spinner is quickly accelerated to the desired spin speed, and the solution will flow towards the edge of wafer/chip due to the centrifugal force. As the coating process goes on, the solution of the resist gradually dries leading to a increasing viscosity. Therefore, a balance will be reached where the centrifugal force can no longer move the solution due to the increasing viscosity. From that point, a longer spin time will not effectively reduce the thickness of the resist. Since the centrifugal force is determined by the spin speed, spin speed is one of the most important factors in the coating process that affects the final thickness of a resist layer. A higher spin speed generally leads to a thinner layer of resist.[33] Because the solution of resist dries very rapidly, the acceleration of the spinner towards the final spin speed needs to be tuned accurately. After spin coating, the coated wafer/chip should be baked on a hotplate for several minutes. The baking process can further dry the solvent and cure the resist as well as improve the uniformity of the resist layer. The baking temperature and time should be adjusted according to the thickness and thermal properties of the wafer/chip as well as the material of the resist so that the required baking temperature and cure time are satisfied. After the baking process, the wafer/chip is ready for EBL. When not in use, the coated wafer/chip should be kept in a dry and dark case.

2.1.2 Pattern Design and Writing

One primary advantage of EBL over photolithography is that it can directly write patterns according to a custom design without making a mask. When designing the pattern, there are two things that need special attention.

- **The resolution of the EBL**. The resolution of the EBL strongly depends on the interactions between the electron beam in the SEM and the resist layer, which limits the size of the smallest feature one can generate based on the SEM and the resist layer being used. Therefore, a basic understanding of the SEM and resist specification is needed before designing the pattern, especially when the pattern includes very fine features.

- **The writing field**. The writing field is a square whose size is determined by the magnification of the SEM during pattern writing. A higher magnification usually leads to better resolution but smaller writing field. Generally, one should write small features of the pattern at high magnification and large features at small magnification. The center of the writing field will typically shift as the magnification window is changing between the fine and coarse windows. The shift can cause disconnection between the small and large features. Fortunately, the shift between two certain magnifications stays constant over time and can be easily measured. In the Nanometer Pattern Generation System (NPGS), this shift can be compensated by the "Origin Offset" prompt in the "Run File" editor with appropriate parameters. Also, it is recommended that the smallest features be placed at the center part of the writing field because the electron beam tends to be off focus and distorted as it moves to the edge of the writing field.

Before writing the real pattern, it is important to optimize the following two aspects of the electron beam .

- **Focus**. The focus of the beam is generally independent of the SEM magnification. Because the chip is usually not level, it is very important to adjust the focus near the final writing area especially when very fine features are required. If a very large writing area is needed, NPGS provides "X-Y-Focus Mode". This mode can automatically adjust the focus according to the position of a pattern based on a "focus map" covering the whole writing area. Please refer to the NPGS manual for instructions about this mode.

- **Astigmatism**. The astigmatism of the electron beam is another factor that can strongly affect the quality of the SEM image as well as the EBL. Different from focus, astigmatism is an internal parameter of the electron beam, meaning it is independent of the relative position between the electron beam and the chip. With astigmatism, the SEM image will appear to be stretched in a certain direction and lines written at different angles will be exposed at different levels.

The focus and astigmatism can all be tuned according to the quality of the SEM image with the assumption that a better set of parameters will lead to a higher image quality. "The goal is to precisely check that equal displacement in either direction of the parameter being adjusted will degrade the image quality by an equal amount."[40] When human eyes reach their limit in verifying the statement above, contamination spot diagnostic technique can be used. This method is done by switching the SEM control to the NPGS at the highest magnification for about 10s. When the beam is well optimized, a circular spot with about 30-50nm in diameter will be produced. A larger and/or blurry spot usually indicates off focus while a noncircular spot often means large astigmatism. It is highly recommended that the contamination spot diagnostic is done near the writing area to ensure the optimization of the electron beam before writing a pattern.

Dose is another parameter that needs to be tuned before writing. It measures the exposure of the resist to the electron beam. The exposed areas consist of arrays of

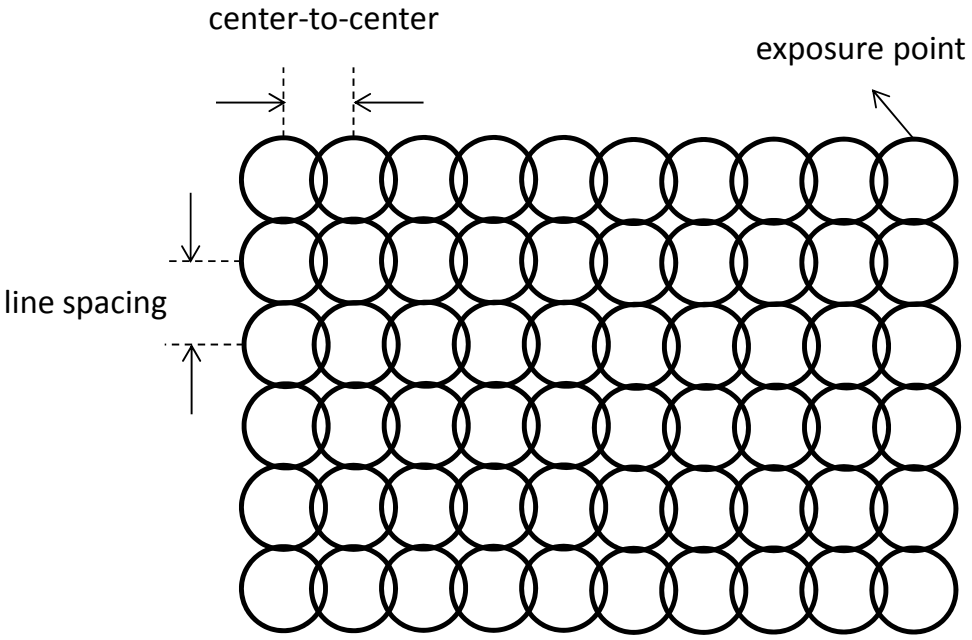

Figure 2.2: Illustration of E-Beam exposure.

exposure points, as shown in Figure 2.2. With the help of a beam blanker, each point is exposed to the electron beam for a certain amount of time, which is called the "dwell time". The "Center-to-Center" prompt in the "Run File" editor represents the distance between the neighboring spots in a line while the "Line Spacing" is the distance between neighboring lines. From Figure 2.2, the area dose can be expressed as

$$\text{Area dose} = \frac{\text{beam current} \times \text{dwell time}}{\text{Center-to-Center} \times \text{Line Spacing}}$$

The size of each spot usually increases with the electron beam current. So a small beam current (10pA) is recommended for very fine features, while a large current can be used for large features to reduce the pattern writing time. The dwell time can be automatically calculated by NPGS from the dose, beam current, center-to-center, and line spacing. Since the electron beam is switched on/off by a beam blanker, the dwell time should be much larger than the rise time of the beam blanker to

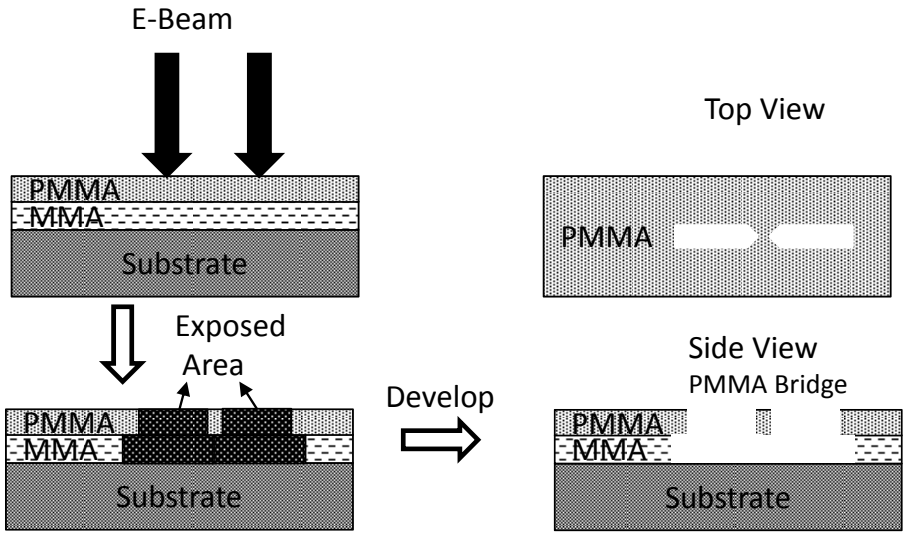

Figure 2.3: The formation of a PMMA bridge for shadow evaporation

ensure the accuracy of the dose. In addition to the primary dose, the actual dose also includes the contribution from secondary electrons created by the primary beam. The secondary dose at one place could originated from another place, which is known as the proximity effect. High beam energy and thin resist can be used to reduce the proximity effect in generating very small structures. Since each pattern will receive secondary dose from neighboring patterns, the determination of actual dose become very complex. Thus, a dose test should always be performed for a new pattern design to ensure an appropriate dose.

The proximity effect can be utilized in the shadow evaporation technique. Because MMA is more sensitive to electrons than PMMA, the secondary electrons can expose larger area in MMA than PMMA. As shown in Figure 2.3, if the two patterns are close enough, the exposed MMA might be able to connect underneath the PMMA. After the exposed MMA and PMMA are removed during the development step, the removed MMA leaves a tunnel under the PMMA and the PMMA left between the two patterns becomes a bridge. That PMMA bridge can be used as a mask during

the shadow evaporation process, which will be described in Section. 2.2.

2.1.3 Automatic Alignment

Sometimes, a single step of EBL is not enough to fabricate a complex device. For example, a gated particle device needs three steps of EBL, where the first step is for alignment markers, the second step is for the gate, and the last step is for the tunneling device. Each of these steps includes spin coating and metal deposition. If multi-step EBL is involved in a sample fabrication, alignment is necessary to match the structure produced at subsequent steps. For certain types of devices like devices on exfoliated graphene, manual alignment is preferred because each pattern design can only be used once due to the uncontrollable shape and position of graphene flakes. One the other hand, for tunneling devices, an array of identical patterns is usually produced on the chip during EBL. Thus, it is more efficient to let the pattern generating system perform a fully automatic alignment (Auto-Alignment) for each pattern. The NPGS manual has very detailed instructions about how to use the fully Auto-Alignment function. Here, I will elaborate some key steps and tips in setting up this function based on my own experience.

- **The accuracy of the alignment.** The alignment has its own accuracy which is set by the spacing between alignment pixels ("Center-to-Center" in a NPGS "Run File"). Since small spacing means more electron beam sweeps, more accurate and complex alignment would lead to higher time consumption. Therefore, one should make the alignment accurate enough for the experiment while trying to keep the time cost low. Generally, the spacing between alignment pixels should be half of the desired accuracy. The accuracy of the alignment also depends on the magnification. Typically, the accuracy of a alignment can reach about 1/10000 to 1/30000 of the writing field size determined by the magnification of the SEM. At a very low magnification, i.e., a very large writing field,

the scan coil of the SEM may not be linear, thus misalignment could happen.

- **The alignment markers.** The alignment markers can be produced using EBL or photo-lithography. "+" or "L" shaped markers are recommended. Gold is a good material for alignment markers because it can provide high contrast under SEM imaging, which is preferred in Auto-Alignment . Alternatively, the void on the resist after the removal of the exposed resist in the development step can also be used as markers when high alignment accuracy is not required. It does not have as good of sharpness or contrast as gold markers, but it saves a lot of time since no metal deposition or lift-off are needed. With two markers being independently aligned, the alignment can correct both the offset and orientation of the pattern relative to the chip.

- **The overlay.** The overlay is a designed pattern used to fit the real markers on the sample. In Auto-Alignment, the overlay should be drawn as lines with zero width that match the edges of the alignment markers. Since errors can happen during the production of markers, the overlay should be drawn based on the final appearance of the markers instead of their original design. During the alignment process, alignment windows need to be assigned, which define the region that will be scanned by the electron beam. Each window should only contain one overlay inside. Those windows should be placed within the same writing field for the device but kept away from the intended device area. Because the Auto-Alignment is required for each device, the size of the window must be large enough to compensate the random error in the movement of the stage from one device to the next device .

- **Prealignment of the angle.** Since a chip with a array of devices is usually very large (1cm×1cm) and can have an arbitrary orientation relative to the stage, it is essential to align the array coordinate axes to the axes of stage

motion. Otherwise, a misalignment will eventually happen as the stage moves further away from the starting position. Though the global rotation correction function of NPGS can address this problem by decomposing the each stage movement into X and Y components according to the rotation matrix between stage and array, it is not recommended for Auto-Alignment because large errors will accumulate during complex stage movements. It is better to rotate the stage based on a series of markers to make sure that the row/column of the array is aligned well with the x/y axes of the stage motion . Generally, the shift caused by moving from the first device to the last device of one column/row should be less than half size of the alignment window.

A set of appropriate parameters is also critical for the success and efficiency of Auto-Alignment. There are three basic Auto-Align modes provided by NPGS, which are based on the NPGS system files started with "Pg_AA". The initial parameters in those files are just typical settings and need to be modified according to the experiment. A short summary of some important parameters is presented here. More detailed descriptions about all the parameters are included in the NPGS manual. [40]

- **Initial Step Size (1-9):** The step size determines how many of the calculated points in the alignment windows are to be scanned. For example, '1' means every point will be scanned while '3' means every third point will be scanned. A larger number leads to a shorter window scan time but a coarser image thus a lower accuracy, and vise versa.

- **Auto Contrast:** It determines the upper and lower boundaries for the data displayed in the windows to enhance the contrast. Let MAX (MIN) be the input value for this option and the data-max (data-min) be the greatest (smallest) data taken from the scan. Then the upper (lower) boundaries of the displayed data will be "data-max(1-MAX)" ("data-min(1+MIN)"). All the data will be

cut off at the boundaries. This setting is very useful when the markers do not have very good contrast or the background noise is large.

- **# of Times to Scan Windows:** This number determines the number of times the scan will be repeated on the alignment windows before the computer starts aligning the overlay to the image. The final image showed in a window is an average over all scans. More number of scans generally lead to better image but will consume more time. I found '2' or '3' is good enough if gold markers are used.

- **# of Times to Align Each Set of Windows:** This is the number of times that a set of alignment windows will be Auto-Aligned. To compensate for the sample rotation, the alignment should be done at least twice for best results.

- **Threshold Color (1-100):** In this parameter, 1 (100) denotes the darkest (brightest) color. Only the pixels brighter than this number would be used for Auto-Alignment process. An increase of this number can eliminate unnecessary background information, thus improving the speed and accuracy of the alignment. However, if this number is higher than the brightness of markers, serious errors will occur. For gold markers on SiO_2 substrate, 30-50 is a good range for this number.

- **Initial Pre-Align Keystroke Commands:** The entered characters corresponds to the commands of image process to the windows before Auto-Aligning. A list of those characters is included in the NPGS manual. 'f' and 'e' are recommended which stand for 'spatial average' and 'enhance the edge', respectively.

- **Stage: Mode:** This option should be turned on; thus stage motion can be enabled for a coarse correction. When writing an array of devices, a lot of stage movements will be involved, leading to an accumulation of random errors.

When a marker is too close to the edge of the window or partially outside, a stage movement is a better way to correct such a large offset. First, it is a self-correction mechanism for the error accumulated from all previous movements, thus it can prevent failure of Auto-Alignment which happens when a marker is entirely out of the window. Also, because the correction done by the electron beam is reduced, the beam would have less distortion, which is desired in pattern writing.

2.2 Thermal Evaporation and Lift-off

After the EBL, the chip will be developed in a developer solution to remove the exposed resist. A microscope inspection should be done to ensure the desired pattern is produced on the chip. Now it is ready to deposit metal onto the chip in the vacuum chamber of the evaporator. A sketch of the evaporator components in the vacuum chamber is shown in Figure 2.4. The chip is attached to the sample holder which can be rotated by a spring extended to the outside of the chamber. The metal sources are placed in molybdenum (Mo) boats. Boats with an aluminum oxide coat (temperature limit 1200^oC) works for all metals, while a boat with no coat can also be used for evaporating Au. After the chip and metal source are loaded in the chamber, the vacuum chamber should be closed and pumped down to the base pressure ($\approx 2 \times 10^{-7}$torr). Then, the boats can be heated up by sourcing a electrical current through the corresponding electrodes. The heating power on the boat should increase slowly or the melted metal might flow out of the boat. The evaporation will start after the metal is melted. A shutter is used to block the metal vapor from the chip. One can control the metal deposition using the shutter. The deposition rate and the thickness of the resulting metal film are monitored by a crystal monitor. As mentioned in the previous section, a PMMA bridge can be produced in EBL, which enables the shadow evaporation technique. In this technique, the relative

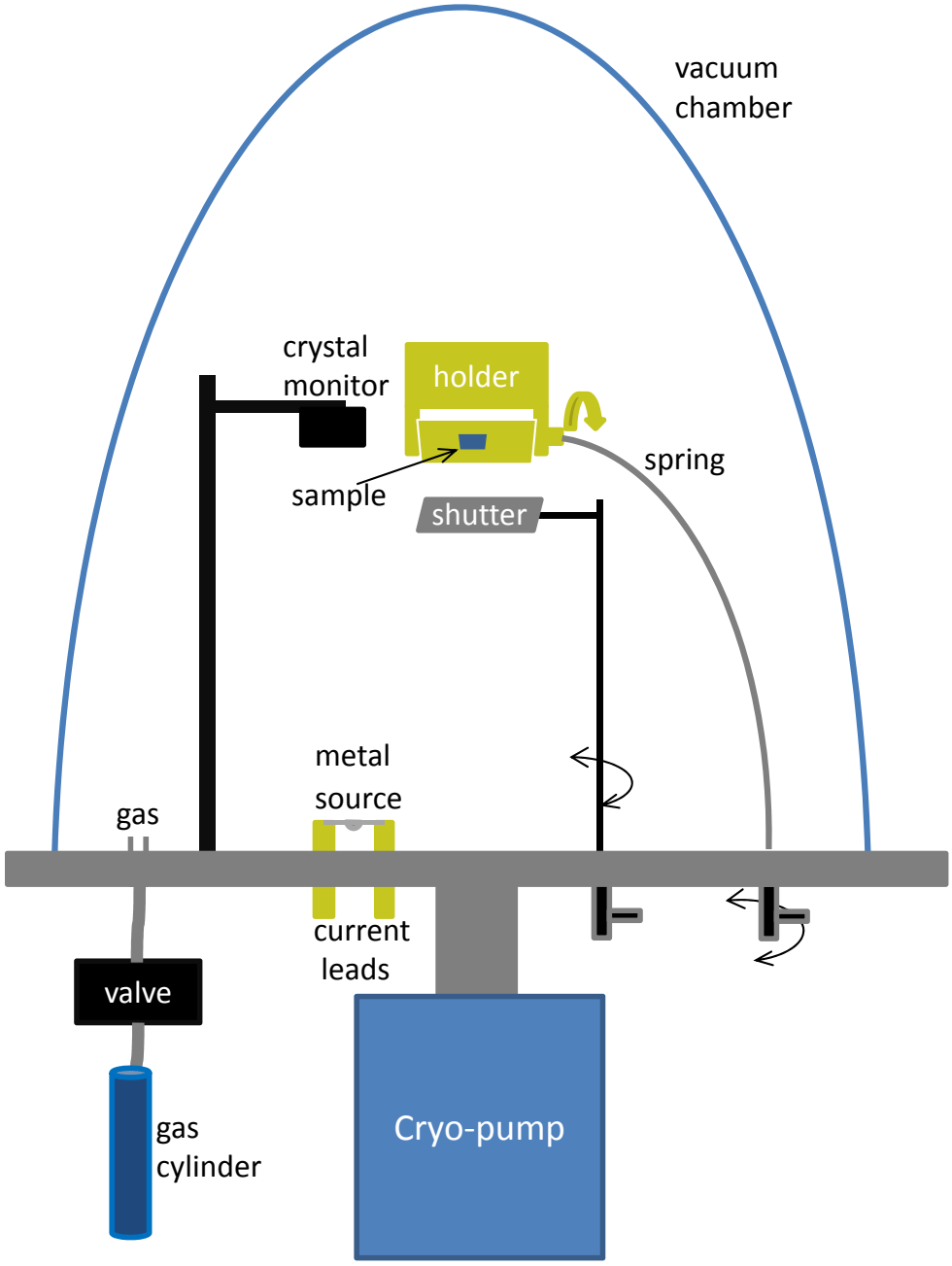

Figure 2.4: A sketch of the vacuum chamber.

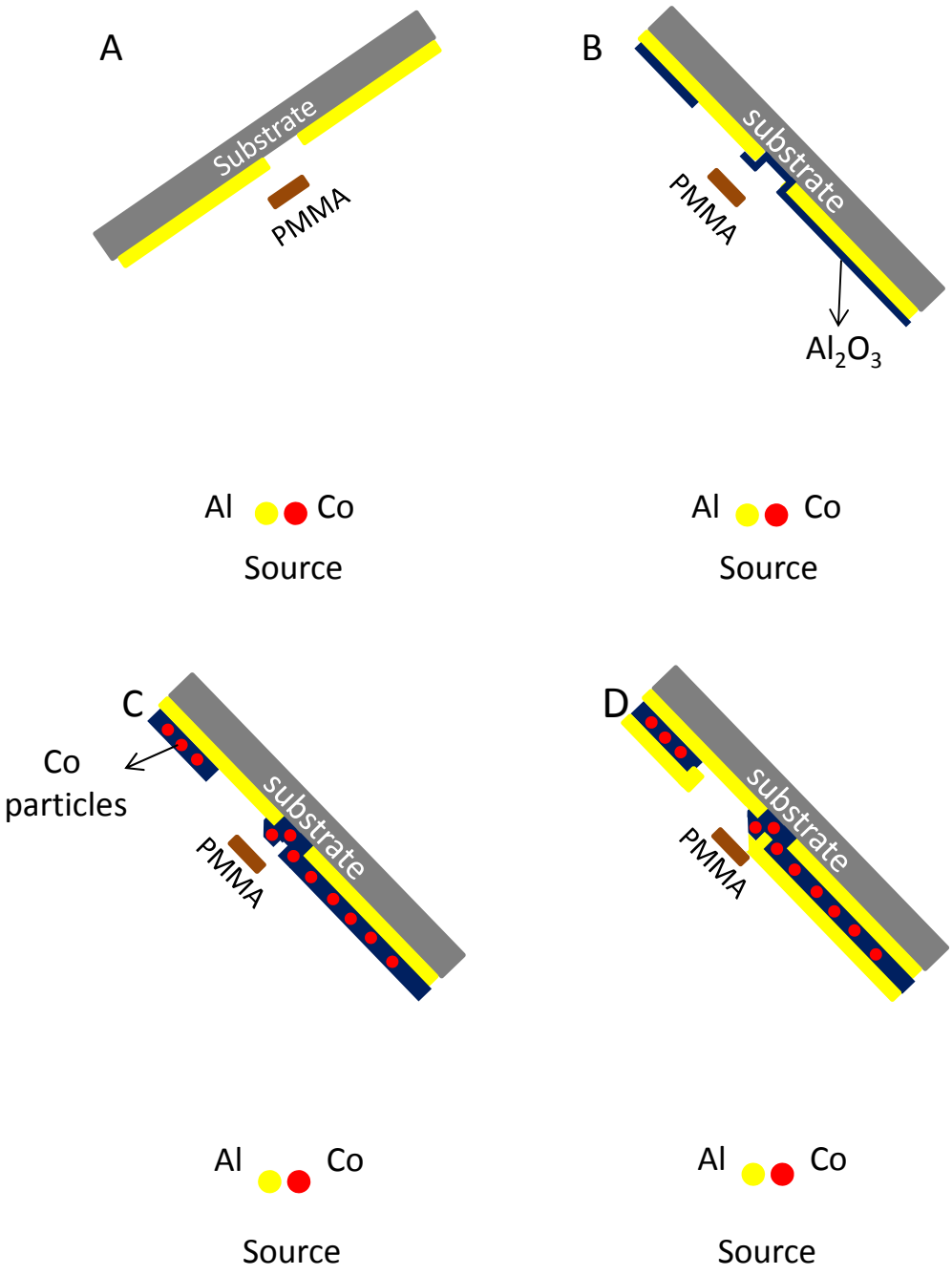

Figure 2.5: Shadow evaporation. A: Al film is deposited at one angle. B: The chip is switched to another angle. A thin Al_2O_3 layer is deposited. C: A layer of Co particles are deposited and then covered with Al_2O_3. D: Al film is deposited to form the other lead.

angle between the incident metal vapor and the chip is controlled by the rotary stage using a spring (Figure 2.4). The PMMA bridge can produce different shadows at different vapor incident angles relative to the stage. A small overlap between the metal film deposited at different angles can be achieved if the angles are precisely controlled. As an example, Figure 2.5 sketches the process of fabricating a tunneling device with Co particles and Al leads using shadow evaporation.

The chip is taken out of the chamber after it cools down. A lift-off process is then performed to remove the resist and the excess metal. During the lift-off, the chip is submerged in acetone at room temperature for $15 - 20$ minutes. One can spray acetone onto the chip to wash the metal away from the chip. Once the lift-off is done, the chip should be taken out of acetone, rinsed with IPA before the acetone dries, and blown dry with dry air. After lift-off, the devices are ready for testing.

2.3 Transport Measurement

The devices are characterized using electron transport measurement. The detailed study is usually done at 4.2K and below. The devices are prescreened at room temperature before being wired to chip holders and cooled down. The prescreening is performed using a micro-manipulator. Tunneling devices with resistance between 10MΩ to 1GΩ are usually good candidates for further test at low temperatures. During the transport measurement, an SRS Synthesized Function Generator (DS345) is used to supply bias voltage. The current is measured by an Ithaco (Model 1211) current amplifier. The circuit diagram is shown in Figure 2.6. The output of the function generator is connected to the source and drain leads of the device via an aluminum "Ithaco Box" using BNC cables. The Ithaco current amplifier is also connected to the box using a triaxial cable while the out-shield and the inner-shield of the triaxial cable are shorted at the "input" connector of the current amplifier. The metal shell of the "Ithaco Box", the outer-shield of the triaxial cable, and the outer-shield of the

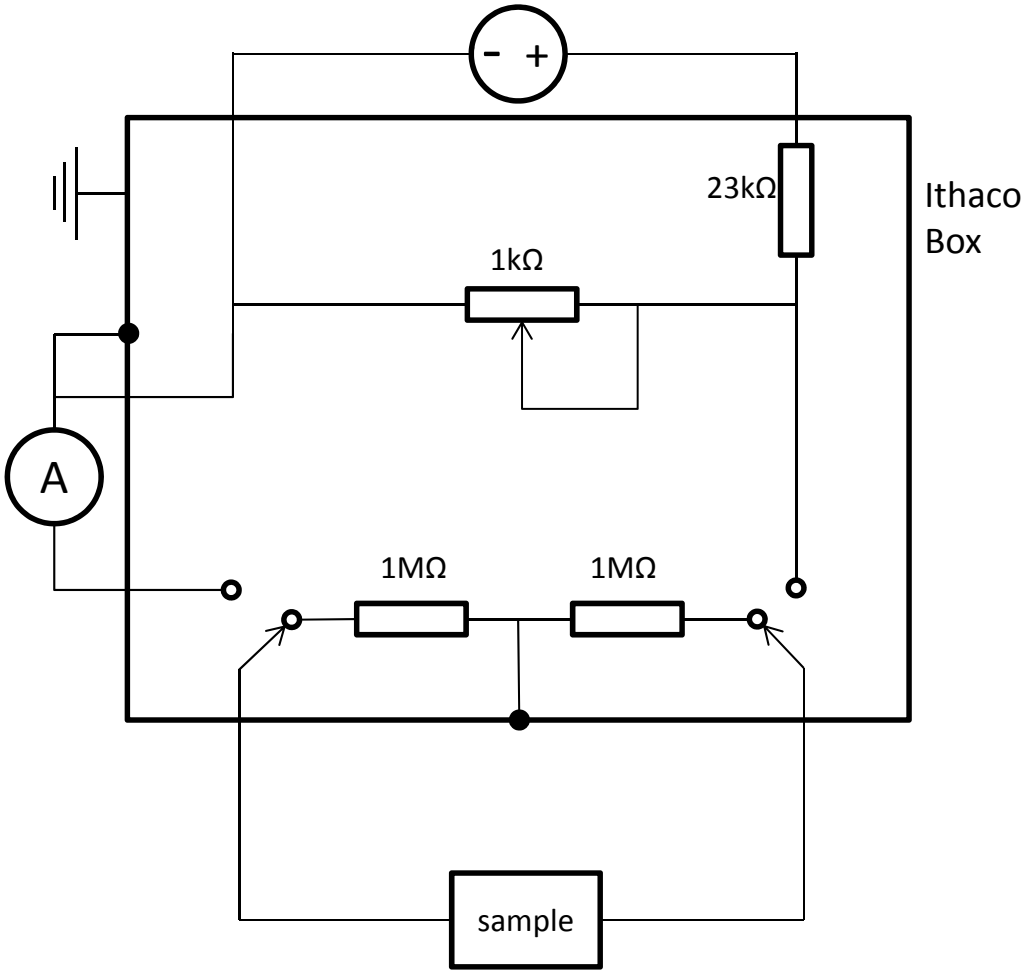

Figure 2.6: A circuit diagram for transport measurement.

two BNC cables that go to the device are all grounded, which creates a small Faraday cage to minimize the external interference. This setup is essential for high sensitive transport measurement.

2.3.1 Dipstick

A dipstick is used for measurements at 4.2K. The devices are attached to the end of the dipstick and the dipstick is then inserted into the liquid helium (He) dewar. A diagram of our dipstick is shown in Figure 2.7. The outer-shield of the dipstick is removable, which is designed mainly to protect the inner part of the dipstick during cool-down and warm-up. If the dipstick freezes in the dewar, the inner part of the dipstick and the magnet can be moved out of the outer-shield. Then, one can insert a hose into the outer-shield to the frozen part (usually around the neck of the He dewar) and blow warm He gas to defrost. The inner-shield is a frame of the dipstick with the superconducting magnet attached to its end. On the cap welded at the top of the inner-shield, there are two connectors for the connection between the magnet power cable and the power supply. A Fisher connector is attached on the top of the slidable shield. Inside the slidable shield, phosphor bronze wires are connected to the Fisher connector and then go to the MicroTech connector at the other end of the shield. When loading devices, one can push the slidable shield in so that the MicroTech connector moves outside of the bottom end of the magnet. The sample holders with devices wired to them are attached to the MicroTech connector. Then, the devices are slid into the center of the magnet and are ready for cool-down. The outer-shield, inner-shield, and the slidable shield of the dipstick are all made of AISI type 314 stainless steel, because of its low thermal conductance, weak magnetism, and good mechanical properties at low temperatures. Since the dipstick is designed to be directly inserted into a He dewar, the diameter of the outer-shield should not exceed 1-3/8in. which is a little smaller than the size of the neck of most He dewars.

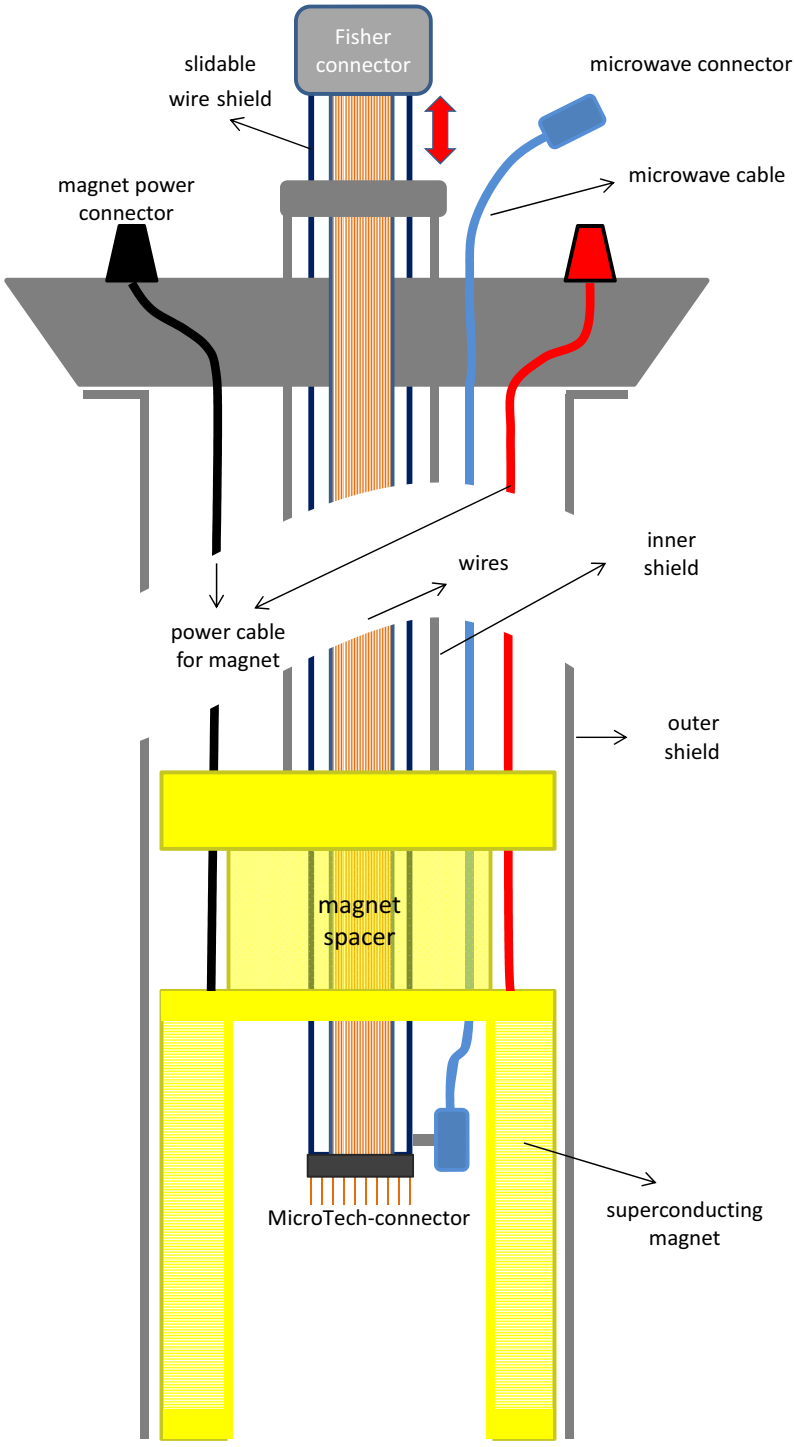

Figure 2.7: A diagram of the dipstick.

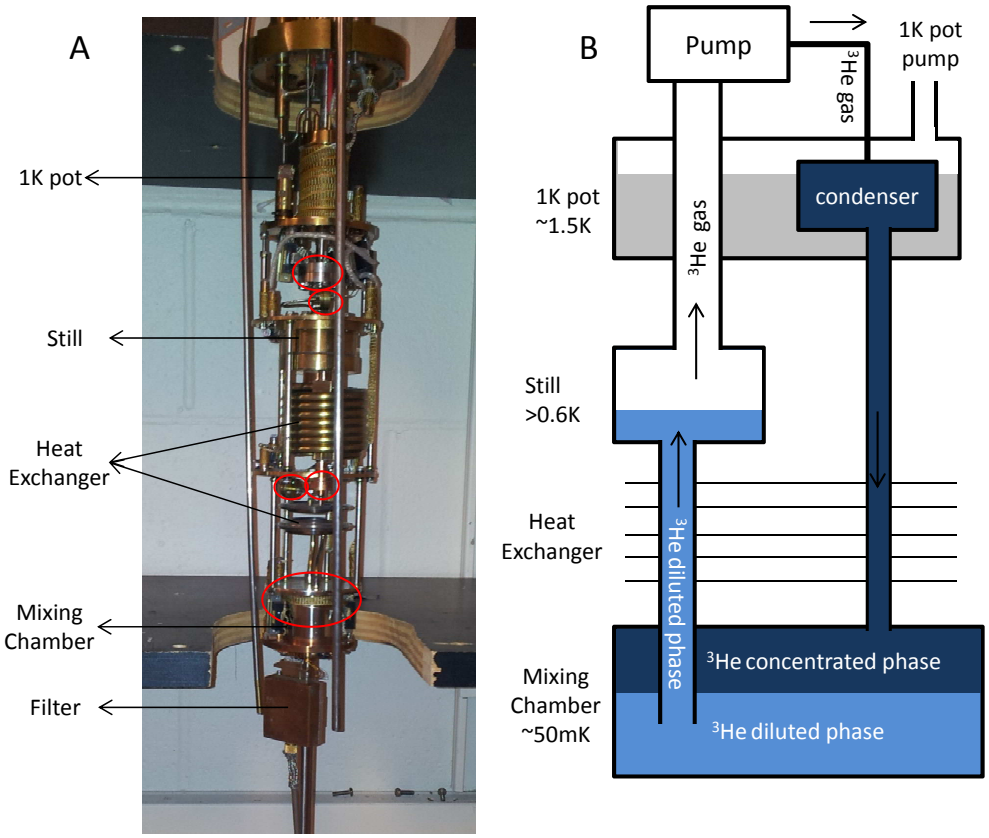

Figure 2.8: A: A photo of the dilution refrigerator in our lab. The red circles point out the five joints of the fridge. B: A schematics showing the operation principle of the dilution refrigerator.

2.3.2 Dilution Refrigerator

Liquid He temperature 4.2K corresponds to a energy of 360μeV, and 10mK to 0.86μeV. A lower temperature can give us higher resolution in energy, enabling detailed studies of the quantum effects in nanoparticles. A ^{3}He/^{4}He dilution refrigerator is an apparatus that can achieve a base temperature of around 10mK. A photo of the dilution refrigerator in our lab and a schematic of a dilution refrigerator is shown in Figure 2.8.

Below 0.87K, the ^{3}He/^{4}He mixture separates into two phases: ^{3}He diluted phase sitting at the bottom of the mixing chamber, and a ^{3}He concentrated phase floating on top. The ^{3}He concentration in the diluted phase is finite (6.6%) at saturated vapor

pressure. ^{4}He becomes superfluid at such low temperature, meaning its vapor pressure becomes zero. On the other hand, ^{3}He atoms are Fermions, so they still maintain a finite vapor pressure. ^{3}He will be removed by pumping on the diluted phase of the mixture, thus the ^{3}He in the concentrated phase will migrate across the phase boundary to maintain the concentration. This "evaporation" of ^{3}He from the concentrated phase to the diluted phase costs energy by removing heat from the mixing chamber. More details about the operation principle of the dilution refrigerator is available at Ref. [56].

The manual from "Oxford Instruments" includes detailed description of procedures for running a dilution refrigerator.[71] Here I will summarize the key parts from running the 1K pot to circulate the mixture.

- **1K pot** Before cooling the insert to 4K, the 1K pot needs to be pumped out or the frozen air inside the pot will cause device failure. The 1K pot uses a needle valve to slowly draw liquid helium into the pot. At the same time, a rotary pump is pumping on the pot. The evaporation of liquid helium provides the cooling power that lowers the temperature of the pot and condense the mixture. To quickly cool the 1K pot, one can increase the opening of the needle valve until the pressure rises to hundreds of mBar. Then, decrease the needle valve opening so the pressure drops fast. The temperature of the 1K pot should decrease very quickly at this time. The needle valve should be adjusted so that the 1K pot has a pressure of about 10mBar and a temperature within 1.2-1.5K. A higher pressure usually leads to higher cooling power but higher temperature.

- **Mixture Condensation** After the 1K pot is stabilized between 1.2-1.5K, one can start condensing the ^{3}He/^{4}He mixture. One can open the valve between condenser line and still and start let mixture enter the dilution unit. The mixture will condense both at the condenser and the still when it goes through 1K pot. Because the cooling power of the 1K pot is limited, this step needs to

be done very slowly and carefully. The pressure in the condenser line should be kept below 200mBar so that the 1K pot is not overloaded. When the pressure of the mixture in the storage drum is lower than 200mBar, one can fully open the valve between the storage drum and the condenser line and start circulating the mixture.

- **Mixture Circulation** At this point, the valve connecting the condenser line and still should be closed. One can slowly open the valve between the still and the ^{3}He pump to start circulating. The pressure in the condenser line should be monitored closely to make sure the system is not out of equilibrium. After the valve between the still and the ^{3}He pump is fully open, the mixing chamber should be gradually cooled to the base temperature. By tuning the heater on the still, one can increase rate of ^{3}He flow, thus increasing the cooling power.

At low temperatures ($<$ 1K), the thermal coupling between electron and the lattice of a metal becomes weak, meaning the electrons can no longer be cooled by the mixing chamber. At mK-temperatures, a small electric field can significantly heat the electrons above the temperature of the phonon bath.[80] Thus, a filter box is introduced to further cool the electrons, as shown in Figure 2.8. The filter box we use is a copper powder filter similar to those studied in Ref. [25]. The principle of the filter is to attenuate the high frequency spectrum of electrons through capacitive coupling to the copper powder. The filter is made by inserting thin wires through a box filled with a matrix of copper powder and epoxy. As the electrons in the wires pass through the filter box, the high frequency spectrum of those electrons has a better capacitive coupling to the copper powder than the low frequency part. The high frequency radiation induces current in those copper grains which heats up the copper powder. The heat is then dumped to the mixing chamber through the epoxy matrix. Therefore, the high frequency spectrum of electrons is attenuated when those electrons pass through the filter box, which effectively reduce the electron

temperature.

As shown in Figure 2.8A, the five joints in red circles are all have indium seals. After being thermal cycled many times, the indium seals of those joints will become loose, which can cause leakage of precious mixture. So it is important to check the leak of those joints and tighten them when needed. At some point, the indium seals of those joints do need to be replaced, and I am lucky enough to have done it during my PhD years. I want to share some of my experience about replacing those indium seals here.

Only the big joint just below the 1K pot is made of stainless steel, others are made of copper. When disassembling the dilution unit, one should start from the mixing chamber then gradually move up to the stainless steel joint . The joint that is next to the stainless steel has a needle inside, so be very careful when breaking the indium seal of that joint. There are tapped holes on the mixing chamber and stainless steel joint with no screws in them, one should use screws to "jack up" the joint through those holes because the indium seals are usually very tight. The remaining indium on those joints can be first cleaned using a wood stick and then scrubbed with a material that is "mild abrasive" (Green Scotch-Brite Heavy Duty Scrub is a good choice). After the old indium is removed, the interfaces of the joints should be cleaned with acetone and rinsed with IPA to make sure they are free of grease and dust. No vacuum grease is allowed for those joints or superfluid leakage can happen at low temperatures.

It is not a very technical work, but I still want to list some points that need special attention.

- Be patient. It is a big project due to the delicate design of the dilution unit, the complex electrical wiring, and the value of the dilution refrigerator. So please allow enough time for a high quality work.

- Keep a good record. It is often easier to disassemble than put things back together. So a record about where to put those screws, heat sinks, thermometers,

and heaters as well as how to winding those wires should be kept carefully and in detail when disassembling the dilution refrigerator.

- Keep your gloves clean. Make sure the gloves are free of grease and acid before touching the parts, especially those joints. A little bit of grease in those joint will cause a bad leak at low temperatures.

- Teamwork. Some part of this work needs two people and one more person can lower the chance of making mistakes. I am lucky to have had Patrick Gartland work with me on this one.

- Do a leak test. A thorough leak test is needed for every joint to make sure they are leak free. A leak test at 77K or even 4.2K is recommended because some leaks can only be seen at low temperatures.

2.3.3 Superconducting Magnet

A superconducting magnet is used to generate magnetic field during transport measurement. The magnet at the end of the dipstick is made in our lab. It is essentially a solenoid with superconducting wires wound on a copper tube. Here I will briefly describe the procedure of making a superconducting magnet.

- The first step is to make a frame for the magnet. A magnet frame is usually made of copper because it has a good thermal conductivity and is not superconducting at 4.2K. The frame for our magnet consists of a spool and a spacer, as shown in Figure 2.9. The spool can be made by gluing a copper tube and two copper rings together using epoxy (Stycast 1266) or solder. There are eight tapped holes on the edge of the rings so we can use screws to attach the magnet. Because superconducting wires are very expensive and winding them takes a lot of effort, it is better to keep the length of the solenoid short provided that it can generate the desired field. Thus, a spacer is introduced to meet the length

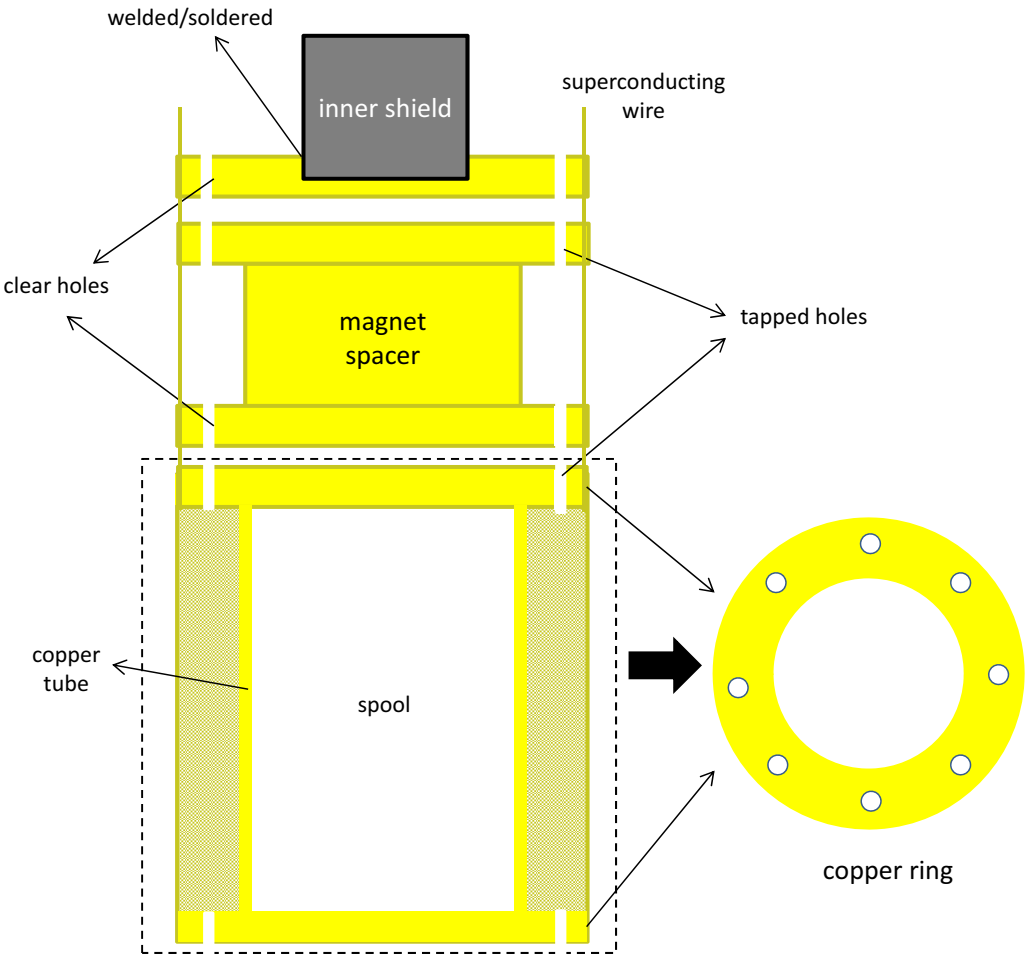

Figure 2.9: A illustration of the superconducting magnet

requirement of the magnet. The spacer is basically a spool, but the screw holes at the bottom ring are clear so it can be attached to the solenoid using screws. Another copper ring with clear holes is welded/soldered on the inner-shield of the dipstick. After finishing winding the magnet, one can screw the magnet onto the copper ring on the inner-shield.

- The second step is to wind the superconducting wire. We use NbTi wire coated with CuNi to improve thermal conductivity. Finer wire can result in more number of turns but has a smaller critical current and is more difficult to wind. The wire is wound on the frame using a winder. Enough wire needs to be left outside the solenoid for connections to the power cable before the start of winding. A small tension should be kept on the wire to improve the uniformity of wound turns. When winding the wires, one can use a wood stick to push the wire so the wound turns sit tightly against each other. A small amount of epoxy (Stycast 1266) can help bond the wire together. Defects are inevitable during the winding especially at the edge of the spool. Generally, the first layer of wire is most uniform and the defects will accumulate as more layers are stacked. The winding should begin and stop at the same end of the spool for the convenience of power connection. Also, one should leave enough wire for power connections after the stop of winding. The excess wire for connection can be loosely winded on the spacer and held by a tape. No kink is allowed at any part of the wire because it can break the superconductivity of the wire. One should be very careful when winding the magnet, because if the wire is kinked at some point, all the wound turns should be forfeited to have a fresh start.

- The third step is to strengthen the magnet. The insulation of the superconducting wire can fail after many thermal cyclings, so epoxy can be used to improve the life-time of a magnet. One should prepare about 20ml of epoxy (Stycast

1266). The air in the epoxy needs to be removed by putting the epoxy in a chamber and pumping on the chamber. When pumping on the chamber, a lot of bubbles will emerge and soon disappear like the epoxy is "boiling". The "boiling" of the epoxy gets weaker as the air being pumped out. After about 10 to 20s, we can stop pumping if the "boiling" continues but does not get weaker. At this point, most of the air has been removed from the epoxy. The solenoid should be brushed with epoxy using cotton swabs and then put in a vacuum chamber. When evacuating the vacuum chamber, the epoxy on the surface of the solenoid will be sucked into the gaps between wires. This brush-and-pump process needs to be performed several times until no more epoxy can be sucked into the solenoid. The excess epoxy on the surface should be wiped with soft paper towel. Then, the magnet should be baked in a rotisserie oven at 140^oF overnight to cure the epoxy. After the epoxy is cured, the magnet can be attached to the dipstick and soldered (Sn60/Pb40) to the power cables.

CHAPTER 3

ELECTRON TRANSPORT MEASUREMENT OF CO PARTICLES IN THE PRESENCE OF MICROWAVE

3.1 Introduction

In the past decade, magnetic particles have generated great interest because of their novel behavior and potential importance in further miniaturization of magnetic storage. Difficult experiments have been carried out to study the electronic and magnetic properties of individual magnetic particles [54, 106, 70, 31, 69, 19, 42, 91, 41, 110, 90]. Some of these experiments [31, 19] focus on electron tunneling measurements of discrete energy levels of the particles. Rich phenomena revealed by these experiments, such as hysteretic energy levels shifts in external magnetic field, and abundance of low-energy excitations, motivated a lot of theoretical effort to describe the physics of nanoscale ferromagnetic systems[14, 50, 102, 62]. These works improved the understanding of ferromagnetism and tunneling transport in particles. On the other hand, some experiments are performed to directly investigate the magnetization of particles using magnetic force microscopy[54] and microSQUID (micro superconducting quantum interference device)[106, 70, 69, 91, 41, 90]. Radio-frequency (RF) field pulses can reduce the magnetization switching field of a Co particle, and ferromagnetic resonance at low temperatures can produce a bimodal distribution of the switching field.[91, 90]

In this chapter, I will explain a technique for fabricating Co particle devices with microwave leads and electron transport measurements of those devices under the influence of microwaves. This technique is used to study the effects of nanosecond microwave pulses on magnetic hysteresis loops of Co particles, by electron tunneling.

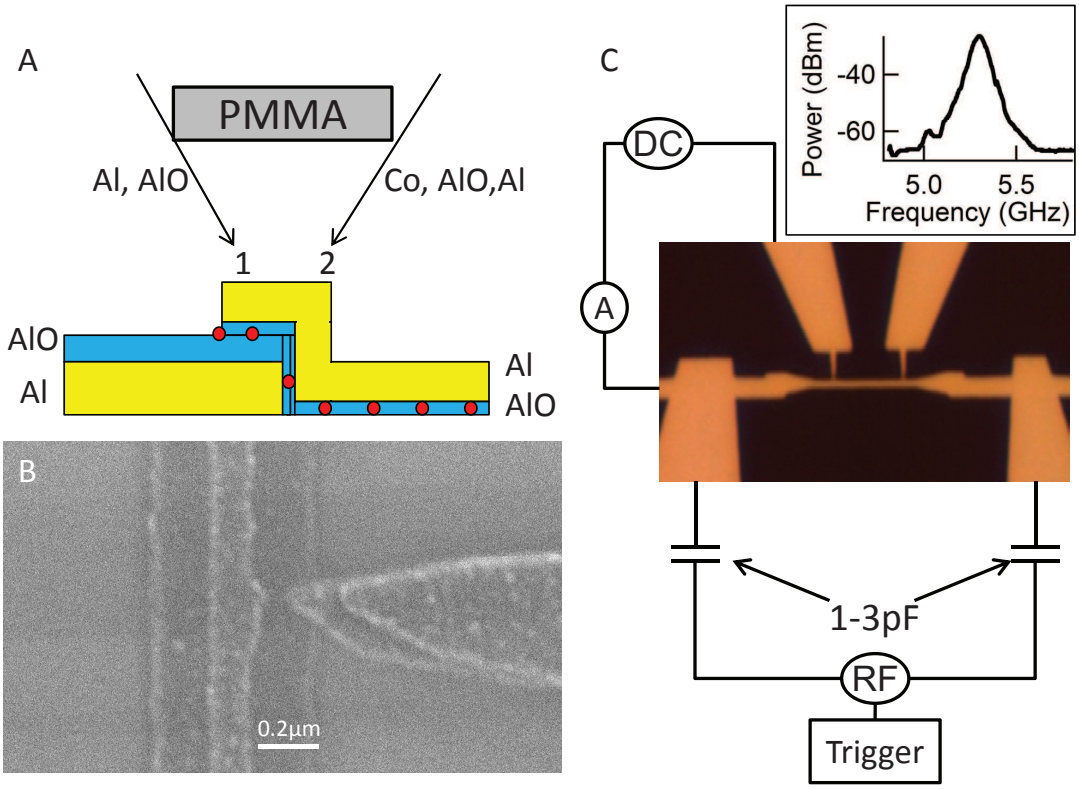

Figure 3.1: A: Sketch representing sample fabrication process. B: Scanning electron micrograph of a typical device. The scale bar indicates 0.2μm. C: Scheme of electrical circuit. Inset: Fourier spectrum of repeated microwave pulses.

It is confirmed that the heating effect on the sample due to the microwave pulses is very weak by using the I-V curve as a thermometer. Thus, the microwave field couples directly to the magnetization of the particles. We find that the magnetic energy delivered by individual pulses into the particle dissipates on the time scale of several microseconds. Our technique, which combines both electron tunneling and microwave pumping, can be used to explore magnetic properties from tunneling spectroscopy as well as magnetization dynamics.

3.2 Sample Fabrication

The samples are prepared by electron beam lithography (EBL) and shadow evaporation, similar to the technique described previously [17, 104]. First, a Poly(methyl methacrylate) bridge is defined by EBL over SiO_2 substrate. Next, we deposit 10nm of Al at 2×10^{-7} Torr base pressure along direction 1. Then, in the same direction, we deposit 1-1.5nm Al_2O_3 by reactive evaporation of Al[17], at a rate of 0.35nm/s. The oxygen pressure is kept at 2.5×10^{-5}Torr for 10-20s in the evaporation process, so the edge of the Al lead is also slightly oxidized. After that, we shut down the oxygen flow. When the pressure decreases to 10^{-7} Torr range, we rotate the sample by 32° and deposit 0.5nm Co along direction 2. At 0.5nm thickness, Co forms isolated particles with 1-4nm in diameter and spaced by 2-5nm[31]. Finally, we deposit another 1-1.5nm Al_2O_3 layer by reactive evaporation and top it with 10nm Al (Figure 3.1A). In each sample, there are two tunnel junctions with Co particles embedded in Al_2O_3 insulating matrix. The tunnel junction is formed by overlapping the finger like lead and the stripe like lead, as it is shown by Figure 3.1B. In this chapter, the number of particles in each junction is much larger than one. Due to the exponential dependence of the tunnel resistance on barrier thickness, only a few particles contribute significantly to transport, as will be shown. The Al strip lead is also used to apply the microwave pulses to Co particles. Figure 3.1C displays the circuit scheme of the experiment. During the measurements, a DC bias voltage is applied to one tunnel junction while the other one is left open. The microwave leads are coupled to the cable via two 1-3pF capacitors to electrically isolate the microwave circuit.

3.3 Experiment and Discussion

During the transport measurement, repeated nanosecond microwave pulses are applied on the measured device. The microwave is generated by an Agilent 83640B at a fixed power output level. The center frequency of the microwave is 5.3GHz which is in

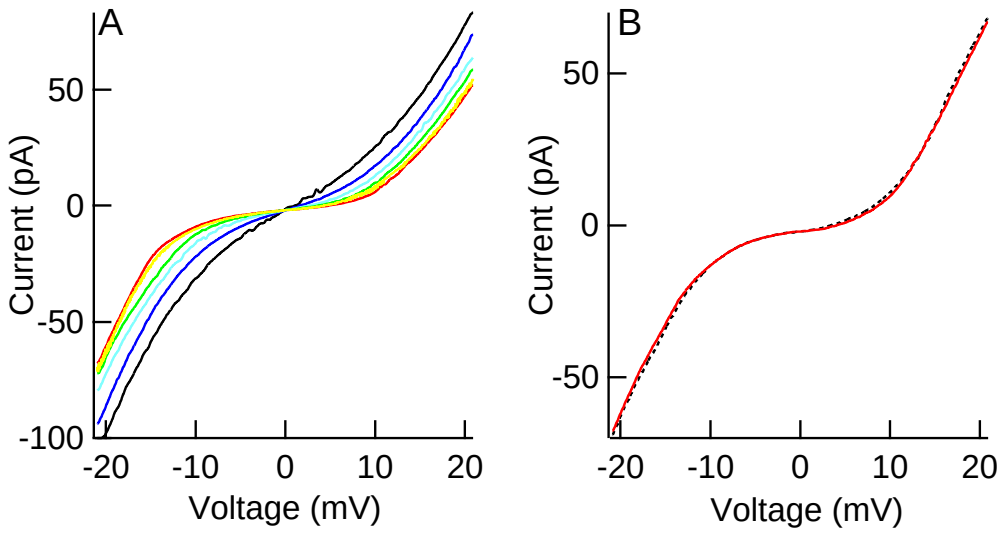

Figure 3.2: A: Average I-V curves at 27K, 16.6K, 13.1K, 9.3K, 5.8K, and 4.2K (from top to bottom at positive bias voltage). B: Average I-V curves at $T_s = 1000\mu$s (red/solid line) and 1.25μs (black/dashed line).

the range used in Ref. [90] . The spacing between pulses (T_s) is varied from 1000μs to 0.33μs using pulse modulation and a SRS-DS345 arbitrary waveform generator. The average single pulse duration is $\approx$ 8ns according to the statistics of real time measurements using microwave power detector and Lecroy 9370 oscilloscope. The calculation based on the Fourier spectrum of pulses taken by HP 8590E Spectrum Analyzer (inset of Figure 3.1C) also shows a similar pulse length.

First, we confirm that the microwave pulses applied have a negligible heating effect on the sample, by measuring the I-V curve of the sample. Figure 2A displays the I-V curves at different temperatures, from 4.2K to 27K. At a higher temperature, the current at certain bias voltage is stronger than it is at a lower temperature. Then, the I-V curve is measured at 4.2K under repeated microwave pluses with different T_s, as shown in Figure 3.2B. Each curve in Figure 3.2 is averaged over 2-5 voltage cycles. The I-V curve at $T_s = 1.25\mu$s is nearly identical to that at $T_s = 1000\mu$s, indicating that the heating effect of microwave pulses with spacing equal or larger than 1.25μs is still negligible. Next, we measure the tunneling current through particles versus magnetic

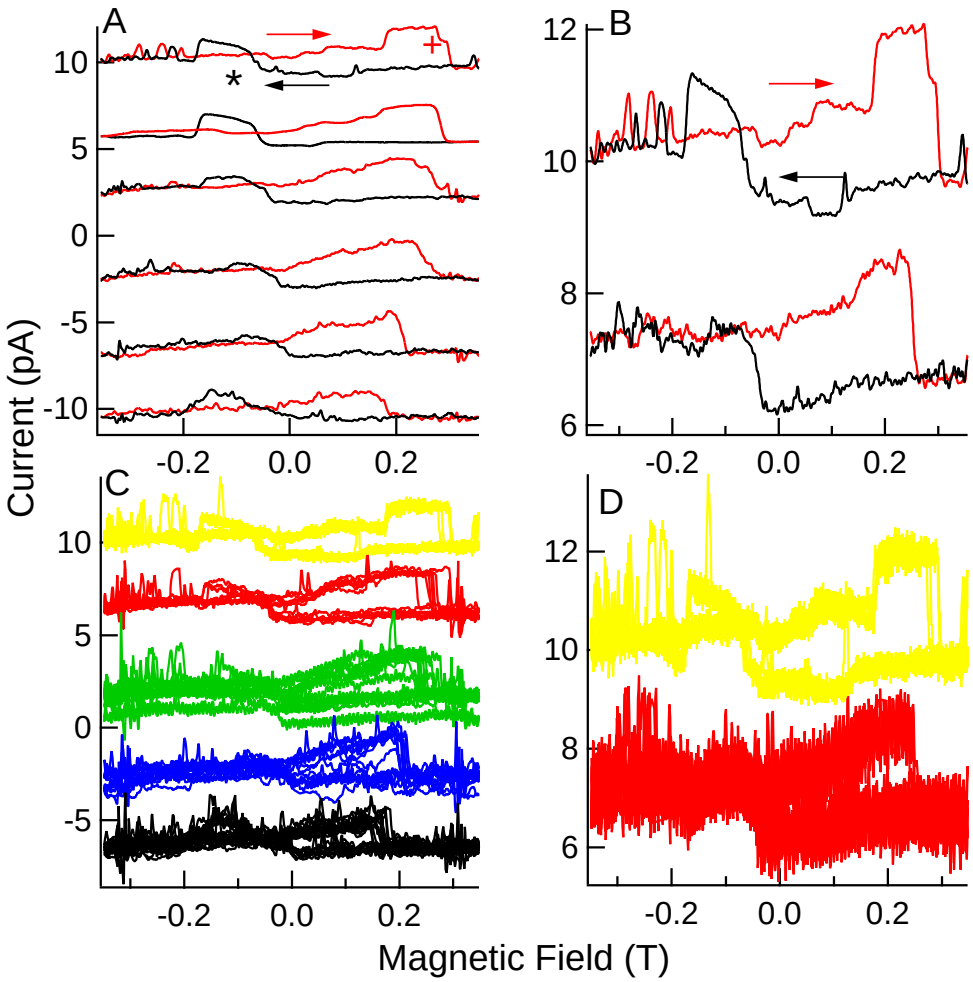

Figure 3.3: A: Average current loops at 4.2K when $T_s = \infty$ (no microwave), 1000μs, 10μs, 5μs, 2.5μs, and 1.25μs (top to bottom). The right and left arrow corresponds to increasing and decreasing magnetic field respectively. B: Average current loops at 4.2K and 7K (top to bottom). C and D: The raw data for A and B, respectively. Current loops with finite T_s in A and 7K in B are offset down with 4pA spacing.

field in the presence of repeated nanosecond microwave pulses at 4.2K . We fix the bias voltage at 10mV across the sample while sweeping the magnetic field and the results at different T_s are displayed in Figure 3.3A. We also measure the current hysteresis loops with the same bias voltage at different temperatures for comparison (Figure 3.3B). Each loop displayed in Figure 3.3 is averaged over 8-40 field cycles, while the one at 1000μs spacing is averaged over 700 cycles. Current loops with finite T_s and 7K are offset down with 4pA spacing for clarity. The current shifts with magnetic field are hysteretic with respect to the direction of the field sweep. The magnetoresistance (MR) in our samples is attributed to the magnetic field dependence of the discrete energy levels (see Sec. 1.1.2). This dependence has been studied in Refs. [31, 19] where the magnetic anisotropy energy was found to have a significant contribution. We have confirmed such dependence of the levels in our sample at dilution refrigerator temperatures[44]. The dependence of the levels on the applied magnetic field leads to MR at low temperature where the levels are well resolved. At 4.2K, energy levels broaden but some MR still remains[44]. In addition to the field dependence of the levels due to the magnetic anisotropy, magneto-Coulomb effect [67, 83, 68, 99, 8] may also contribute to the MR in our devices. So, the transition from low(high) current to high(low) current state during the sweep of magnetic field suggests magnetization reversal in Co particles. The width of the magnetic transitions in Figure 3.3 arises from averaging of the hysteresis loops over many field cycles. In individual hysteresis loops, the magnetic transitions are discontinuous, and switching field of the transitions fluctuates among different field cycles. Since different particles are likely to have transitions at different fields, the small number of magnetic transitions shows that only very few of particles are involved in transport. One transition indicated by cross in Figure 3.3A is observed in all hysteresis loops. Another transition indicated by star in Figure 3.3A is also clear except in the loop at $T_s = 1.25\mu$s.

When $T_s = 1000\mu$s, the hysteresis loop is nearly identical to that without microwaves, showing that a single microwave pulse is too weak to magnetically excite the Co particles. Reductions in switching field of the magnetic transitions are observed when the spacing between pulses decrease below 10μs, suggesting microwave triggered switch [91, 90] (Figure 3.3A). Figure 3.3B shows the similar reduction effect due to thermal fluctuations[65, 12]. At 1.25μs spacing, the switching field of the transition indicated by cross is reduced by $\approx 40\%$ compared with that at 1000μs. Meanwhile, the reduction of the switching field caused by a temperature increase from 4.2K to 7K is much weaker than 40%. Also, from the I-V curve (Figure 3.2B), the electron temperature in the leads at $T_s = 1.25\mu$s is estimated to be ≤ 4.4K. Similarly, the decrease in the switching field of the transition indicated by star when $T_s = 2.5\mu$s is larger than that at 7K. These results demonstrate that magnetic excitations in Co particles are pumped directly by microwave pulses, not by ordinary sample heating. The reduction of switching field is still observable at 10μs pulse spacing, which implies that the magnetic energy delivered by a single pulse does not completely dissipate in 10μs. This suggests that the spin relaxation time in our Co particles is on the order of microsecond. Long lower bounds of the spin-relaxation time T_1 in Co particles have been observed before.[19, 110, 44] Thus our measurement narrows down T_1 at 4.2K to the microsecond range.

We can use the I-V curve to estimate the magnetic field at the particle due to the RF current. The broadening of the I-V curve by the microwave pulses becomes visible in our measurement when the spacing between pulses is less than 0.625μs (Figure 3.4A). We also induce broadening of the I-V curve by injection of a continuous AC current at frequency 1.2kHz, instead of microwave pulses (after shorting the capacitors). The amplitude of the AC current I_{ac} can easily be determined using a standard lock-in technique. We use a low frequency transformer to isolate the AC circuit. Then we measure the I-V curve at different AC current, as shown in Figure

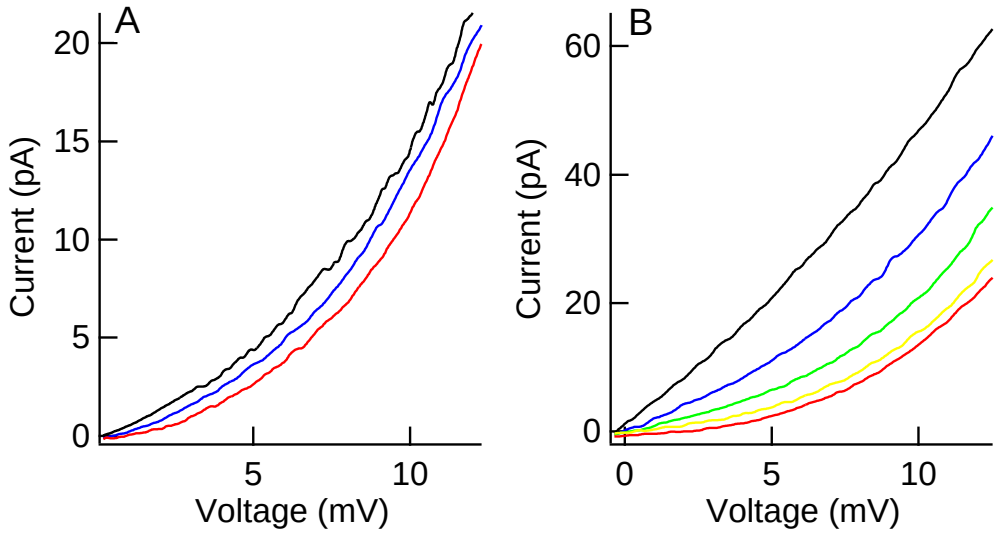

Figure 3.4: A Average I-V curves at $T_s = 0.333\mu$s, 0.625μs, 1000μs (top to bottom). B: Average I-V curves at $I_{ac} = 108\mu$A, 80μA, 53μA, 36μA, 15μA (top to bottom).

3.4B. By matching the I-V curve at different T_s and I_{ac}, we can find the power of microwave pulses with certain T_s from the amplitude of corresponding I_{ac}. Based on this result, we can solve the equations, $I(t) = \int_{-\infty}^{\infty} I(f)e^{i2\pi ft}\,\mathrm{d}f$, $P(t) = RI^2(t)$, and $\int_{-\infty}^{\infty} P(t)\,\mathrm{d}t/T_s = RI_{ac}^2$, where $I(f)$ is the current density of frequency and $P(t)$ is the power of a single pulse. Under the assumption that $|I(f)|^2$ is Gaussian distributed according to the Fourier spectrum, the expression for microwave induced current $I(t)$ in time domain is obtained after Fourier transform of $I(f)$. Then, we can find the amplitude of $I(t)$ by plugging this expression into the second equation. The amplitude of the RF-field on the particle is estimated to be $\approx 5 \times 10^{-4}$T from the lead geometry and $I(t)$.

CHAPTER 4

NONEQUILIBRIUM NOISE IN A FERROMAGNETIC NANOPARTICLE

4.1 Introduction

Recently, a lot of efforts are devoted to include very small ferromagnets in electronic devices, leading to the research of spintronics.[108, 39] Examples include giant magnetoresistance sensors, magnetic tunnel junctions, and spin-transfer torque nanopillars.[47, 3, 30, 63, 94, 89, 64, 48] As the diameter of a ferromagnetic particle decreases toward one nanometer, the particle's magnetization becomes highly susceptible to perturbations by the noise in the environment. Superparamagnetism is a well known example, where the magnetization of a ferromagnetic particle is perturbed by thermal noise. Above the blocking temperature, the particle loses the ability to maintain magnetic memory.[65, 12, 106] The magnetization of a ferromagnetic particle may also be susceptible to perturbations by electron transport.[23] At finite current through a ferromagnetic particle in a double barrier device, the magnetization can exhibit nonequilibrium noise.[102, 4, 66] Similar to how the thermal noise limits the size of magnetic memory, further miniaturization of spintronics may be limited by the nonequilibrium noise.

In this chapter, I will present an experimental study of nonequilibrium magnetization noise in a single nanometer-scale Co particle, which is attached between two Al leads by tunneling junctions. Tunneling spectroscopy of discrete levels in similar Co particles have been carried out previously.[31, 19] Magnetic anisotropy fluctuations were introduced to address the unexpected dependence of electron-in-a-box levels on the applied magnetic field.[19, 50, 51, 15, 16, 98] A much larger than expected

abundance of levels, observed in a Co particle, was explained by nonequilibrium spin excitations, described as a ladder of transitions between states with different spin of the particle (S_0).[50, 51] In these transitions driven by electron tunneling, only the ground states $|S_0, S_0>$ with different S_0 (spin ground states) are involved.[50, 51] Tunneling transitions between different magnetic states, which will be referred to as magnetic tunneling transitions, were not observed[19, 50, 51]. Examples of magnetic tunneling transitions could be $|S_0, S_0> \rightarrow |S_0 \pm 1/2, S_0 \pm 1/2 - n>$. Because of the spin-orbit (SO) interaction, the magnetic states become admixtures of $\hat{S}_Z$ eigenstates $|S_0, S_0 - n>$, which fluctuate among various particle eigenstates because of the magnetic anisotropy fluctuations. Thus, the tunneling selection rule $\Delta S_Z = \pm 1/2$ is not applicable. In that case, we would expect an abundance of magnetic levels in the tunnel spectrum, but the magnetic levels were not demonstrated. (In this chapter, a magnetic level (ω) refers to the magnetic energy difference between the final and the initial state in the magnetic tunneling transition.) Despite the absence in the experimental data, magnetic tunneling transitions are widely supported by prior theoretical work [14, 51, 16, 62]. The magnetic levels cannot be measured by tunneling spectroscopy for the following two reasons: (i) In a magnetic field where the Zeeman energy is much larger than the magnetic anisotropy energy per spin, ω is approximately equal to the Zeeman splitting, which is large enough to resolve by conventional tunneling spectroscopy.[76] But in that case, the admixing between different $\hat{S}_Z$ eigenstates becomes weak. Neglecting the admixing entirely, the tunneling matrix elements for magnetic tunneling transitions with low n are on the order $O(1/\sqrt{S_0})$, related to the Clebsch-Gordan (CG) coefficients[51]. The corresponding tunneling transition probability of order $O(1/S_0)$ is negligibly small, and only tunneling transitions between spin ground states ($|S_0, S_0> \rightarrow |S_0 \pm 1/2, S_0 \pm 1/2>$) retain significant weight.[14, 50, 51] As a result, in a strong magnetic field, all measured levels display linear dependence on magnetic field without Zeeman splitting.[31, 19] (ii) In the vicinity of the magnetic

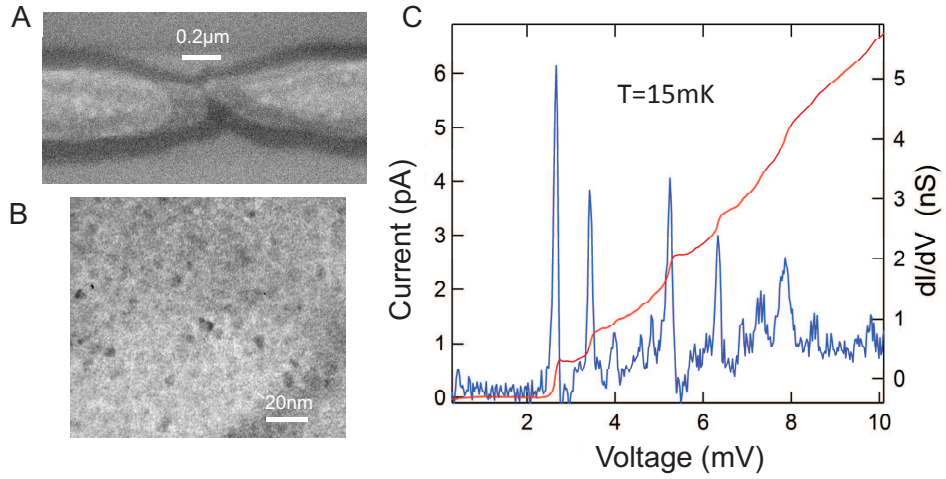

Figure 4.1: A: Scanning electron micrograph of a typical sample. B: TEM image of Co particles on aluminum oxide surface. C: Current (red) and differential conductance (blue) versus voltage for sample 1.

switching field before the magnetic switch, magnetic levels become so small that they cannot be resolved at experimentally accessible temperature [51, 62], even though the tunneling matrix elements for the magnetic tunneling transitions could be strongly enhanced by the SO-interaction, as will be discussed here. The main theme of this chapter is that the nonequilibrium noise is the strongest just below the switching field, where the magnetic levels are small compared to the anisotropy; while in the strong magnetic field, where the magnetic levels are much larger than the anisotropy, the nonequilibrium noise becomes negligibly weak.

4.2 Sample Fabrication

Our samples are made using electron beam lithography (EBL) and shadow deposition.[104] First, a polymethilmetachryllate (PMMA) bridge over a SiO_2 substrate is defined by EBL. Second, we deposit 10nm of Al and 1.5-3nm of Al_2O_3, along direction 1. Then we oxidize the sample at room temperature in O_2 at 3mPa, for 30s. Next, we deposit 0.5nm of Co, 1nm-1.5nm of Al_2O_3, followed by 10nm of Al, along direction 2. Sample resistance is varied by changing the oxide layer thickness. After lift-off in acetone,

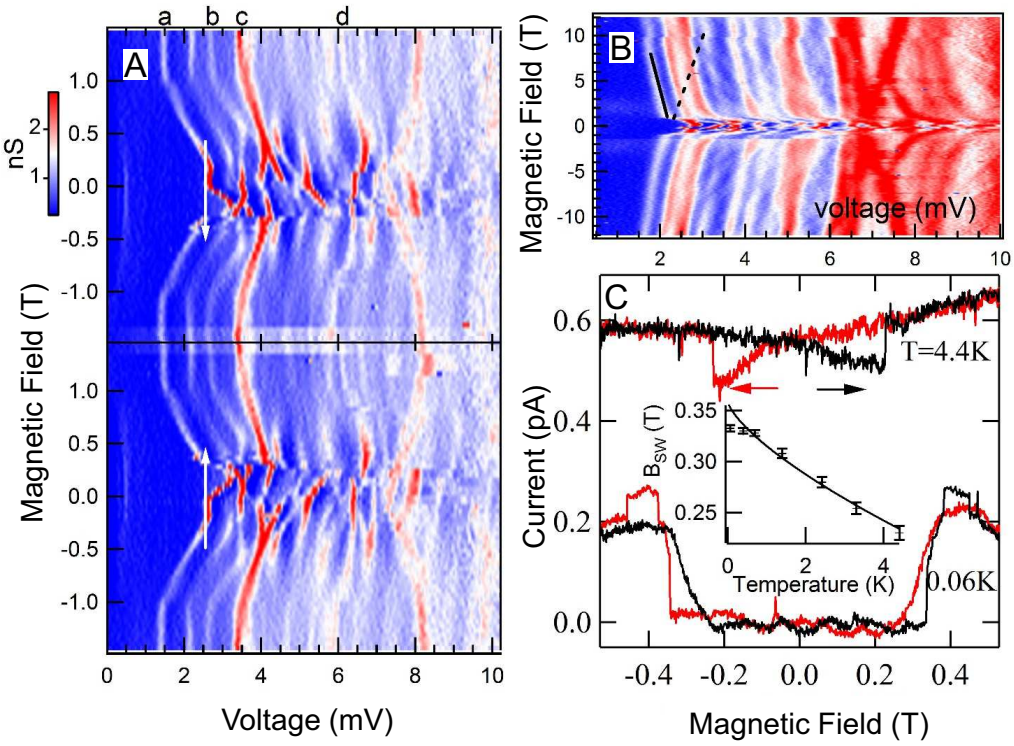

Figure 4.2: Sample 1. A and B: Differential conductance versus magnetic field and voltage at 60mK. Top and bottom panel in a correspond to decreasing and increasing magnetic field, respectively. Blue (red) regions correspond to low (high) conductance. **c**: Current versus magnetic field at voltage 2.4mV, at $T = 60$mK and 4.4K, with a current offset 0.4pA for clarity. Red (black) lines correspond to decreasing (increasing) magnetic field. Inset: Equilibrium switching field versus temperature.

the samples are ready to be wired up for measurement.

4.3 Experiment

4.3.1 Spectroscopic Measurements

Our samples consist of Co particles tunnel-coupled with two Al leads via aluminum oxide barriers. Co particles were formed by deposition of a thin Co film, with nominal thickness of 0.5nm, on aluminum oxide substrate. At this nominal thickness, we suppose that the deposited Co forms isolated particles of diameter 1-4nm, as demonstrated by prior work.[31] Figure 4.1A shows the micrograph of our typical device,

and Figure 4.1B displays a transmission electron microscope (TEM) image of aluminum oxide surface topped off by Co film with the nominal thickness 0.5nm. The image in Figure 4.1B is lower in resolution, but generally in agreement with the TEM image in Ref. [31], which showed that Co particles are darker than the substrate. The diameters of the particles in Figure 4.1B appear to be in the similar range as in Ref. [31]. 36 samples were studied in detail at 4.2K, and approximately two thirds of those samples display bias voltage dependence of the switching field similar to that discussed here. The remaining samples did not display bias voltage dependence of the switching field. Four samples were studied in detail at dilution refrigerator temperature, the main results discussed in this chapter have been confirmed in three of those samples. In this paper we discuss the electron transport properties in one sample at dilution refrigerator temperature, and in another sample at 4.2K.

Figure 4.1C shows the current-voltage characteristics, $I(V)$, and the tunnel spectrum, $\mathrm{d}I/\mathrm{d}V$ of sample 1 at $T = 15$mK and zero applied magnetic field. The low voltage region where the current is negligibly small indicates Coulomb blockade, while the steps in the $I(V)$ curve indicate discrete levels, similar to the prior work.[76] The Coulomb-blockade voltage threshold is the voltage at the first maximum in $\mathrm{d}I/\mathrm{d}V$. The particle size will be estimated later in the text. Those $I(V)$ curves are measured using an Ithaco 1211 current amplifier and are highly reproducible with voltage sweeps. Some of our samples have finite conductance below the lowest discrete level. This conductance is explained in terms of direct tunneling between the leads, through the aluminum oxide surrounding the particle. We refer to it as a leakage conductance of the junction. To correct for the leakage conductance in sample 1, we subtract a linear slope of 0.35nS from the $I(V)$ curves.

Figure 4.2A and B displays the magnetic field dependence of the tunneling spectrum, for decreasing and increasing magnetic fields. During the measurements, the magnetic field varies at a rate of 0.26mT/s, while the bias voltage varies between

-10.2mV and 10.2mV at a rate of 0.25mV/s. The sample wiring is filtered at the mixing chamber using a copper powder filter and a high-loss coaxial wiring with $10MHz$ bandwidth. The sample is in a Faraday cage and the filter output is connected coaxially with the cage. There are no unfiltered wires entering the cage. We usually obtain electron temperatures <100mK (measured from the line-width of discrete levels in normal metal particles). In Figure 4.2C and 4.3A-B, the magnetic field sweep rate is 8mT/s. The temperature dependence of the switching field (inset of Figure 4.2C) and the standard deviation is obtained by averaging over up to 32 magnetic field sweeps. The tunneling spectrum of Co particle shows symmetric hysteresis about zero magnetic field. Discrete levels correspond to the maximum in conductance. All levels are discontinuous at the same switching field $|B_{sw}| \approx 0.3$T, confirming that they belong to the same particle. To convert from voltage to electron energy in units of eV, the voltage needs to be divided by $1 + 1/c$, where $c = 1.59$ is the capacitance ratio, obtained as the ratio of the magnitudes of the Coulomb-blockade voltage thresholds at negative and positive bias. The size of the sudden jump in energy levels fluctuates: levels a,b,c, and d,(Figure 4.2A) change discontinuously by -0.3meV, 0.07meV, -0.09mev, and 0.15meV, respectively. In addition, there is a continuous dependence of the levels versus magnetic field, which also varies among levels. These properties are in agreement with the prior experimental work [31, 19] and theory[15, 98]. The fluctuations in the discontinuity among different levels were explained in terms of the fluctuations in the magnetic anisotropy energy among different particle eigenstates.[19, 50, 15, 98] All the low-lying levels displayed in Figure 4.2A shift down in voltage with the magnetic field, with approximately the same slope. As explained in Ref. [19], in that case, the measured levels correspond to the tunneling transitions where an electron tunnels off the minority electron-in-a-box states, without exciting the particle magnetically. The one level that shifts up in voltage, between 7mV and 8mV, is a majority electron-in-a-box level.

4.3.2 Temperature dependence of equilibrium switching field

We measure the temperature dependence of the equilibrium switching field, i.e. the switching field at zero current. We set the voltage to 2.4mV and measure the magnetic hysteresis loop, following the white arrows in the (B,V) space shown in Figure 4.2A. At low temperatures, if the magnetic field is just below the switching field, the particle will face Coulomb blockade. As the magnetic field is increased and reaches the switching field, the transition to a current-carrying state takes place. Since the sequential tunnel current is zero before the switching, this switching field is the equilibrium switching field. The magnetic hysteresis loop for two different temperatures is displayed in Figure 4.2C, with the inset showing the temperature dependence of the equilibrium switching field. The error bar is the standard deviation (S.D.) of the equilibrium switching field. The S.D. increases versus temperature. At 4.2K, thermal broadening produces a current of ≈0.1pA preceding the switching event, but the current is still small enough to have negligible nonequilibrium effect on the switching field (see the next paragraph). The decrease of the equilibrium switching field accompanied by an increase in the S.D. with temperature indicates thermally activated switching [32, 27, 106].

The equilibrium switching field dependence on temperature can be fitted to the Néel-Brown model based on the formula used in the experimental study of magnetization reversal in a single ferromagnetic particle (Refs. [65, 12, 106]) :

$$\frac{B_{sw}}{B_0} = 1 - \left\{ \frac{k_B T}{E_B} ln \left[\frac{cT}{v \left(1 - \frac{B_{sw}}{B_0}\right)^{\beta-1}} \right] \right\}^{1/\beta} . \tag{4.1}$$

Here, B_0 is the switching field at $T = 0$ and $I = 0$, E_B is the energy barrier in $\mathcal{H}(\vec{B}, S_Z)$ between the initial and the final magnetic states, $v = dB/dt$ is the magnetic field sweep rate, $c = k_B B_0 \nu_0/(\beta E_B)$, where β is equal to 3/2,(Refs. [106, 100]) and ν_0 is the attempt frequency, dependent on α, B, and T. Parameters B_0, E_B, and ν_0 are free.

From the fitting, we obtain B_0 =0.359±0.036T for the equilibrium switching field at zero temperature E_B =20.6±2meV for the energy barrier for switching extrapolated to zero magnetic field. (For a magnetic field B in the vicinity of B_0, the energy barrier is $E_B(1-B/B_0)^{3/2}$.[100, 106]) The fit is shown by the solid line in the inset of Figure 4.2C.

In order to characterize the Co particle, we use a magnetic model-Hamiltonian with uniaxial anisotropy K, based on Stoner-Wohlfarth (SW) model,

$$\mathcal{H}(\vec{B}, S_Z) = -g\mu_B \vec{B} \cdot \vec{S} - KS_Z^2/S_0. \tag{4.2}$$

The easy-axis is in Z direction, and S_0 is the total particle spin in units of $\hbar$. The SO-interaction in this Hamiltonian is described by a single magnetic anisotropy constant K, which we refer to as trivial SO-interaction. $g = 1.25$ is obtained from the difference in slopes of minority and majority electron-in-a-box levels in Figure 4.2B. Because the energy levels of the Co particle discussed here exhibit continuous magnetic field dependence before the magnetic switch, which demonstrates that there is a continuous rotation of the magnetization before the switch, the easy-axis cannot be collinear with the magnetic field. Similarly, the easy axis cannot be perpendicular to the magnetic field, because there would be no discrete magnetic switching in that case. We have confirmed that using 15-75 degrees as angle between the easy-axis and the magnetic field produces similar result in the analysis. Thus, we use 45 degrees in further analysis, which is the same assumption as in Refs. [19, 50]. The SW-switching field B_0 for the Hamiltonian given by Eq. 4.2 could be obtained from $g\mu_B B_0 = K$, which is the equilibrium magnetic switching field at zero temperature. B_0 is 0.359T from the temperature dependence of switching field discussed above, so $K = 26.0\mu$eV. At 45 degrees, we obtain from Eq. 4.2 that $S_0 = 3\sqrt{3}E_B/(4\sqrt{2}g\mu_B B_0) \approx 728$. This corresponds to a hemispherical particle with diameter 2.6nm and the number of Co atoms $N_a = 882$.[14]

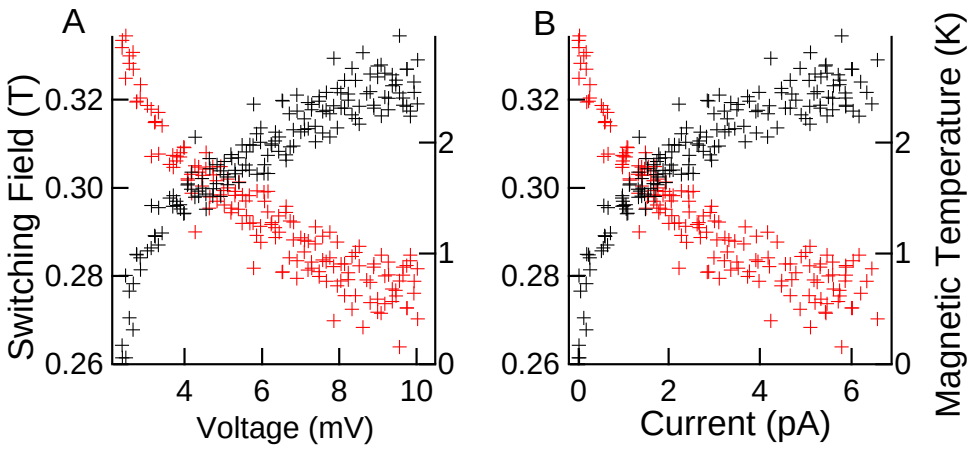

Figure 4.3: A and B: Magnetic switching field (red) and magnetic temperature (black) versus voltage and current, respectively, in sample 1 at 60mK.

4.3.3 Current and voltage dependence of switching field

Now, we study the effect of bias voltage and tunnel current on magnetic switching at T =60mK. We set a bias voltage, vary the applied magnetic field, and measure the tunnel current. Figures 4.3A and B, show the magnetic switching field versus voltage, and the current recorded immediately prior to the switching, respectively. Note that the tunnel current of 0.1pA at 60mK has negligible effect on the switching field. At 10mV, the magnetic switching field is reduced by 15% compared to the equilibrium switching field at 60mK. It can also be seen that the decrease in the switching field with bias is accompanied by an increase in the noise of the switching field. The equilibrium switching field at 60mK has a S.D. of 3.1mT, while the S.D. at 8mV bias voltage is 4.7mT. The magnetic temperature (T_M) at voltage V and current I can be defined as the temperature at which the equilibrium switching field equals the switching field at voltage V and current I and base temperature (60mK in our magnetic field sweeps). T_M can be obtained by linearly interpolating the switching field measured at voltage V and base temperature to the temperature dependence of the equilibrium switching field. As temperature is an indicator of thermal noise intensity, magnetic temperature T_M serves to represent the level of nonequilibrium magnetization noise.

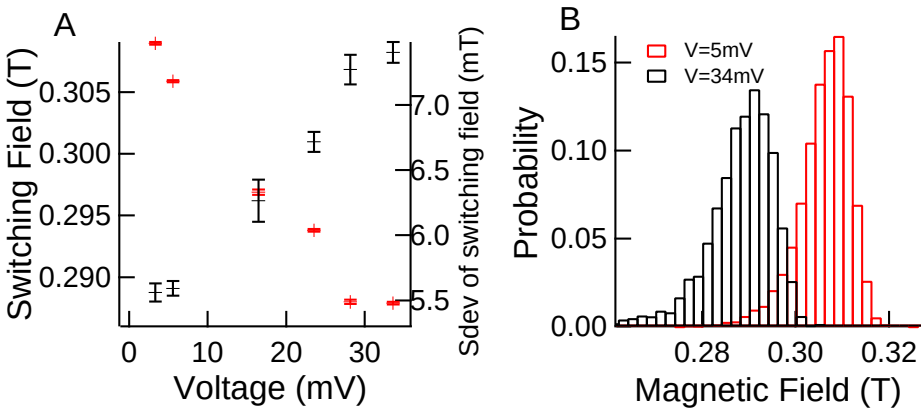

Figure 4.4: A: Magnetic switching field (red) and standard deviation of switching field (black) versus voltage in sample 2. The error bars are the standard errors. B: Probability distribution of switching field for 5mV (red) and 34mV (black).

For example, at 8mV, the average magnetic switching field is 0.281T. A switching field of 0.281T is the same as the interpolated equilibrium switching field at 2.36K. Thus, T_M at 8mV is 2.36K. The S.D. of the equilibrium switching field at 2.36K is 4.9mT, close to the S.D. of the switching field at 8mV and 60mK, confirming that the reduction in switching field is well described by the concept of magnetic temperature. The physical interpretation of $k_B T_M$ is the average magnetic excitation energy in the steady state. The voltage dependence of the switching field cannot be interpreted in terms of a simple shift in magnetic anisotropy with bias voltage, as described in Refs. [105, 21, 61, 95], because in our case, the noise increases with bias voltage. If the switching field simply shifted down due to the change in anisotropy with voltage, the noise would also go down, because the switching field noise scales with the switching field. [106, 53] The magnetic temperature versus voltage and current is shown in Figures 4.3A and B, respectively.

Figure 4.4A displays the bias voltage dependence of the switching field as well as the S.D. in sample 2, at 4.2K. In this sample, the magnetic hysteresis loop was measured nine hundred to five thousand times for different bias voltages, enabling us to obtain the statistical distribution of the switching field. As seen in Figure

4.4B, the distribution is asymmetric, as expected for thermally activated magnetic switching.[53] As the bias voltage increases, the distribution broadens asymmetrically, indicating again that the noise increases.

4.4 Discussion

The observation that the switching field distribution widens with current, brings a question if simple Joule heating in the environment is responsible for the noise increase. The answer is no because of the following three reasons. First, we take advantage of the full-width-half-maximum (FWHM) of the levels. It is known that the FWHM of a discrete level in a quantum dot is $\approx 3.5 k_B T_e$, where T_e is the electron temperature in the lead. After conversion from voltage to energy, FWHM becomes 75μeV and 86μeV, for the levels at 2.4mV and 6.3mV in Figure 4.1C, corresponding to T_e of 0.25K and 0.28K, respectively. So the magnetic temperature is at least an order of magnitude larger than the electron temperature in the leads. Note T_e is significantly larger than that obtained by tunneling spectroscopy of discrete levels in Al particles, implying an additional broadening mechanism in the Co particle. Second, we have estimated the increase in phonon temperature in the particle. Assuming the power input of IV = 40fW (at 8mV) into the phonon bath is uniform within the volume of the particle, and heat conductance through the tunnel barrier 2.5×10^{-5}W/K-cm for Al_2O_3 at 60mK,[78] we find an increase in the phonon temperature to be in the mK-range. Third, it would be in disagreement with prior work that applied power of 40fW could raise the temperature of the particle from mK to 2K. For example, in Ref. [76], the electron temperature remains well below 0.5K when an order of magnitude larger power was applied to a similarly sized Al particle.

We conclude that the electron tunneling is responsible for the direct deposition of the magnetic energy in the particle, without heating up the environment. At a

fixed bias voltage, let E_M and ϵ denote the magnetic excitation energy and its increment in an electron tunneling event, respectively, averaged over a large number of electron tunneling events. If the SO-interaction is trivial, then ϵ will be independent of E_M provided $E_M \ll E_B$. [102] That is, the average energy transfer into the magnetic subsystem per electron tunneling event, is independent of the initial magnetic energy. As will be shown here, that remains to be the case even if the nontrivial SO-interaction is included. Then, E_M varies versus time according to the differential equation $\mathrm{d}E_M/\mathrm{d}t = \epsilon 2I/e - E_M/T_1$, where T_1 is the magnetization relaxation time. Here we assume that ϵ is pumped at the rate $2I/e$, since there are two energy deposition events in one sequential tunneling cycle, one for electron tunneling on, and one for electron tunneling off. (At low bias voltage and/or with a trivial SO-interaction, ϵ may be different for electrons tunneling on and off,[102] which could reduce the pumping rate by factor of up to two. In addition, here we neglect any other transitions that can deposit magnetic energy from the electronic subsystem. For example, an internal energy relaxation process in the particle may involve a magnetic transition. We expect that such internal relaxation events do not change the pumping rate significantly, because an internal relaxation process must be preceded by a tunneling process. Thus, the internal relaxation rate is limited by the tunneling rate I/e.) The average magnetic excitation energy in the steady state, which could be indicated by the magnetic temperature, becomes

$$k_B T_M = \epsilon T_1 2I/e. \tag{4.3}$$

As discussed earlier, most of the levels displayed in Figure 4.2B are minority electron-in-a-box levels that do not involve magnetic levels. If the magnetic tunneling transitions were also observed in the tunneling spectra, then those minority electron-in-a-box levels would split by ω. The black line in Figure 4.2B indicates the lowest conductance maximum, which moves down in voltage versus field. The black dashed line in Figure 4.2B is an example of where a magnetic level is expected, assuming

ω is the level spacing from the magnetic Hamiltonian in Eq. 4.2. If the magnetic level were detected, it would present as a local maximum in the conductance versus voltage, which moves following the dashed line. Evidently, the magnetic level is absent, in agreement with the prior published work. [31, 19] Theoretically, if the SO-interaction was trivial, then we would expect that $\epsilon \approx \omega/2S_0 \approx 0.0007\omega$, which would certainly explain the absence of magnetic levels. The factor $1/2S_0$ is the probability of a magnetic transition in a tunneling event, related to the square of the CG coefficient involved in that transition. [14, 50, 51, 102]

Now, assume $\epsilon \approx 0.0007\omega$ is valid in the magnetic field just below the magnetic switching field. We obtain ω as the level spacing in Hamiltonian 4.2 above the metastable spin-ground state. Then, according to Eq. 4.3 and the data in Figure 4.3, we obtain T_1^{-1} to be in the kHz range. The magnetization relaxation rate reached here seems unphysical, as it is much smaller than that generally measured by ferromagnetic relaxation.[36] This problem can be resolved if ϵ is strongly enhanced just below the switching field, meaning that the magnetic levels are significantly more involved in electron tunneling. Such an enhancement of ϵ near the switching field would not be possible if the magnetic transition probabilities are governed exclusively by the CG coefficients. [14, 51, 102]

Clearly, the effects of SO-interaction on magnetic tunnel transitions need to be considered beyond the magnetic Hamiltonian in Eq. 4.2. In the simplest non-trivial approach, we invoke the magnetic model-Hamiltonian for a single Co particle from Refs. [19, 50],

$$\mathcal{H}_N(\vec{B}, S_Z) = -g\mu_B \vec{B} \cdot \vec{S} - K_N S_Z^2/S_0, \tag{4.4}$$

N is the total number of electrons in the particle. In the regime of sequential electron tunneling, N can only vary by 1. This model-Hamiltonian was used successfully to account for the magnetic field dependence of the low-lying levels in the tunneling spectra of Co particles consistent with our work. In contrast to Eq. 4.2, K_N now

fluctuates with N as well as different particle eigenstates involved in each electron tunneling event[19, 50, 51, 15, 98]. Since the statistics from four levels in Figure 4.2A is insufficient to obtain the standard deviation $\sigma(\Delta K_N)$ reliably, we use the theoretical value $\sigma(\Delta K_N) = 0.4\mu$eV for the particle with $N_a = 882$, which is "of the order needed to account for the experimental data"[98].

Because of the fluctuations in K_N[19, 50, 51, 15, 98], many matrix elements of the tunnel Hamiltonian, taken between magnetic states corresponding to different K_N, become large in the vicinity of B_0 resulting in a much larger ϵ. We have derived a formalism, which describes the nonequilibrium distribution among magnetic states at finite bias voltage, using the tunnel Hamiltonian and master equations [102] as well as the model-Hamiltonian with fluctuating anisotropy. The discussion of this formalism is beyond the scope of this chapter. The formalism shows that a simple classical model can be applied to predict the magnetic temperature in the regime of our experiment, so in the remainder of this paper we will use the classical approach only, for simplicity.

Despite the complexity of anisotropy fluctuations, our analysis can be carried by using two different anisotropy constants in $\mathcal{H}_N(\vec{B}, S_Z)$ for N and $N+1$. We can set $K_N = 26.0\mu$eV and $K_{N+1} = K_N + \sigma(\Delta K) = 26.4\mu$eV. Figure 4.5A shows the magnetic energy of the particle versus $m_Z = S_Z/S_0$, using the classical energy corresponding to the Hamiltonian given by Eq. 4.4, for B=0.281T, K_N and K_{N+1}. The minima in energy are metastable, that is, they correspond to the magnetization directions before switching. We assume that the initial magnetization direction corresponds to the minimum for the anisotropy constant K_N. Next, an electron tunneling onto the particle changes the anisotropy constant to K_{N+1}. Tunneling can be considered as instantaneous, because the magnetization precession time ($\hbar/K_N$) is much larger than the time to tunnel under the barrier. In that regime, the tunneling transition is represented by the vertical arrow in the figure. The magnetization is now excited

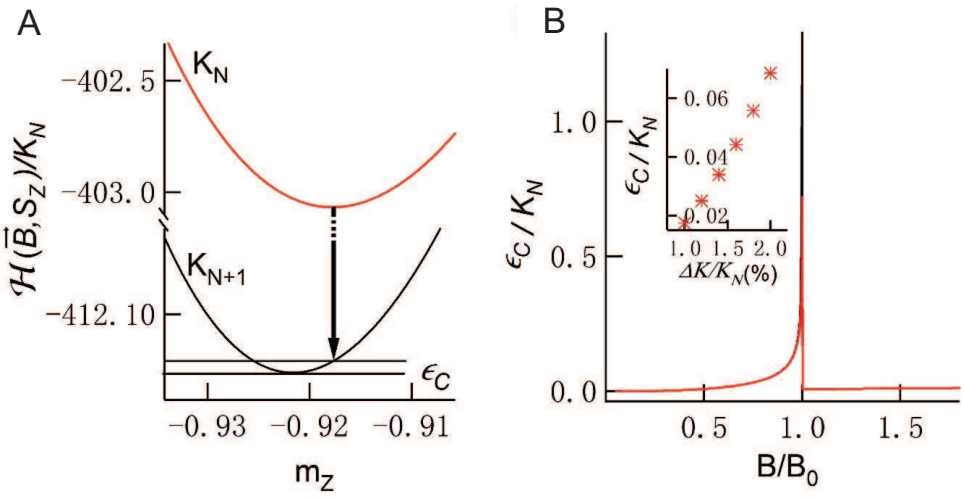

Figure 4.5: A: Hamiltonian of single Co particle versus $m_Z = S_Z/S_0$ for K_N and K_{N+1} at $B = 0.281$T. $B_0 = 0.359$T is the SW-switching field for K_N. The arrow indicates the transition from N to $N+1$-electron state. ϵ_C is the classical magnetic excitation energy induced by the transition. B: Magnetic excitation energy versus magnetic field. ϵ_C is induced by single electron tunneling onto the particle. Red (black) line corresponds to the result from classical (quantum mechanical) approach. Inset: ϵ_C versus ΔK at $B = 0.281$T.

with the classical excitation energy $\epsilon_C = \mathcal{H}_{N+1}(\vec{B}, S_{Z,eq}^{K_N}) - \mathcal{H}_{N+1}(\vec{B}, S_{Z,eq}^{K_{N+1}})$. Here $S_{Z,eq}^{K_X}$ represents the metastable equilibrium S_Z of Eq. 4.4 at X-electron state. Figure 4.5B shows that ϵ_C increases as the magnetic field approaches B_0. For comparison, in Figure 4.5B, we plot ϵ using the quantum mechanical approach mentioned earlier. The results from the two approaches agree with each other very well, except in the close proximity of the SW-switching field $B_0 = K_N/g\mu_B$. However, in our experiment, the magnetization of the particle always switches before the magnetic field reaches this regime where the classical method breaks down. ϵ_C has a maximum $2S_0\sqrt{2[\sigma(\Delta K)]^3}/3\sqrt{3K_N}$ immediately before the magnetic switch at $B = B_0$. It drops to $S_0[\sigma(\Delta K)]^2/12\sqrt{3}K_N$ immediately after the magnetic switch at the SW-switching field. In a field $B \gg B_0$, $\epsilon_C = S_0[\sigma(\Delta K)]^2 B_0/2K_N B$ which is much smaller than the magnetic level $\omega \approx K_N B/B_0$. This behavior of ϵ_C is consistent with the observation that the magnetic temperature increases with bias in the vicinity of

the switching field, while there are no signatures of magnetic levels in the tunnel spectra in a strong magnetic field. The classical excitation energy increases with $\Delta K = K_{N+1} - K_N$, indicating that anisotropy fluctuations plays the crucial role in delivering magnetic excitations (Figure 4.5B inset). ϵ_C becomes comparable to $\epsilon \approx \omega/2S_0$ (the average magnetic excitation energy per tunneling event if the SO-interaction were zero or trivial) at the magnetic field of $S_0 B_0 \sigma(\Delta K)/K_N \approx 10B_0$, which is independent of the particle's volume. Thus, the magnetic tunneling transitions are governed by the CG coefficients in a magnetic field above approximately $10B_0$, while below that field, the magnetic tunneling transitions are governed by the SO-interaction. This is an important result of this chapter. Interestingly, the same factor $S_0 \Delta K/K$ accounts for the enhancement of the discontinuities of the electron-in-a-box levels at the switching field[19].

Next, we use the stochastic LLG equation to model magnetization dynamics,[36, 55]

$$\frac{\partial \vec{m}}{\partial t} = -\vec{m} \times [\vec{h}_{eff} + \alpha \vec{m} \times \vec{h}_{eff}], \tag{4.5}$$

where $\vec{m}$ is the unit vector of magnetic moment, α is the phenomenological damping parameter and $\vec{h}_{eff} = \nabla_{\vec{m}} \mathcal{H}_N/S_0$ is the effective magnetic field with time dependent noise $K_N(t)$, which reflects the mesoscopic fluctuations in K_N. By numerically solving the LLG equation, we obtain the time dependence of the classical magnetic excitation energy E_M driven by $K_N(t)$. The numerical solution shows that E_M, averaged over a time interval much longer than the correlation time for K_N and much shorter than T_1, will increase linearly versus time, if it is initially at 0 . This verifies the hypothesis used in the derivation of Eq. 4.3 that ϵ is independent of E_M. The magnetic temperature is obtained as the steady state value of E_M, averaged over time. The numerical solution confirms Eq. 4.3, $k_B T_M \approx \epsilon_C \delta f T_1$, where δf is the rate at which K_N changes. The resulting T_1^{-1} is now in the MHz range, which is more realistic than that obtained from the CG coefficients [14, 102], demonstrating the relevance

of our approach. The magnetization relaxation rate obtained here is consistent with the previous reports.[19, 110, 43]

Thus, we find that electron tunneling through a nanometer-scale Co particle can excite nonequilibrium magnetization noise at very low temperatures. This noise can reduce the magnetic switching field as well as broaden its distribution. The noise is strongly enhanced in the vicinity of the magnetic switching field. Magnetic anisotropy fluctuations among different particle eigenstates, caused by the spin-orbit interaction, provide a natural explanation of the noise properties.

The results presented in this chapter may have ramifications with respect to further miniaturization of spin electronics. It suggests that, other than simple heating, nonequilibrium could present as an explanation for the reduction in switching field. If one of the leads were ferromagnetic, then the magnetization of the ferromagnetic particle could be switched by the STT mechanism. [101] Relatively long T_1 suggested in a Co particle [19, 110, 43] also implies that the critical current for STT-switching should be reduced, because the critical current in STT-switching generally scales with magnetization relaxation rate.[84] But, since the magnetic tunneling transitions in a Co particle at low field seems to be governed by the SO-interaction which produces anisotropy fluctuations beyond experimental control, it would appear that STT-switching cannot be realized in a Co particle in a double barrier device. That is, the effect of STT would be negligibly weak compared to the effect of nonequilibrium noise.

CHAPTER 5

SIZE-DEPENDENCE OF MAGNETO-ELECTRONIC COUPLING IN CO PARTICLES

5.1 Introduction

In the emerging era of spin-based electronics, understanding the coupling between electron transport and magnetization in single nanometer scale ferromagnetic particles is essential. In this field, electron tunneling spectroscopy has been proven to be very useful. Rich physical phenomena was revealed in difficult experiments, including abundance of energy levels and hysteretic dependence of those levels with the applied magnetic field, [31, 19, 44] which stimulated a lot of theoretical work. [14, 50, 51, 98, 102] For example, magnetic anisotropy fluctuations were introduced to explain a larger-than-expected jump in energy levels upon a magnetic switch. [19, 50, 51, 15, 16, 98] The fluctuations are analogous to the universal conductance fluctuations in mesoscopic physics, where the conductance of a mesoscopic conductor fluctuates as a function of external parameters and microscopic disorder. [103] Similarly, the magnetic anisotropy energy of a Co particle fluctuates among its eigenstates and electron number.

As the particle approaches nanometer-scale, the magnetization of the particle becomes more susceptible to the noise in the environment such as thermal fluctuations and electron transport. [65, 12, 23, 102, 4, 66] A recent experimental study discovered that nonequilibrium magnetization noise can be induced by sequential electron tunneling through single, nanometer scale Co particles in double barrier devices. [44] To summarize, the magnetic energy of the Co particle (E_M) can be significantly increased by the tunneling current, even though the heat bath temperature remains low

and nearly independent of the current. The strength of the nonequilibrium noise is characterized by effective magnetic temperature (T_M). The physical meaning of T_M is that $k_B T_M$ is the average of E_M in the steady state, at a certain bias voltage and tunneling current through the particle. This magnetic heating occurs because tunneling transitions between various magnetic states, or the magnetic tunneling transitions, are allowed due to the spin-orbit (SO) interaction in the particle. The magnetization relaxation rate also needs to be smaller than the rate of the magnetic tunneling transitions, in order that T_M be substantially larger than the temperature in the heat bath. The mesoscopic fluctuations in magnetic anisotropy play a central role in driving the magnetic excitation due to electron tunneling in single Co particles. The anisotropy Hamiltonian of the particle differs before and after the tunneling, so the magnetic eigenstates of the particle involved in the tunneling process are not orthogonal. If an electron tunnels onto the particle, the probability of various magnetic excited states after tunneling is given by the overlaps of the magnetic eigenstates before and after tunneling. So, as the electrons tunnel via the particle sequentially, E_M increases until the rate of magnetic excitation becomes balanced by the magnetic relaxation, thereby leading to the steady state magnetic temperature at a certain bias voltage and tunneling current.

In order to further verify this model, we perform electron tunneling measurements of magnetic hysteresis loops of Co particles that are large compared to the size of the particles studied in prior work. [31, 19, 44] The size dependence of the magnetic anisotropy fluctuations were investigated by Usaj and Baranger, [98] using a random matrix model for the SO coupling. For uniaxial anisotropy in Co, they obtain the standard deviation ($\sigma(\Delta K)$) for the anisotropy constant (K), due to adding an electron to the particle. $\sigma(\Delta K)/K$ is found to vary inversely with the number of atoms (N_a) in the particle. In our experiment, the magnetic switching field of the Co

particles decreases versus tunneling current, which is attributed to the nonequilibrium magnetization noise induced by electron tunneling. However, our experimental result shows that for a fixed tunneling current at mK phonon temperature, the magnetic temperature at the switching field has much weaker size dependence than the magnetic anisotropy fluctuations. Although at first this result appears to be contradictory to the theoretical prediction, the discrepancy is reconciled by the physical picture discussed in this paper.

Later in this chapter, I will present a phenomenological model that incorporates mesoscopic fluctuations of the magnetic anisotropy energy, to address the weak size dependence of the magnetic temperature at the switching field. This model uses a quantum mechanical master equation to carry our discussion in this paper. In large Co particles, the reduction in magnetic switching field due to thermal noise is much weaker than that in small particles. [12, 106] We will show that the same relation applies to the nonequilibrium noise. This allows for the particle to be much closer to the ideal Stoner-Wohlfarth (SW) switching field [88] before the switch occurs. As the applied magnetic field approaches the SW switching field, the magnetic level spacing decreases significantly, which makes the magnetic states more strongly perturbed by the anisotropy fluctuations. Consequently, the probability of magnetic tunneling transitions increases dramatically. So, on one hand, the probability of magnetic tunneling transitions is enhanced at the observed switching field, while on the other hand, the anisotropy fluctuation amplitude, $\Delta K \sim 1/S_0$, is weaker in larger particles. As S_0 increases, the combination of these two opposing effects; that is, the reduced fluctuation amplitude ΔK, versus the enhanced magnetic tunneling transition probability at the switching field (due to closer proximity to the SW switching field) explains the weak size dependence of the nonequilibrium noise temperature at the switching field. Alternative models in Ref. [102] predict that the probability of magnetic tunneling transitions is given by the square of the Clebsch-Gordan (GC) coefficient which is on

the order of $1/S_0$. That model would lead to two orders of magnitude suppression in T_M for larger Co particles, which disagrees with our experimental observations. On the other hand, our model provides good agreement with the observed T_M in larger particles.

5.2 Experiment

5.2.1 Sample Fabrication

Our samples are made using electron beam lithography (EBL) and shadow deposition. [104] Figure 5.1A shows the fabrication process of our sample. First, a polymethilmetachryllate (PMMA) bridge is defined by EBL over a SiO_2 substrate. Second, 10nm of Al and 1.5-3nm of Al_2O_3 is deposited along direction 1. Then the sample is oxidized at room temperature in O_2 at 3mPa, for 30s. Next, we deposit 0.5nm of Co, 1nm-1.5nm of Al_2O_3, followed by 10nm of Al, along direction 2. Sample resistance can be varied by changing the oxide layer thickness. After lift-off in acetone, the samples are ready to be wired up for measurement. Co forms isolated particles of diameter 1-4nm on aluminum oxide substrate with nominal thickness of 0.5nm, which has already been confirmed by prior work done by D. Ralph's group, and D. Davidovic's group.[31, 44] The exact same recipe as in those works is used for the growth of Co particles measured in this work. Furthermore, the Coulomb blockade in the IV-curve (Fig. 1B) as well as the single discontinuity shown in the current hysteresis (Figure 5.1C) all signify the tunneling through single Co particles.

5.2.2 Transport Measurement

Figure 5.1B displays the IV-curve of sample 1 at 90mK. As before, the IV-curve is interpreted here in terms of the Coulomb blockade at low bias voltage and sequential electron tunneling at large bias voltage, for a single particle. [44] The Coulomb blockade is indicated by the low voltage region where the current is very small. At voltages above the Coulomb blockade thresholds, no discrete steps in the I-V curve

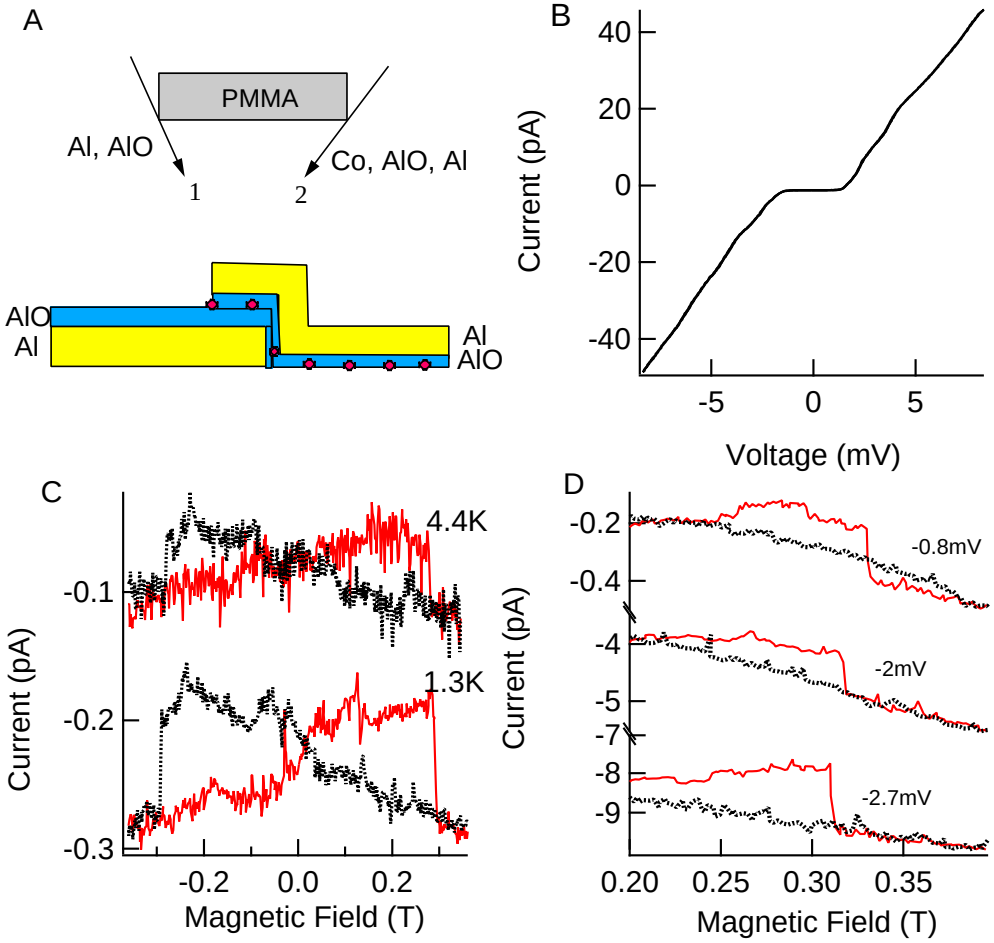

Figure 5.1: A: Sketch of the sample fabrication process. Red dots represent Co particles. B: Current versus bias voltage for Sample 1 at 90mK. C: Hysteresis loops in current versus applied magnetic field at -0.1mV, in sample 1 at 1.3K and 4.4K. The current loop at 1.3K is offset by -0.15pA for clarity. D: Magnetic switching field for sample 1 at three different bias voltages/currents and 90mK. Red (black) lines in C and D correspond to increasing (decreasing) magnetic field.

are seen in Figure 5.1B, showing that discrete levels are not resolved in that case. The absence of discrete levels indicates that the particle size is large enough so that the level spacing is much smaller than the energy resolution at 90mK. The sample leads are cryogenically filtered in order to reduce the electronic temperature to < 100mK. One way to confirm that only one particle contributes to tunneling is from the magnetic hysteresis loop. If only one switching field were measured, then only one particle would contribute significantly to the current, because multiple particles would likely have different switching fields.

Figure 5.1C shows the typical current hysteresis loops for sample 1 at 1.3K and 4.4K. The current is measured at a fixed bias voltage while sweeping the magnetic field. The current exhibits hysteretic shifts with magnetic field, which could be attributed to the field dependence of the energy levels, broadened by the Fermi distribution in the leads. The dependence of energy levels on the magnetic field in Co particles has been studied in Refs. [31, 19, 44]. The discontinuity in current during the magnetic field sweep, along with hysteresis, indicates magnetization reversal in the Co particle. As the sample temperature is increased, the hysteresis loops narrow (Figure 5.1C). Note that the switching field is very weakly reduced with temperature between 1.3K and 4.2K, compared to that in our prior study of Co particle with smaller diameter, [44] wherein a Co particle with $S_0 \approx 728$, the switching field dropped by 26% as the temperature increased from 1.4K to 4.2K. In comparison, the switching field of sample 1 in this paper drops by 4.3% in the same temperature range. The weak temperature dependence in sample 1 indicates again that the particle size is much larger than in the previous work. The energy barrier for magnetic switching in the particle scales with S_0 and B as $S_0(1 - B/B_0)^{3/2}$, where B and B_0 are the applied magnetic field and the SW switching field, respectively, assuming that B is close to B_0. Magnetic switching occurs roughly when the barrier divided by the thermal energy k_BT is equal to $ln(\nu_0/\nu)$, where ν_0 is the attempt frequency and ν is

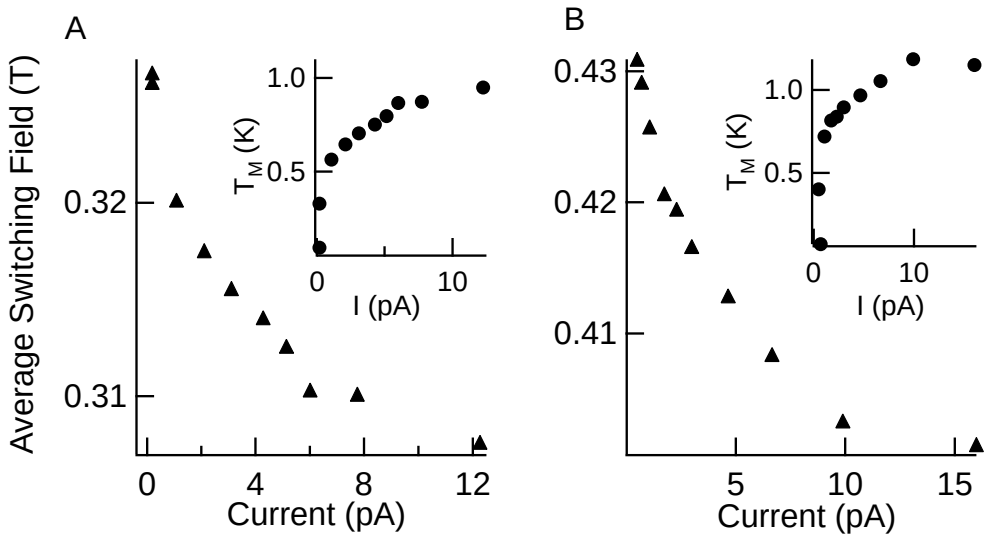

Figure 5.2: A and B: Average switching field versus tunneling current for sample 1 and 2, respectively. Each data point is averaged over approximately 40 hysteresis loops. Insets: Magnetic temperature at the switching field, versus tunneling current.

the sampling rate. The reduction from 26% to 4.3% then corresponds to an increase in S_0 by factor of 15, leading to $S_0 \approx 10824$ for sample 1, assuming the same value for $ln(\nu_0/\nu)$ in both samples. Since the dependence on the attempt frequency is logarithmic, the assumption is reasonable. We will return to the estimate of S_0 further below.

We now study the current dependence of the hysteresis loops for two samples at 90mK. The magnetic field sweep rate is 7.1mT/s in all the measurements of current hysteresis loops, while the dilution refrigerator temperature is maintained at 90mK during the sweeps. The value of the switching field and tunneling current was recorded immediately prior to the magnetization switch. Typical current hysteresis loops for sample 1 at three different bias voltage/current are displayed in Figure 5.1D. The whole hysteresis loops are shown in Figure 5.3. Similar results can be obtained for the magnetic switch in the opposite field direction.

Note that there are current peaks near zero field in the hysteresis loops, which are artifacts due to the heat spike generated by the superconducting magnet when

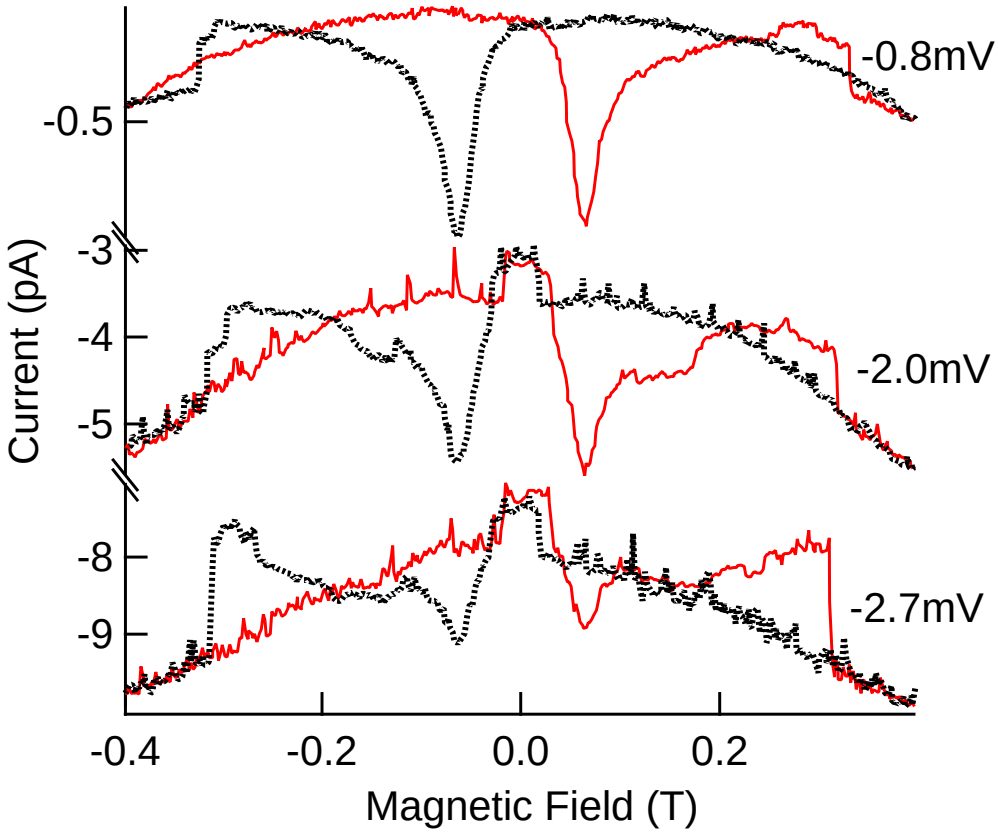

Figure 5.3: Typical hysteresis loop at different bias voltage for sample 1. Red (black) lines correspond to increasing (decreasing) magnetic field.

it passes across zero field. According to the vendor of our superconducting magnet (Oxford Instruments), that heat spike is due to the Eddy current caused by the depinning of the flux vortices in the superconducting magnet when it sweeps across zero field and it is a fairly well known problem. We have seen similar phenomena in our experiments ever since we have this magnet. In our electron tunneling measurements, the tunneling current through the particle is sensitive to that heat spike only at mK temperatures, because the heat capacity of the sample is very low at mK and the IV curve of the sample is very sensitive to temperature. At higher temperatures (> 1K), the heat spike is not visible from the measurement of the tunneling current in our samples. We found that this problem can be avoided by sweeping the magnet extremely slowly. However, we have to sweep the magnet faster to acquire enough hysteresis loops for our data to be statistically reliable. On the other hand, the current peak shown in the hysteresis loops is an evidence that our sample is indeed at mK temperatures. The fact that the current went back after the peak before the magnetic switch indicates that the heat has been fully dissipated before the magnetic switch, so our data of the magnetic switching field is not affected by that heat spike.

At -0.8mV, the sample is just below Coulomb Blockade. Clearly, the magnetic switching field decreases with higher current magnitude. The switching field at current I and $T = 90$mK will be labeled as $B_{sw}(I)$. Figures 5.2A and B display $B_{sw}(I)$ for sample 1 and 2, respectively. The switching field is reduced by 6.4% in sample 1 at 15pA, and 5.8% in sample 2 at 12pA, relative to the switching fields at the lowest current. In comparison, in the previous work on the Co particle with $S_0 \approx 728$, $B_{sw}(6\text{pA})$ was reduced by 15% compared to that at zero current. Thus, both temperature and tunneling current have a reduced effect on the switching field in larger Co particles.

We also measure the hysteresis loops at different temperatures to obtain the temperature dependence of the equilibrium switching field. During those measurements

at different temperatures, the bias voltage is set at the lowest level where the hysteresis loops just emerge, so the switching field could be viewed as equilibrium switching field, i.e., the switching field at zero current. Thermal fluctuations can also reduce the magnetic switching field and the temperature dependence of the relative reduction of the switching field $(1-B_{eq}(T)/B_0)$ can be fitted to the Néel-Brown model. [65, 12, 106] Here, $B_{eq}(T)$ is the equilibrium switching field at temperature T. By fitting the temperature dependence of the switching field, according to the procedure explained in our previous work, [44] we estimate that the total spin of the Co particle is $S_0 \approx 11394$ in sample 1, in agreement with the estimate obtained earlier, and $S_0 \approx 4691$ in sample 2. Assuming the particles are hemispherical, the corresponding diameters of the particles are 6.5nm and 4.8nm for sample 1 and 2, respectively. Since both thermal fluctuations and tunneling current can lead to decrease in the magnetic switching field of single Co particles, magnetic temperature $T_M(I)$ of the Co particle at current I can thus be defined as $B_{eq}(T_M(I)) = B_{sw}(I)$. Magnetic temperature $T_M(I)$ can be calculated by linearly interpolating $B_{sw}(I)$ to $B_{eq}(T)$. For example, the reduction by 6.4% at 15pA in sample 2 corresponds to $T = 1.15$K in $(1 - B_{eq}(T)/B_0)$. Thus, the magnetic temperature $T_M(15\text{pA})$ is 1.15K for sample 2. $T_M(I)$ could serve as an indicator of the strength of the nonequilibrium magnetization noise, while the average magnetic excitation energy E_M at steady state is indicated by $E_M = k_B T_M$. [44] The insets in Figures 5.2A and B shows the magnetic temperature versus tunneling current in sample 1 and 2, respectively.

Note that $T_M(I)$ introduced above refers only to the magnetic temperature at the switching field. We expect a strong dependence of magnetic temperature with the applied magnetic field, as will be discussed below. In samples 1 and 2, $T_M(6\text{pA}) =$ 0.87K and 1.04K, at bias voltages 2.4mV and 3.2mV, respectively. In comparison, in the much smaller sample from previous work, [44] $T_M(6\text{pA}) = 2.5$K at 10mV bias. Alternatively, in samples 1 and 2, $T_M(1.3\text{pA}) = 0.56$K and 0.75K, at bias

voltages 1.84mV and 1.9mV, respectively, while for the sample from the prior work, $T_M(1.3\text{pA}) = 1.3\text{K}$ at 4mV bias. As S_0 increases by factor of 16, $T_M(I)$ is reduced by factor of 2.3 (2.9) at 1.3pA (6pA). Thus, the size dependence of magnetic temperature is weak compared to that of S_0.

The current driven reduction in switching field studied in Ref. [44], demonstrated that that this effect was not due to ordinary Joule heating, because the width of the Fermi distribution in the leads was very small compared to $k_B T_M(I)$. In this paper, the size of the particle is much larger than in Ref. [44]. Thermal conductance between the particle and the environment scales in proportion with the particle surface area. In addition, the power input IV is smaller here by factor of 2-3. Since Joule heating was insignificant in the smaller particle, we conclude that Joule heating is even lower than before, so $T_M(I)$ should remain much larger than the environment temperature. In that case $k_B T_M(I)$ represents the average out of equilibrium magnetic excitation energy of the particle in the steady state, just before the switching field. The necessary condition to be out of equilibrium is that the magnetic excitation rate by tunneling be larger than the magnetization relaxation rate T_1^{-1}.

5.3 Discussion

5.3.1 Model

As shown in Ref. [44], the nonequilibrium magnetization noise originates from the tunneling transitions involving different magnetic states, or simply, magnetic tunneling transitions. Magnetic tunneling transitions have been described by the master equation in Ref. [102]. In that work, the tunneling matrix elements are given by Clebsch Gordan (CG) coefficients, which are negligibly small for the first several magnetic states if $S_0 \gg 1$. On the other hand, SO interaction resulting in magnetic anisotropy fluctuations can greatly enhance the tunneling matrix elements in the vicinity of the

magnetic switching field, while the probabilities of magnetic tunneling transitions remains very low at strong magnetic field. [44] In the remainder of this paper, we will combine the master equation with the magnetic anisotropy fluctuations to explain the properties of nonequilibrium magnetization noise including its size dependence.

We assume that the total spin S_0 stays constant when the magnetic field is varying. Then, we can adopt the magnetic model-Hamiltonian introduced in Ref. [19],

$$\mathcal{H}(\vec{B}, N) = -g\mu_B \vec{B} \cdot \hat{\vec{S}} - K_N \hat{S_z}^2 / S_0. \tag{5.1}$$

Here $\vec{S}$ is the total spin with ground state magnitude S_0 for N electrons. Z axis is parallel with the easy-axis of the particle which is independent of N. Because of the magnetic anisotropy fluctuations, the uniaxial anisotropy constant K_N now depends on the total electron number N. As discussed in the introduction, it has been shown that the standard deviation in K_N in Co particles is $\approx 10K/S_0$, where K is the average of K_N. [98] Thus, in our particles the difference between K and K_N is on the order of 0.1-1%. Generally, the magnetic field and the easy-axis of the particle are not collinear. Therefore, the eigenstates $|S_0, m>$ of $\hat{\vec{S}}^2$ and $\hat{S}_Z$ are no longer the eigenstates of $\mathcal{H}$. Instead, the eigenstates of $\mathcal{H}(\vec{B}, N)$ (magnetic eigenstates) can be represented by the linear superpositions of $|S_0, m>$ [9]. In the following analysis of this work, we use $S_0 = 1000$ and 45° for the angle between magnetic field and easy axis, which are in agreement with prior experimental reports. [31, 19, 44] Now we assume that only one single electron state j is involved in the electron tunneling process, for simplicity. Increasing the number of levels into the analysis does not alter the qualitative picture, if the fluctuations in anisotropy are ignored. [102] In the sequential tunneling regime, an electron tunnels though j making the particle hop between N and $N+1$ electron states. Thus, the master equation in Ref. [102] can be

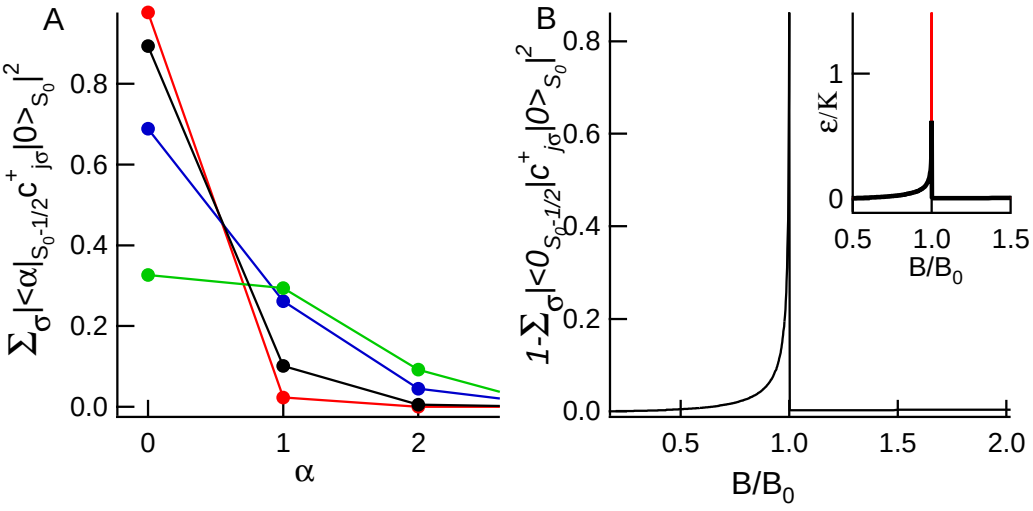

Figure 5.4: A: Probability of transitions from the ground state $|0>_{S_0}$ to the ground state and excited states $|\alpha>_{S_0-1/2}$, by an addition of an electron to the minority level j. $\alpha = 0, 1$, and 2 represent the magnetic ground state, first, and second magnetic excited state with spin $S_0 - 1/2$, respectively. Viewed from the left most data points, B/B_0= 0.78(Red), 0.95(Black), 0.99(Blue), and 0.999(Green) from top to bottom. B: Probability of a magnetic tunneling transition versus magnetic field. Inset: Increment in magnetic excitation energy upon an addition of an electron to the minority level j, versus magnetic field. Black line is the classical energy ϵ_C, while the red line is obtained from the master equation. $S_0 = 1000$ and $\Delta K_N/K = 1.1\%$ in A and B

reduced to

$$\frac{\partial P_\alpha}{\partial t} = \sum_{\alpha'} \sum_{l=L,R} \sum_{\sigma=\uparrow,\downarrow} \Gamma_{l\sigma} \Big\{ |<\alpha'|c_{j\sigma}|\alpha>|^2 \left[-(1-f_l(E_\alpha - E_{\alpha'}))P_\alpha + f_l(E_\alpha - E_{\alpha'})P_{\alpha'}\right] + |<\alpha'|c^\dagger_{j\sigma}|\alpha>|^2 \left[-f_l(E_{\alpha'} - E_\alpha)P_\alpha + (1-f_l(E_{\alpha'} - E_\alpha))P_{\alpha'}\right] \Big\}. \tag{5.2}$$

Here, $|\alpha>$ and $|\alpha'>$ represent magnetic eigenstates of the particle with N or $N+1$ electrons. $c_{j\sigma}$ ($c^\dagger_{j\sigma}$) is the annihilation (creation) operator for an electron with spin σ on level j. $\Gamma_{l\sigma}$ denotes the tunneling rate to level j through the leads $l = L, R$ for electron with spin σ and f_l is the Fermi distribution in the leads. $|<\alpha'|c^\dagger_{j\sigma}|\alpha>|$ is the tunneling transition element for transition between the initial state $|\alpha>$ and the final state $|\alpha'>$.

Next, we discuss the electron-tunneling-on event where the particle changes from

N to $N+1$-electron state. We assume that the particle is initially in the ground state with N electrons $|0>_{S_0}^{N}$. Then, according to prior studies, [19, 14, 102] we make a further assumption that j is a minority state which reduces the spin of the particle by 1/2 after the electron-tunneling-on event. Thus, the overlap between magnetic ground state before tunneling and the magnetic states after tunneling is $|<\alpha_{S_0-1/2}^{N+1}|c_{j\sigma}^{\dagger}|0>_{S_0}^{N}|^2$, while the probability of any magnetic tunneling transition becomes $1-\sum_{\sigma}|<0_{S_0-1/2}^{N+1}|c_{j\sigma}^{\dagger}|0>_{S_0}^{N}|^2$. Figure 5.4A shows the overlap between $|0>_{S_0}^{N}$ and $|\alpha>_{S_0-1/2}^{N+1}$ at several magnetic fields. As B moves closer to the SW switching field B_0, the overlap between $|0>_{S_0}^{N}$ and the magnetic ground state ($\alpha=0$) for $S_0-1/2$ becomes weaker while the overlaps between $|0>_{S_0}^{N}$ and the magnetic excited states ($\alpha>0$) are stronger. When ΔK becomes comparable to, or larger than, the spacing between magnetic states, the magnetic ground state of the N electron system overlaps with a large number of magnetic excited states for the $N+1$ electron system. In comparison, if the SO interaction were not fluctuating, meaning $K_N = K_{N+1}$, the probability of magnetic tunneling transitions would be close to $1/2S_0$. However, if we take into account the magnetic anisotropy fluctuations, the probability of the magnetic tunneling transitions is significantly enhanced in the vicinity of B_0 before the magnetic switch, as shown in Figure 5.4B. Here, $\Delta K_N = K_{N+1} - K_N$ is chosen to be $1.1\%K_N$ based on the theoretical work. [98] The increment ϵ in the magnetic energy excited by the electron-tunneling-on event, $\epsilon = \sum_{\alpha',\sigma}(E_{\alpha'}^{N+1,S_0-1/2} - E_0^{N+1,S_0-1/2})|<\alpha_{S_0-1/2}'^{N+1}|c_{j\sigma}^{\dagger}|0>_{S_0}^{N}|^2$, where $E_{\alpha'}^{N+1,S_0-1/2}$ represents the eigenenergy of the magnetic state $|\alpha'>_{S_0-1/2}^{N+1}$ and $E_0^{N+1,S_0-1/2}$ is the ground state energy of $\mathcal{H}(\vec{B}, N+1)$. As a result of enhanced magnetic tunneling transition probability, ϵ is also greatly boosted by the magnetic anisotropy fluctuations as the magnetic field approaches B_0, approaching a value comparable to K (Figure 5.4B Inset). Since $S_0 \gg 0$, ϵ could also be obtained from the classical SW-model, as sketched in Figure 5.5A. [44] The result obtained from classical method agrees with the result from the master equation,

except in the close vicinity of the SW switching field, as shown in the inset of Figure 5.4B. The discrepancy arises when the magnetic level spacing becomes comparable to (or smaller than) ΔK.

5.3.2 Numerical Simulation

Now, we simulate the time evolution of the magnetic excitation energy in the Co particle using Eq. 5.2. The magnetic excitation energy at time t can be written as $E_M(t) = \sum_i \sum_\alpha P_\alpha^i(t)(E_\alpha^i - E_0^i)$, where $i = N, N+1$ represents the number of electrons in the particle, E_0^i is the ground state energy for i-electron state and $|\alpha>$ denotes any magnetic eigenstate for N or $N+1$-electron state. The result of the numerical simulation is presented in Figure 5.5B. A linear fitting of $E_M(t)$ shows that $E_M(t) \approx 2\epsilon\delta f t$, where $\delta f = \Gamma_L\Gamma_R/(\Gamma_L + \Gamma_R) = I/e$. The magnetization excitation energy increases linearly versus time, meaning that ϵ for single electron-tunneling-on or tunneling-off event is independent of $E_M(t)$. Note here that no external magnetization relaxation mechanism is included in Eq. 5.2. If we now consider the magnetization relaxation, E_M would vary versus time based on the differential equation $\mathrm{d}E_M/\mathrm{d}t = 2\epsilon\delta f - E_M/T_1$, where T_1 is the magnetization relaxation time for the Co particle. Then, the average of $E_M(t)$ would reach the steady value $2\epsilon\delta f T_1$ if t is large enough, and the average steady value of $E_M(t)$ could be represented by the magnetic temperature $k_B T_M$. In the prior work, we have obtained the time evolution of the magnetic excitation energy from the stochastic Landau-Lifshitz-Gilbert equation. [44] That approach confirmed the steady state average magnetic energy of $2\epsilon_C\delta f T_1$.

According to Ref. [98], $\Delta K_N/K \approx 10/S_0$ in the Co particle. We now increase S_0 from 1000 to 3000, then $\Delta K_N/K$ is expected to be reduced by factor of three. The particles in this paper are much closer to the SW-switching field before the reversal of its magnetization, compared to the smaller Co particle studied previously, because the temperature dependence of the switching field is much weaker in larger particles.

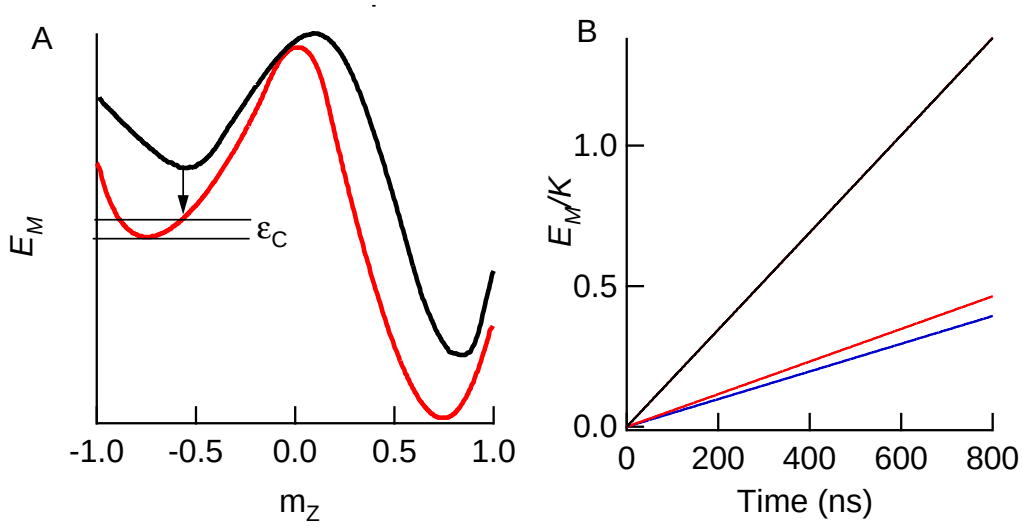

Figure 5.5: A: Sketch of the classical magnetic excitation energy induced by electron tunneling and magnetic anisotropy fluctuations. B: Magnetic excitation energy versus time simulated numerically using Eq. 5.2. Black line corresponds to both $S_0 = 1000, \Delta K_N/K = 1.1\%, B = 0.78B_0$ and $S_0 = 3000, \Delta K_N/K = 0.365\%, B = 0.94B_0$. Red line: $S_0 = 3000, \Delta K_N/K = 0.365\%, B = 0.78B_0$. $\Gamma_{L,R} = 6 \times 10^7 \mathrm{s}^{-1}$ for both black and red. Blue line: $S_0 = 1000, \Delta K_N/K = 1.1\%, B = 0.78B_0$ and $\Gamma_{L,R} = 1.71 \times 10^7 \mathrm{s}^{-1}$.

Meanwhile, the probability of magnetic tunneling transitions as well as ϵ can be greatly enhanced as the magnetic field gets closer to the SW switching field (Figures 5.4A and B). Therefore, the magnetic temperature exhibits weaker size dependence even though the magnetic anisotropy fluctuations are reduced proportionally to S_0^{-1} in larger particles. For example, for $S_0 = 1000, \Delta K/K = 1.1\%$ and $B = 0.78B_0$, the probability of magnetic tunneling transition is 0.023 and $\epsilon = 0.0286K$. If $S_0 = 3000$, $\Delta K/K = 0.365\%$ and $B = 0.94B_0$, the probability of magnetic tunneling transition becomes 0.0111 and $\epsilon = 0.0285K$ which is very close to the value at $S_0 = 1000$. For those two parameter choices, the magnetic energy E_M increases versus time nearly identically, as shown in Figure 5.5B. The reduction of the fluctuation amplitude ΔK_N is compensated by the closer proximity of B to the SW field.

The weak size dependence confirms the main conclusion from Ref. [44], that the magnetic tunneling transitions are governed by magnetic anisotropy fluctuations,

rather than by the matrix-elements of the tunnel Hamiltonian equal to the CG-coefficients. Assume now that the square of the CG-coefficients determine the probability ratio between the magnetic tunneling transitions and the nonmagnetic tunneling transitions. In that case, the probability that the particle is excited magnetically, after an electron tunneling event, is $1/2S_0$. [102] The magnetic temperature becomes $k_B T_M(I) \approx \omega I T_1/S_0 e$, where ω is the magnetic level spacing at the switching field. As already discussed in our prior work, [44] this $T_M(I)$ would be in agreement with measurement, if the magnetization relaxation time were $T_1 \sim 10^{-3} - 10^{-2}$s. However, this differs by six orders of magnitude from the accepted relaxation time in ferromagnets of $\sim 0.1 - 1$ns [36]. Although there are few suggestions that T_1 in Co particles may be longer than in the bulk, [19, 109, 43], T_1 in single Co particles has not been measured yet. Despite the low odds that $T_1 \sim 10^{-3} - 10^{-2}$s, we now estimate the size dependence of $T_M(I)$ if CG-coefficients were responsible for the magnetic tunneling transitions. ω decreases rapidly as the magnetic field approaches B_0; its minimum value would reach K/S_0. That leads to the size dependence of $T_M(I) \sim \omega T_1 S_0^{-1} \sim S_0^{-2}$. In sample 1, T_M should be reduced by two orders of magnitude compared to that in the small particle in Ref. [44], if T_1 were comparable. However, such a reduction disagrees with our measurement of the size dependence of $T_M(I)$ by two orders of magnitude. In comparison, our model utilizing mesoscopic anisotropy fluctuations provides a mechanism for driving magnetic tunneling transition that is natural, and in both quantitative and qualitative agreement with the measured magnetic temperature size dependence.

CHAPTER 6

ELECTRON TRANSPORT MEASUREMENTS OF NI, FE, AND $NI_{80}FE_{20}$ PARTICLES

6.1 Introduction

As ferromagnets become smaller in size, the decreasing magnetic energy barrier and the corresponding blocking temperature, as well as the changing magnetic anisotropy, play the critical roles in maintaining the magnetization direction.[65, 12, 106] In addition to thermal noise, electron transport through very small ferromagnets can also inhibit magnetic hysteresis, which may pose a fundamental limit for the miniaturization of spin-based electronics. As an example, while hysteresis in magnetic molecules was confirmed by magnetometery,[24, 92, 107, 59] electron transport measurements via single molecules do not exhibit magnetic hysteresis,[35, 29, 13, 113] even at temperatures far below the blocking temperature.[46] We have recently shown that the effect of electron transport persists in larger magnetic systems. The magnetic hysteresis loops of Co particles of diameter ≈2nm display narrowing at the onset of sequential electron transport, while the ordinary Joule heating is negligibly weak.[44] However, the electron tunneling measurements of single ferromagnetic particles have been limited to Co. Thus, we perform the first systematic study of similarly-sized single Ni, Ni−61 Py=$Ni_{0.8}Fe_{0.2}$, Fe, and Co particles, embedded in double-barrier tunneling devices. Using the single electron tunneling technique, we find a remarkable difference in the abundance of magnetic hysteresis among different particle materials. It is in stark contrast to Co particles which always show hysteresis during electron tunneling measurement. Further research is required to completely understand the results we have.

6.2 Experiment

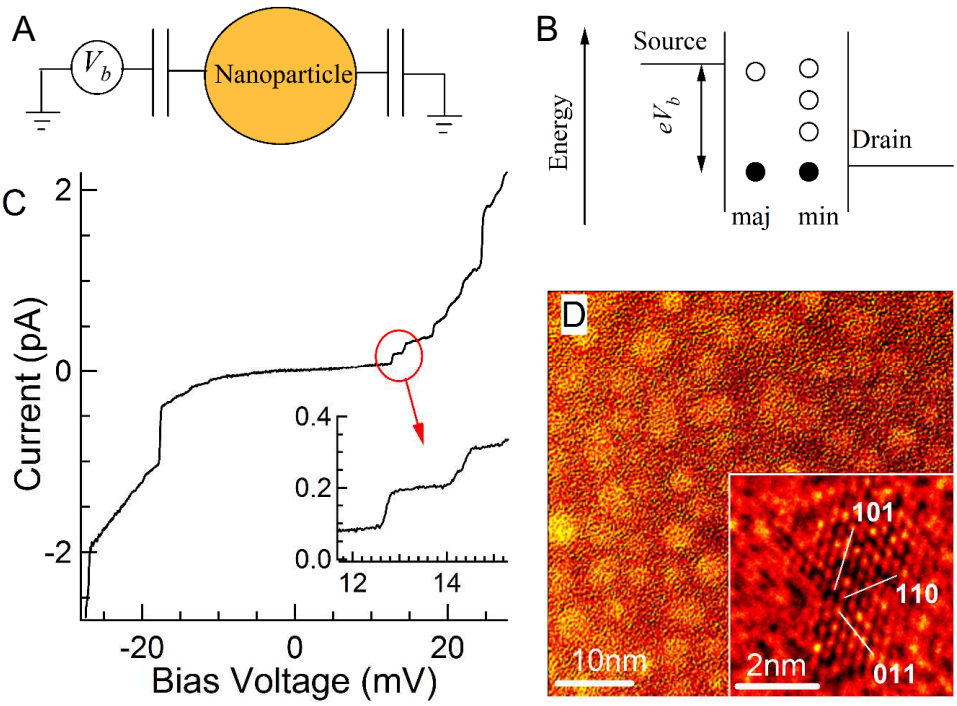

Figure 6.1: A: Circuit diagram of electron tunneling through particles. Red dots represent magnetic particle. B: Energy level diagram for tunneling process. "min" and "maj" indicate the minority and majority states, respectively. C. Discrete levels in the IV curve in a Ni particle sample at $B = 8$T and $T = 30$mK. D: Image of Ni particles on aluminum oxide surface. Inset: Single crystal structure for one particle.

As shown in Figure 6.1A, the ferromagnetic particles are capacitively coupled to two Al leads with a bias voltage applied across the particle. Figure 6.1B displays the energy levels of the particle between the junctions. A bias voltage V_b changes the Fermi level in the source lead by eV_b. When the Fermi level equals the energy difference between the final and initial quantum states of the particle, the tunneling transition between those states can take place. At that voltage, discrete step in the IV curve is displayed, as shown in Figure 6.1C for Ni sample 1.

The sample fabrication process has been described in our earlier published work.[44] The irregularly shaped Ni particles are created by the evaporative deposition of Ni

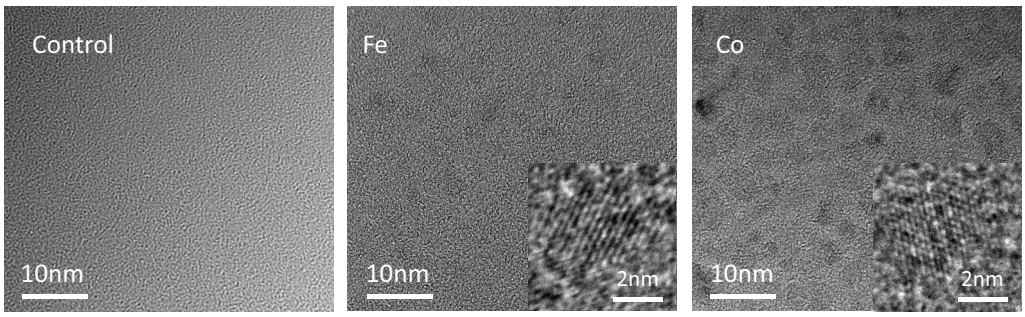

Figure 6.2: TEM image of aluminum oxide surface topped with nothing, 1.2nm of Fe, and 0.6nm of Co.

at 5-6Å nominal thickness on aluminum-oxide surface. The particles are shown by the transmission electron microscope (TEM) image in Figure 6.1D, with the inset showing the single crystal structure of a particle. The lattice constant extracted from the structure confirms faced-centered-cubic Ni. In addition, energy dispersive X-ray spectra (EDS) demonstrate that the particles are made from Ni. The volume of the Ni particles in Figure 6.1D is estimated to be $V = 15 \pm 6\text{nm}^3$, with the error reflecting the particle-size distribution. The analysis is done in 120 Ni neighboring particles.

We also obtain the TEM image of the deposited pure aluminum oxide surface, and the aluminum oxide surface topped with nominally 1.2nm of Fe, and 0.6nm of Co, as shown in Figure 6.2. The deposition is done immediately prior to loading the sample in the TEM. Pure aluminum oxide surface appears completely amorphous, with no visible signs of crystalline structure. In comparison, single crystal structure can be identified in the TEM images for Fe, and Co. The volume distribution in Co particles is similar to that in Ni.

In Figure 6.3A, the IV curve displays coulomb blockade (CB) which indicates electron tunneling through Ni particles, but no discrete levels are resolved at 4.2K. The current versus applied magnetic field (parallel to the film plane) is obtained by measuring the current at a fixed bias voltage while sweeping the magnetic field slowly (Figure 6.3B). Though the Ni sample displays magneto-resistance (MR), no

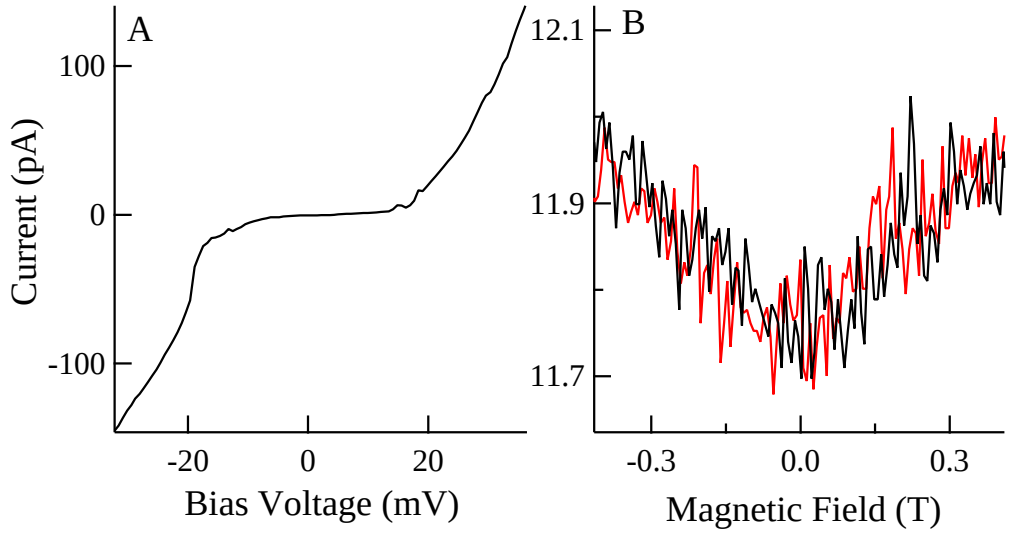

Figure 6.3: A: IV curve of a typical natural Ni at 4.2K. B: Current versus magnetic field at 4.2K for samples in A. Red(black) lines correspond to decreasing(increasing) magnetic field.

hysteresis can be identified in Figure 6.3B. Since the electrodes are made of Al which is nonmagnetic, the MR of the sample indicates that the Ni particle being measured is magnetic. However, at 4.2K and below, only 2 of the 46 measured natural Ni samples display hysteresis. On the other hand, all of the Co samples (over 50) show magnetic hysteresis.

We studied 8 Ni samples at mK-temperatures. Figures 6.4A and B display the magnetic field dependence of the tunneling spectrum of Ni sample 1 at 30mK. Discrete levels correspond to the maxima in conductance, they are symmetric about zero magnetic field, and no hysteresis is detected. In a strong magnetic field, the width of the lowest level corresponds to the leads' electron temperature of 0.23K, which is much smaller than the expected blocking temperature. Thus, the suppression of magnetic hysteresis in our samples is not due to ordinary Joule heating. The energy levels in Figure 6.4 exhibit both zero field splitting (ZFS) and Zeeman splitting at strong magnetic field. Note that the ZFS is much larger than the anisotropy energy corresponding to the switching field in Co and Py particles ($\sim 10 - 20\mu eV$). The

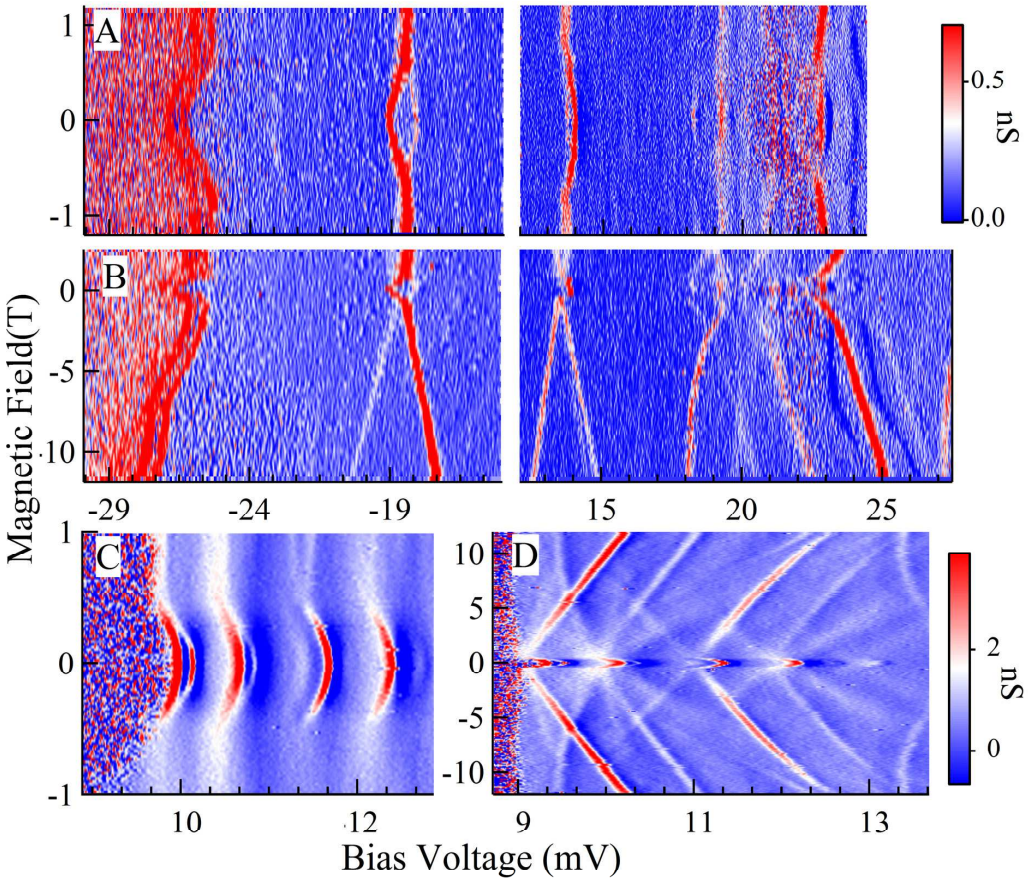

Figure 6.4: Differential conductance versus magnetic field and voltage at 30 mK. A and B: Ni sample 1. C and D: Ni sample 2.

energy of a tunneling transition includes the difference in magnetic energy ΔE_M after and before tunneling, so the envelope of ΔE_M for different magnetization direction will be added to the electron-in-a-box level according to the orientation distribution of the magnetization, which leads to ZFS in Ni samples. After conversion from voltage to energy, the ZFS at negative bias $\approx$0.5meV, which is comparable to the single-electron anisotropy measured from the discontinuous shifts of the energy levels at the switching field of Co particles.[31] In Figure 6.4A, the ZFS is not symmetric with bias voltage, which shows that the range of ΔE_M has different weight distribution at different current directions, which could be related to the asymmetry in tunnel junction resistance.

In a strong magnetic field, the lowest level splits in energy versus field by $g\mu_B B$, where μ_B is the Bohr magneton and $g = 1.75$ (Figure 6.4B). At positive bias voltage, the spin increasing and decreasing transitions of the first level have approximately equal weight (Figure 6.4B). This remarkable result is very different from the tunneling spectra of Co particles, where the levels do not display Zeeman splitting.[19, 31, 44] The tunneling spectra of normal metal particles have similar Zeeman splitting as in our Ni particles.[76, 17] But, the Zeeman split levels in normal metal particles cross at zero applied magnetic field, while the crossings in Figure 6.4A are offset by approximately $\pm$0.5T. The ZFS and Zeeman splitting have been confirmed in a second sample as shown in Figures 6.4C and D.

To further understand our result, we perform electron tunneling measurements on similar sized Fe and Py particles (Figure 6.5). The probability that the particle will exhibit hysteresis increases in the order of Ni, Py, Co/Fe where Co and Fe particles always show hysteresis.

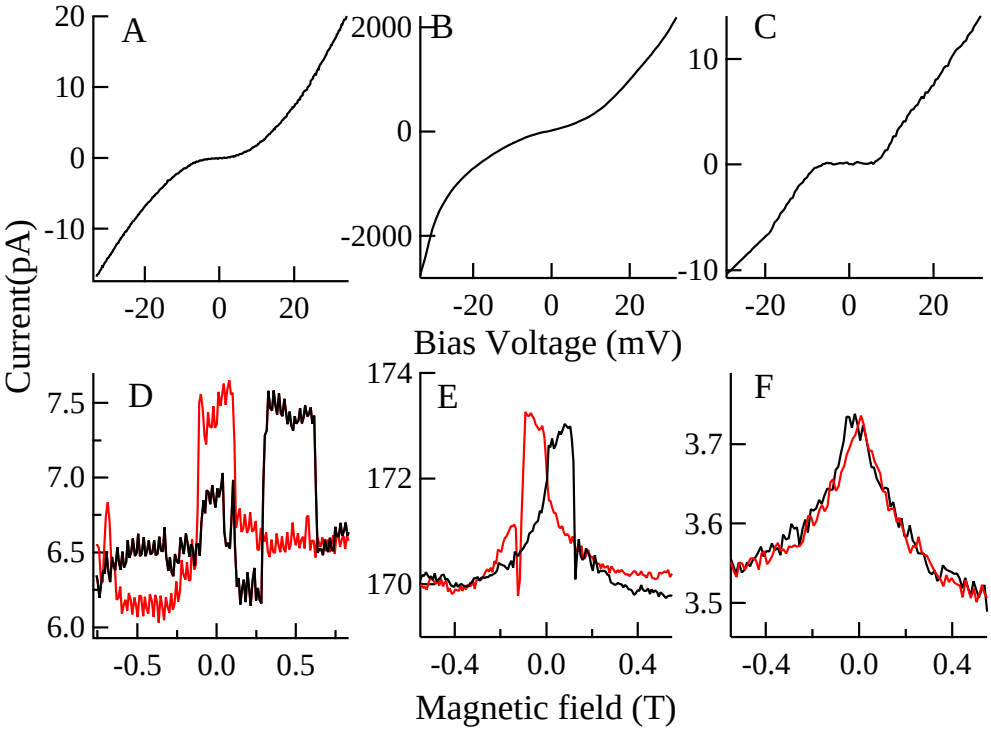

Figure 6.5: A, B, and C: IV curve of a typical Fe, Py and Ni-61 isotope sample at 4.2K, respectively. D, E, and F: Current versus magnetic field at 4.2K for samples in A, B, and C, respectively. Red(black) lines correspond to decreasing(increasing) magnetic field.

6.3 Discussion

To address the difference in the hysteretic behaviors between those ferromagnetic particles, we can start from superparamagnetism. In thermal equilibrium, the Néel magnetization flipping time is $\tau_N = \tau_0 \exp(E_B/k_B T)$, where τ_0 is the attempt time, k_B is the Boltzmann constant and T is the temperature.[65] E_B is on the order of the magnetic anisotropy energy of the particle KS, where S is the total particle spin in units of $\hbar$. The temperature at which the measurement time equals τ_N is the blocking temperature T_B, leading to the well known expression $T_B \approx E_B/20k_B$. Above the blocking temperature, the hysteresis is suppressed. In thermal equilibrium, $k_B T$ equals the average magnetic energy E_M of the particle. However, nonequilibrium magnetization noise can be brought into the particle by the external source such as electron transport.[44, 45] Thus, E_M can be much larger than $k_B T$.[44, 45] In that case, hysteresis will be inhibited if $E_M > k_B T_B$, even when $T \ll T_B$. Thus, we conclude that the average magnetic energy E_M in Ni particles is so high that the Ni particle's magnetization goes into a superparamagnetic-like state where the magnetization flips at a speed much higher than our measurement rate. Therefore, no hysteresis can be detected. Since the energy of a tunneling transition includes the difference in magnetic energy ΔE_M after and before tunneling, the envelope of ΔE_M for different magnetization direction will be added to the energy level according to the orientation distribution of the magnetization, which leads to ZFS in Ni samples. The Zeeman split levels crossing at ± 0.5T shows that the Ni particle we measure is ferromagnetic, but the magnetization of the Ni particle remains isotropic, so that the spin increasing and decreasing tunneling transitions have equal probability.

Prior magnetometry on similarly-sized particles show that the blocking temperature varies between $13 - 30$K for Co and $9 - 20$K for Ni.[82, 57, 111, 22] Though Co particles appear to have higher blocking temperature than Ni particles, the difference in blocking temperature is not sufficient to explain the vast contrast in the hysteresis

abundance in single particles under electron transport. Measurements of the blocking temperature usually involve arrays of particles, so the comparison with the single particles is problematic because of the ensemble averaging. Thus, the height of the energy barrier and the magnetization noise from the environment both have their importance in explaining the different hysteretic behaviors of different particles.

6.3.1 Energy Barrier

We first look into the energy barrier of different particles, which is determined by the magnetic anisotropy and size of the particle. The particles with different materials are fabricated using a similar method, thus they are expected to have similar size distribution. So we will focus on the magnetic anisotropy.

For magnetocrystalline anisotropy, it is known theoretically that the calculations of it are very complicated and the results are not in good agreement with experiment even in the bulk.[87, 15] Due to the large surface/volume ratio and irregular shape, it is inappropriate to use bulk magnetocrystalline anisotropy to evaluate the SO-contribution to the anisotropy in a metallic ferromagnetic particle. In a hemispherical fcc-Co particle with a symmetry axis, theoretical simulations of the effect of spin-orbit interaction find easy-plane anisotropy perpendicular to the symmetry axis, with a suppressed anisotropy within the easy plane.[15] In irregularly shaped particles with no symmetry, the role of the SO interaction is less clear. It has been argued that in Co particles with 2-5nm in diameter, both mesoscopic and magnetocrystalline anisotropy play a role in defining the magnetic structure of the particle, while on the contrary, the mesoscopic anisotropy fluctuations dominate in similar-sized Ni particles. [11] In our opinion, the SO-energy of the particle is suppressed due to the multiple surface scattering from the particle surface, similar to how the g-factors of electron in a box levels are suppressed compared to the bulk values. [81, 17, 75] Further theoretical work is needed to understand how chaotic electronic wavefunctions in a ferromagnetic

particle affect the particles's total SO-energy shift.

The magnetic shape anisotropy contribution to the total magnetic anisotropy per unit volume, $\mu_0 M_S^2/2$, varies among different metals as Ni:Py:Co:Fe=$1:2.9:7.8:11.6$, where M_S is the saturation magnetization. [49, 60] This is monotonic with the observed variation in hysteresis abundance. It suggests that the spin-orbit (SO) contribution to the total magnetic anisotropy is weaker than the shape anisotropy contribution, or what we refer to here as quenching of the SO-contribution to the anisotropy. It is remarkable that Py particles have a much higher probability to display hysteresis than Ni particles, despite the fact that bulk Py has negligibly weak magnetocrystalline anisotropy compared to Ni. It shows that the magnetocrystalline anisotropy in the bulk loses relevance in the particle.

Our conclusion about the relevance of the shape anisotropy is further supported by the measurements of the switching field. The switching field measured in single Co particles leads to an anisotropy in the particle much weaker than the bulk uniaxial magnetocrystalline anisotropy in hcp-Co. [31, 41] In our samples, the switching field at 4.2K is also monotonic with the hysteresis abundance among different particle materials: Ni: 0.12T and 0.05T in the only two samples that displayed hysteresis, and, Py: 0.114T, Co: 0.233T, and Fe: 0.257T , averaged over 5, 30, and 6 samples, respectively.

The third part of the magnetic anisotropy is the mesoscopic anisotropy, which results from nonmagnetic disorder or irregularities in the boundary of a particle.[11] It fluctuates among different electronic configurations of the particle, by an amount comparable to the single-electron anisotropy $\hbar/\tau_{SO}$, where τ_{SO} is the spin-orbit scattering time.(If SO-scattering is strong, that is, $\hbar/\tau_{SO} > \delta$, where δ is the level spacing, then the single electron anisotropy will be limited to $\sim \delta$, because of the level repulsion.) In addition, $\hbar/\tau_{SO}$ is weakly dependent among neighboring transition metals, with a typical value $\sim$ 1meV.[15] This value is consistent with the measurements

of the discontinuous shifts in energy-levels versus field at the switching field in Co particles,[19, 31, 44] and also consistent with τ_{SO} measured in Cu particles.[75] Since the single-electron anisotropy or ΔKS appears to be weakly dependent among neighboring transition metal particles, it is the total magnetic anisotropy energy or KS instead of the mesoscopic anisotropy part, that holds the responsibility for the different hysteresis abundances among neighboring transition metals.

6.3.2 Magnetization noise

The magnetization excitation caused by electron tunneling might lead to the differences in the hysteretic behaviors among different materials. In ferromagnetic particles at $T = 0$, E_M can be estimated as $\epsilon IT_1/e$, where ϵ is the typical magnetic excitation energy induced by a single electron tunneling event, I is the tunneling current, T_1 is the magnetic relaxation time, and e is the elementary charge.[44] ϵ is known to be proportional to $(\Delta K/K)^2$,[44, 45] where ΔKS is the mesoscopic anisotropy. [19, 98, 15] ΔK does not vary much among transition metals, thus for a material with a smaller K such as Ni, there will be stronger magnetization excitations due to electron tunneling, which could overcome the energy barrier and make the particle superparamagnetic.

One may argue that the main difference between Co and Ni is that Co has nuclear spin, which could introduce an additional magnetic relaxation mechanism, leading to a smaller T_1. In order to address this issue, we measured the current hysteresis loops of particles made of Ni-61 isotope with $> 90\%$ purity, which have a nuclear spin of 3/2. In Figure 6.5F, the current versus magnetic field loop of a Ni-61 sample shows MR without hysteresis. Out of 8 samples that show CB and MR, none of them exhibit hysteresis. Thus, we conclude that nuclear spin is not the main factor affecting the hysteresis abundance. Alternatively, spin might relax through the paramagnetic surface oxide layer resulting in a smaller T_1 in Co particles because Co is generally

thought to be more prone to oxidation than Ni. However, in the hysteresis measurement on Py particles which have higher resistance to oxidation than Ni particles,[20] we find that 5 out of the 10 measured Py samples exhibit hysteresis. One example is shown in Figure 6.5E, which suggests that surface oxide layer does not play a critical role in the hysteretic behavior measured in our experiments.

There is no "blocking current" below which the Ni particle restores magnetic hysteresis. The hysteresis of Ni particles is suppressed at the onset of electron transport. This could be attributed to the large CB-threshold voltage, which enables energy deposition into the magnetic subsystem at the very onset of sequential electron tunneling, leading to nonequilibrium. Alternatively, there could be noise from other sources that excites the magnetization. Further research is needed on that part.

CHAPTER 7

CONCLUSION AND FUTURE WORK

We demonstrated a technique to combine electron transport measurement of Co particles with microwave pumping. The reduction in the switching field in the presence of microwave pulses shows that the microwave pulses can pump magnetic excitations in those nanoparticles directly, without heating the leads. Repeated pulses with $\leq 10\mu$s spacing is sufficient to lower switching field, suggesting that magnetization relaxation time is in the range of a microsecond.

We conduct electron transport measurements on Co particles with various sizes at different temperatures and bias voltages. Electron tunneling through a nanometer-scale Co particle can excite nonequilibrium magnetization noise at very low temperatures. This noise can reduce the magnetic switching field as well as broaden its distribution, similar to the effect of thermal fluctuations. The noise is strongly enhanced in the vicinity of the magnetic switching field. For a given sequential tunneling current through the particle, the strength of the nonequilibrium magnetization noise at the switching field in these Co particles is weakly dependent on the size of the particle. We present a simple physical model that incorporates the magnetic anisotropy fluctuations to address the properties of that noise. In our model, the magnetic excitation energy increases linearly versus time and a steady magnetic temperature could be reached if the external magnetization relaxation mechanism is included. Numerical simulation based on the LLG equation and a quantum mechanics master equation are performed to study the magnetization dynamics in those particles and validate our model.

We perform a systematic study of Ni, Ni-61, Permalloy, and Fe particles using

electron transport measurement. Magnetic hysteresis is completely extinguished in Ni and Ni-61 particles by electron transport near zero temperature. The material dependence of the hysteresis abundance near zero temperature is monotonic with the strength of magnetic shape anisotropy of the materials; that is, while Ni, Ni-61 particles do not exhibit hysteresis at all, Py particles have much higher probability to exhibit hysteresis, while Co and Fe particles generally show hysteresis. The spin-orbit contribution to the magnetic anisotropy appears to be quenched by the irregular particle shape. Electron transport is a main source of magnetization noise.

The technique of coupling microwaves with electron transport measurement provides a possible way to study the damping in ferromagnetic particles. If a white noise instead of microwave pulses is coupled to the sample, the damping parameter of ferromagnetic particles could be estimated by corresponding the applied random magnetic field with the one obtained from magnetic thermal noise[12].

In addition to the electron tunneling induced magnetization noise, there might be other noise sources, such as the electromagnetic radiation from the electrons decoupled from the phonon bath. The model needs improvements so it can be applied to a more complex magnetic Hamiltonian. A better way to include mesoscopic fluctuations might involve adding a fluctuating MCA term in Eq. 1.10. This is a subject for future research. Devices with capacitive shunt underneath have been produced aiming to minimize the effect of the radiation. Magnetic quantum tunneling might be involved in the tunneling experiment. Further tests on those devices are still needed to draw reliable conclusions.

APPENDIX A

DATA FOR FERROMAGNETIC MATERIALS

	Fe	Co	Ni	$Ni_{80}Fe_{20}$
$2S_0/N_A$ [73]	2.10	1.65	0.67	0.96
δ_a at Fermi Level (eV/N_A)[73]	4.16	5.53	5.42	N/A
δ_i at Fermi Level (eV/N_A)[73]	1.14	1.43	0.56	N/A
No. of Spins/cm^3 (10^{22})	8.91	7.50	3.06	4.33
M_s at $T = 0$ (10^6A/m)[49, 60]	1.75	1.44	0.52	0.86
K_s at $T = 0$ (μeV/spin)[49, 60]	127.8	105.1	37.8	67.1
K_1 at $T = 300$K (μeV/spin) [49]	2.94	34.2	-1.16	0
K_2 at $T = 300$K (μeV/spin) [49]	1.05	8.33	0	0
K_1 at $T = 4.2$K (μeV/spin)	3.95[96]	64.1[72]	-24.1[26]	0
K_2 at $T = 4.2$K (μeV/spin)	1.33[96]	8.33[72]	4.1[26]	0

Here, δ_a is the majority level spacing and δ_i is the minority level spacing.

APPENDIX B

MATLAB CODE FOR MAGNETIZATION DYNAMICS

```
% This part calculate all the eigenstates and eigenenergies of the system befor
% and after tunneling
%S0 is before tunneling
S0=100;


%S01 is after tunneling
S01=S0-1/2;


%Eular Angle between the axes of MCA and MSA
phi=1/5*pi;
psi=1/5*pi;
theta=1/5*pi;
sa=sin(phi);
ca=cos(phi);
sb=sin(psi);
cb=cos(psi);
sc=sin(theta);
cc=cos(theta);
A=[cb*ca-cc*sb*sa cb*sa+ca*sb*cc sb*sc; -1*sb*ca-cc*sa*cb
-sb*sa+cc*cb*ca cb*sc; sc*sa -sc*ca cc]; % Eular rotation matrix
```

```
%Anisotropy Constant in ueV per spin
Kc=[-24.07 4.1]*0.3; %MCA before tunneling
Kc1=[-24.07 4.1]*0; %MCA after tunneling
Ksa=37.9*[0.2 0 0; 0 0.35 0 ;0 0 0.45]; %Ks*N
Ks=Ksa*A; %MSA tensor in the xyz coordinates defined by MCA

%Magnetic Field
theta1=3*pi/12;
phi1=2*pi/4;
h=0.001; %magnitude of the field in T
b=[sin(theta1)*cos(phi1) sin(theta1)*sin(phi1) cos(theta1)];



%Sx is for the spin of |S0 m> state
Sx=zeros(2*S0+1,2*S0+1);
Sz=zeros(2*S0+1,2*S0+1);
Sy=zeros(2*S0+1,2*S0+1);

%Sx1 is for the spin of |S0-1/2 m> state
Sx1=zeros(2*S0,2*S0);
Sz1=zeros(2*S0,2*S0);
Sy1=zeros(2*S0,2*S0);



%Calculate Sx, Sy, Sz
for k=-1*S0:1:S0
```

```
    for j=-1*S0:1:S0
        if j==k-1
            Sx(k+S0+1,j+S0+1)=1/2*(sqrt((S0-j)*(S0+j+1)));
            Sy(k+S0+1,j+S0+1)=-1i/2*(sqrt((S0-j)*(S0+j+1)));
        elseif j==k
            Sz(k+S0+1,j+S0+1)=k;
            Sx(k+S0+1,j+S0+1)=0;
        elseif  j==k+1
            Sx(k+S0+1,j+S0+1)=1/2*(sqrt((S0+j)*(S0-j+1)));
            Sy(k+S0+1,j+S0+1)=1i/2*(sqrt((S0+j)*(S0-j+1)));
        else Sx(k+S0+1,j+S0+1)=0;
        end
    end
end

%Calculate Sx1, Sy1, Sz1
for k=-(S01):1:(S01)
    for j=-(S01):1:(S01)
        if j==k-1
            Sx1(k+S01+1,j+S01+1)=1/2*(sqrt((S01-j)*(S01+j+1)));
            Sy1(k+S01+1,j+S01+1)=-1i/2*(sqrt((S01-j)*(S01+j+1)));
        elseif j==k
            Sz1(k+S01+1,j+S01+1)=k;
            Sx1(k+S01+1,j+S01+1)=0;
        elseif  j==k+1
            Sx1(k+S01+1,j+S01+1)=1/2*(sqrt((S01+j)*(S01-j+1)));
            Sy1(k+S01+1,j+S01+1)=1i/2*(sqrt((S01+j)*(S01-j+1)));
```

```
        else Sx1(k+S01+1,j+S01+1)=0;
        end
    end
end
Sxp=A(1,1)*Sx+A(2,1)*Sy+A(3,1)*Sz;
Syp=A(1,2)*Sx+A(2,2)*Sy+A(3,2)*Sz;
Szp=A(1,3)*Sx+A(2,3)*Sy+A(3,3)*Sz;
%Magnetocrystalline Anisotropy Energy
% before tunneling, this is an example of cubic symmetry
anic=Kc(1)/2*((Sxp*Syp)^2+(Syp*Sxp)^2+(Sxp*Szp)^2+(Szp*Sxp)^2+(Szp*Syp)^2
+(Syp*Szp)^2)/S0^3+Kc(2)*((Sxp*Syp*Szp)^2+(Syp*Sxp*Szp)^2+(Sxp*Szp*Syp)^2
+(Syp*Szp*Sxp)^2+(Szp*Sxp*Syp)^2+(Szp*Syp*Sxp)^2)/S0^5/6;


% after tunneling, this is an example of hexagonal symmetry
anic1=Kc1(1)*(Sz1*Sz1)/S0+Kc1(2)*(Sz1^4)/S0^3;


%Shape Anisotropy Energy
anis=Ks(1,1)*Sx*Sx+Ks(1,2)*(Sx*Sy+Sy*Sx)+Ks(1,3)*(Sx*Sz+Sz*Sx)
+Ks(2,2)*Sy*Sy+Ks(2,3)*(Sy*Sz+Sz*Sy)+Ks(3,3)*Sz*Sz;
% before tunneling

anis1=Ks(1,1)*Sx1*Sx1+Ks(1,2)*(Sx1*Sy1+Sy1*Sx1)+Ks(1,3)*(Sx1*Sz1+Sz1*Sx1)
+Ks(2,2)*Sy1*Sy1+Ks(2,3)*(Sy1*Sz1+Sz1*Sy1)+Ks(3,3)*Sz1*Sz1;
% after tunneling
```

```
%Calculate for the eigenstates and eigenenergy

 % before tunneling
H=-(2*h*57.89*(b(1)*Sx+b(2)*Sy+b(3)*Sz))-anic+anis/S0;

% after tunneling
H1=-(2*h*57.89*(b(1)*Sx1+b(2)*Sy1+b(3)*Sz1))-anic1+anis1/S01;

% each coloumn in V is an eigenstats of H on basis |S,SZ>
[V,D] = eig(H);

% each coloumn in V1 is an eigenstats of H1 on basis |S-1/2,SZ1>
[V1,D1] = eig(H1);
% The code above can be put in a single Matlab file.

%=============================================================================
% This part will sort the eigenstates and eigenenergies according to Sz.
SpinZ1=real(V1'*(Sz1)*V1);
SpinZ=real(V'*(Sz)*V);
SpinX1=real(V1'*(Sx1)*V1);
SpinX=real(V'*(Sx)*V);
SpinY1=real(V1'*(Sy1)*V1);
SpinY=real(V'*(Sy)*V);

SpinZ2=real(V'*(Sz*Sz)*V);
SpinX2=real(V'*(Sx*Sx)*V);
SpinY2=real(V'*(Sy*Sy)*V);
```

```
SZE=zeros(1,2*S0+1);
SZE1=zeros(1,2*S01+1);

for i=1:2*S0+1
    SZE(i)=real(SpinZ(i,i));

end
for i=1:2*S01+1

    SZE1(i)=SpinZ1(i,i);
end
[SZS,IX]=sort(SZE);
[SZS1,IX1]=sort(SZE1);

SZS=SZS';
SZS1=SZS1';

Ens=zeros(1+2*S0,1);
Ens1=zeros(1+2*S01,1);
SXS=Ens;
SYS=Ens;
SXS2=Ens;
SYS2=Ens;
SZS2=Ens;
for i=1:2*S0+1
```

```
    Ens(i)=real(D(IX(i),IX(i))); % Sorted eigenenergies of H
    SXS(i)=SpinX(IX(i),IX(i));
    SYS(i)=SpinY(IX(i),IX(i));
    SXS2(i)=SpinX2(IX(i),IX(i));
    SYS2(i)=SpinY2(IX(i),IX(i));
    SZS2(i)=SpinZ2(IX(i),IX(i));
end
SXS1=Ens1;
SYS1=Ens1;
for i=1:2*S01+1
    SXS1(i)=SpinX1(IX1(i),IX1(i));
    SYS1(i)=SpinY1(IX1(i),IX1(i));
    Ens1(i)=real(D1(IX1(i),IX1(i))); % Sorted eigenenergies of H1
end



Vs=V;
Vs1=V1;
for i=1:1+2*S0
    Vs(:,i)=V(:,IX(i));
end
for i=1:1+2*S01
    Vs1(:,i)=V1(:,IX1(i));
end
if S0==S01
    T1=Vs1'*Vs;
    T2=T.*conj(T);
```

```
end
% Now the first one is the max Sz which is the ground state of the particle
% The code above can be put in a single Matlab file.



%=========================================================================
% This part calculate the C.G. for |1/2 1/2>|G> (CGP)
% and  |1/2 -1/2>|G> (CGN) on the
% basis |S0-1/2 m>, and magnetic tunneling matrix elements
CGN=zeros(2*S01+1,1);
CGP=zeros(2*S01+1,1);
for m=-(S0-1):1:(S0)
    %  m'=m-1/2 So it is m'= -(S0-1/2):1:(S0-1/2)
    CGN(m+S0)=((S0+m)/(2*S0+1))^0.5;
    CGP(m+S0)=-((S0-m+1)/(2*S0+1))^0.5;
end
TP=zeros(2*S01+1,2*S0+1);
TN=zeros(2*S01+1,2*S0+1);
Vs=V;
Vs1=V1;
for i=1:1+2*S0
    Vs(:,i)=V(:,IX(i));
end
for i=1:1+2*S01
    Vs1(:,i)=conj(V1(:,IX1(i)));
end
```

```
for p=1:1:1+2*S0
    for m=-(S01):1:(S01)
        for j=-(S01):1:(S01)
            TN(m+S01+1,p)=TN(m+S01+1,p)
+Vs(j+S01+2,p)*Vs1(j+S01+1,m+S01+1)*CGN(j+S01+1);

            TP(m+S01+1,p)=TP(m+S01+1,p)
+Vs(j+S01+1,p)*Vs1(j+S01+1,m+S01+1)*CGP(j+S01+1);

        end
    end
end
TP2=TP.*conj(TP);
TN2=TN.*conj(TN);
T=TP2+TN2;
%T is the tunneling matrix element for the master equation.
%T(i,j) meaning the tunneling probability from the
%ith state of H to the jth state of H1.

% The code above can be put in a single Matlab file.
%================================================================================



%This parts is the simulation of magnetization dynamics using master equition
dt=1e-9;   %size of time step
t=0:dt:2e-6; % the total time of the run
```

```
%t=t';
num=2*S0;
bar=1e-8;
Tt=T(1:num,1:num+1);

u=30000; % the energy level that electron is tunneling through

% Fermi level of left lead, should be higher than the energy levels,can be an a
uL=70000;
T1=zeros(length(uL),1);
uR=0;  % Fermi level of right lead, grounded
ktemp=0.1; %energy of the thermal fluctuations
RL=6e7; %tunneling rate of left lead
RR=6e7; %tunneling rate of right lead
dP=zeros(1,num+1);
dQ=zeros(1,num);

%coupling to Boson bath, does not work at this time
gB=25;

%Intrinsic Relaxation,does not work at this time
% t1=1e6;
% Rex=(1:2*S0+1)/t1;
% Rex1=(1:2*S01+1)/t1;

%calculation of histogram
Edt=0*zeros((2*S01+1)*(2*S0+1),1);
```

```
Pdt=0*zeros((2*S01+1)*(2*S0+1),1);
Et=T*0;
k=1;
for i=1:2*S0+1;
    for j=1:2*S01+1
        Edt(k)=Ens1(j)-Ens(i);
        Pdt(k)=Tt(j,i);
        k=k+1;
        Et(j,i)=Ens1(j)-Ens(i);
    end
end
[Eds,EIX]=sort(Edt);
step=20;    %stepsize between bins
Bins=[-1500:step:1000 1000+step]'; % bins of histogram, can be set accordingly
numb=length(Bins);
Hist=zeros(length(t),numb); % histogram
Pds=Pdt(EIX);

for x=1:length(uL)
    P=zeros(length(t),num+1); % the probability distribution over H states
    Q=zeros(length(t),num);   % the probability distribution over H1 states
    P(1,1)=1;
    %     P=Pinitial;
    %     Q=Qinitial;
    fL=Tt;
    fR=Tt;
    v=1;
```

```
for u=1:length(Eds)
    if Eds(u)<=Bins(v)+step/2
        Hist(1,v)=Hist(1,v)+Pds(u);
    elseif v==numb
        Hist(1,v)=Hist(1,v)+Pds(u);
    else
        v=v+1;
        Hist(1,v)=Hist(1,v)+Pds(u);
    end
end
%find fL and fR
for j=1:num+1

    for i=1:num
        fL(i,j)=1/(exp((Ens1(i)-Ens(j)+u-uL(x))/ktemp)+1);
        fR(i,j)=1/(exp((Ens1(i)-Ens(j)+u-uR)/ktemp)+1);
    end

end

%calculate S+/S- matrix
Splus=Vs'*(Sx+1i*Sy)*Vs;
Splus2=Splus.*conj(Splus);

%Sminus=Vs'*(Sx-1i*Sy)*Vs;
Sminus2=Splus2';
```

```
%calculate S1+/S1- matrix
Vs1=conj(Vs1);
S1plus=Vs1'*(Sx1+1i*Sy1)*Vs1;
S1plus2=S1plus.*conj(S1plus);
S1minus2=S1plus2';

%calculate Boson Distribution
Bp=Splus;
for i=1:num+1
    for j=1:num+1
        Bp(i,j)=1/(exp((Ens(i)-Ens(j))/ktemp)-1);
        %           if Bp(i,j)^2<1e-10
        %               Bp(i,j)=0;
        %           end

        if i==j
            Bp(i,j)=0;
        end
    end
end
Bn=Bp';

Bp1=S1plus;
for i=1:num
    for j=1:num
        Bp1(i,j)=1/(exp((Ens1(i)-Ens1(j))/ktemp)-1);
```

```
        %           if Bp1(i,j)^2<1e-10
        %               Bp1(i,j)=0;
        %           end
        if i==j
            Bp1(i,j)=0;
        end
    end
end
Bn1=Bp1';

%calculate boson energy spectra
pB=Bn;
for i=1:num+1
    for j=1:num+1
        pB(i,j)=1;
    end
end

pB1=Bn1;
for i=1:num
    for j=1:num
        pB1(i,j)=1;
    end
end

TfL=RL*times(Tt,fL);
TfLa=RL*times(Tt,1-fL);
```

```
TfR=RR*times(Tt,fR);
TfRa=RR*times(Tt,1-fR);
Tf=TfL+TfR;
Tfa=TfLa+TfRa;
Stn=((-Splus2.*pB).*Bp+(Sminus2.*pB').*Bp);
Stp=-Stn';
%         Stpa=-Stna';
%         Stpb=-Stnb';
Stn1=((-S1plus2.*pB1).*Bn1+(S1minus2.*pB1').*Bn1);
%    Stp1=((-S1plus2.*pB1).*Bp1+(S1minus2.*pB1').*Bp1)*pi*gB^2;
Stp1=-Stn1';
Stpp=Stp;
Stpq=Stp1;
for s=2:length(t)
    for i=1:num+1
        Stpp(i,:)=times(Stp(i,:),P(s-1,:));
    end

    for i=1:num
        Stpq(i,:)=times(Stp1(i,:),Q(s-1,:));
    end

    %         Stpp=int64(floor(Stpp*2^40));
    %         Stpq=int64(floor(Stpq*2^40));
    %         Stppm=Stpp;
    %         Stpp=Stpp/2;
    %         Stpq=Stpq/2;
```

```
%          Stpp=Stpp*2;
%          Stpq=Stpq*2;
%          Stpp=double(Stpp);
%          Stpq=double(Stpq);
%          Stpp=Stpp/2^40;
%          Stpq=Stpq/2^40;

        dP=dt*(-times(P(s-1,:),sum(Tf))+Q(s-1,:)*Tfa
+pi*gB^2*((-sum(Stpp,2))'+(sum(Stpp))));

        dQ=dt*((P(s-1,:)*Tf')-times(Q(s-1,:),sum(transpose(Tfa)))
+pi*gB^2*((-sum(Stpq,2))'+(sum(Stpq))));

        P(s,:)=P(s-1,:)+dP; % the probability distribution over H states
        Q(s,:)=Q(s-1,:)+dQ; % the probability distribution over H1 states

        %    %This part give the evolution of  the Historgram, uncomment to tur
        %          k=1;
        %          Et=T*0;
        %          for u=1:2*S0+1;
        %              for v=1:2*S01+1
        %                  Pdt(k)=T(v,u)*P(s,u);
        %                  k=k+1;
        %              end
        %          end
        %          Pds=Pdt(EIX);
        %
```

```
        %         v=1;
        %         for u=1:length(Eds)
        %             if Eds(u)<=Bins(v)+step/2
        %                 Hist(s,v)=Hist(s,v)+Pds(u);
        %             elseif v==numb
        %                 Hist(s,v)=Hist(s,v)+Pds(u);
        %             else
        %                 v=v+1;
        %                 Hist(s,v)=Hist(s,v)+Pds(u);
        %             end
        %         end
        %
        %
        %
        %
    end
    Eem=P*(Ens(1:num+1)-Ens(6))+Q*(Ens1(1:num)-Ens1(14)); %magnetic energy
    m=P*(SZS)+Q*(SZS1); %the averaged Sz
end
```

REFERENCES

[1] Averin, D. V. and Korotkov, A. N., "Correlated single-electron tunneling via mesoscopic metal particles - effects of the energy quantization," *Journal of low temperature physics*, vol. 80, p. 173, 1990.

[2] Averin, D. V., Korotkov, A. N., and Likharev, K. K., "Theory of single-electron charging of quantum wells and dots," *Phys. Rev. B*, vol. 44, p. 6199, 1991.

[3] Baibich, M. N., Broto, J. M., Fert, A., Van Dau, F. N., Petroff, F., Etienne, P., Creuzet, G., Friederich, A., and Chazelas, J., "Giant magnetoresistance of (001)fe/(001)cr magnetic superlattices," *Phys. Rev. Lett.*, vol. 61, pp. 2472–2475, 1988.

[4] Basko, D. M. and Vavilov, M. G., "Stochastic dynamics of magnetization in a ferromagnetic nanoparticle out of equilibrium," *Phys. Rev. B*, vol. 79, p. 064418, Feb 2009.

[5] Beenakker, C. W. J., "Theory of columb-blockade oscillations in the conductance of a quantum dot," *Phys. Rev. B*, vol. 44, p. 1646, 1991.

[6] Beleggia, M., De Graef, M., and Millev, Y., "Demagnetization factors of the general ellipsoid: An alternative to the maxwell approach," *Philosophical Magazine*, vol. 86, no. 16, pp. 2451–2466, 2006.

[7] Berger, L., "Emission of spin waves by a magnetic multilayer traversed by a current," *Phys. Rev. B*, vol. 54, pp. 9353–9358, 1996.

[8] Bernand-Mantel, A., Seneor, P., Bouzehouane, K., Fusil, S., Deranlot, C., Petroff, F., and Fert, A., "Anisotropic magneto-Coulomb effects and magnetic single-electron-transistor action in a single nanoparticle," *Nature Phys.*, vol. 5, p. 920, DEC 2009.

[9] Brouwer, P. W., Waintal, X., and Halperin, B. I., "Fluctuating spin g-tensor in small metal grains," *Phys. Rev. Lett.*, vol. 85, p. 369, 2000.

[10] Brouwer, P. W. and Waintall, X. *Phys. Rev. Lett.*, vol. 85, p. 369, 2000.

[11] Brouwer, P. W. and Gorokhov, D. A., "Bound on anisotropy in itinerant ferromagnets from random impurities," *Phys. Rev. Lett.*, vol. 95, p. 017202, Jun 2005.

[12] Brown, W. F., "Thermal fluctuations of a single-domain particle," *Phys. Rev.*, vol. 130, pp. 1677–1686, 1963.

[13] Burzurí, E., Zyazin, A. S., Cornia, A., and van der Zant, H. S. J., "Direct observation of magnetic anisotropy in an individual fe_4 single-molecule magnet," *Phys. Rev. Lett.*, vol. 109, p. 147203, Oct 2012.

[14] Canali, C. M. and MacDonald, A. H., "Theory of tunneling spectroscopy in ferromagnetic nanoparticles," *Phys. Rev. Lett.*, vol. 85, p. 5623, 2000.

[15] Cehovin, A., Canali, C. M., and MacDonald, A. H., "Magnetization orientation dependence of the quasiparticle spectrum and hysteresis in ferromagnetic metal nanoparticles," *Phys. Rev. B*, vol. 66, p. 094430, Sep 2002.

[16] Cehovin, A., Canali, C. M., and MacDonald, A. H., "Elementary excitations of ferromagnetic metal nanoparticles," *Phys. Rev. B*, vol. 68, p. 014423, Jul 2003.

[17] Davidović, D. and Tinkham, M., "Spectroscopy, interactions, and level splittings in an nanoparticles," *Phys. Rev. Lett.*, vol. 83, pp. 1644–1647, 1999.

[18] Deshmukh, M. M., E, E. B., Pasupathy, A. N., and Ralph, D. C., "Equilibrium and nonequilibrium electron tunneling via discrete quantum states," *Phys. Rev. B*, vol. 65, p. 073301, 2002.

[19] Deshmukh, M. M., Kleff, S., Gueron, S., Bonet, E., Pasupathy, A. N., von Delft, J., and Ralph, D. C., "Magnetic anisotropy variations and nonequilibrium tunneling in a cobalt nanoparticle," *Phys. Rev. Lett*, vol. 87, p. 226801, 2001.

[20] Dong, X., Zhang, Z., Zhao, X., Chuang, Y., Jin, S., Sun, W., and others, "The preparation and characterization of ultrafine fe-ni particles," *JOURNAL OF MATERIALS RESEARCH-PITTSBURGH-*, vol. 14, pp. 398–406, 1999.

[21] Duan, C.-G., Velev, J. P., Sabirianov, R. F., Zhu, Z., Chu, J., Jaswal, S. S., and Tsymbal, E. Y., "Surface magnetoelectric effect in ferromagnetic metal films," *Phys. Rev. Lett.*, vol. 101, p. 137201, Sep 2008.

[22] Fonseca, F. C., Goya, G. F., Jardim, R. F., Muccillo, R., Carreño, N. L. V., Longo, E., and Leite, E. R., "Superparamagnetism and magnetic properties of ni nanoparticles embedded in sio_2," *Phys. Rev. B*, vol. 66, p. 104406, Sep 2002.

[23] Foros, J., Brataas, A., Tserkovnyak, Y., and Bauer, G. E. W., "Magnetization noise in magnetoelectronic nanostructures," *Phys. Rev. Lett.*, vol. 95, p. 016601, 2005.

[24] Friedman, J. R., Sarachik, M. P., Tejada, J., and Ziolo, R., "Macroscopic measurement of resonant magnetization tunneling in high-spin molecules," *Phys. Rev. Lett.*, vol. 76, p. 3830, 1996.

[25] Fukushima, A., Sato, A., Iwasa, A., Nakamura, Y., Komatsuzaki, T., and Sakamoto, Y., "Attenuation of microwave filters for single-electron tunneling experiments," *Instrumentation and Measurement, IEEE Transactions on*, vol. 46, pp. 289–293, Apr 1997.

[26] Gadsden, C. and Heath, M., "The first three anisotropy constants of nickel," *Solid State Commun.*, vol. 20, no. 10, pp. 951 – 952, 1976.

[27] Garg, A., "Escape-field distribution for esacape from a metastable potential well subject to a steadily increasing bias field," *Phys. Rev. B*, vol. 51, pp. 15592–15595, 1995.

[28] Gittleman, J. I., Abeles, B., and Bozowski, S., "Superparamagnetism and relaxation effects in granular ni-sio$_2$ and ni-al$_2$o$_3$ films," *Phys. Rev. B*, vol. 9, p. 3891, 1974.

[29] Grose, J. E., Tam, E. S., Timm, C., Scheloske, M., Ulgut, B., Parks, J. J., Abruna, H. D., Harneit, W., and Ralph, D. C., "Tunnelling spectra of individual magnetic endofullerene molecules," *Nat. Mater.*, vol. 7, pp. 884–889, 2008.

[30] Grünberg, P., Schreiber, R., Pang, Y., Brodsky, M. B., and Sowers, H., "Layered magnetic structures: Evidence for antiferromagnetic coupling of fe layers across cr interlayers," *Phys. Rev. Lett.*, vol. 57, p. 2442, 1986.

[31] Gueron, S., Deshmukh, M. M., Myers, E. B., and Ralph, D. C., "Tunneling via individual electronic states in ferromagnetic nanoparticles," *Phys. Rev. Lett.*, vol. 83, p. 4148, 1999.

[32] Gunther, L. and Barbara, B., "Quantum tunneling across a domain-wall junction," *Phys. Rev. B*, vol. 49, pp. 3926–3933, 1994.

[33] Hall, D. B., Underhill, P., and Torkelson, J. M., "Spin coating of thin and ultrathin polymer films," *Polymer Engineering & Science*, vol. 38, no. 12, pp. 2039–2045, 1998.

[34] Hanson, R., Kouwenhoven, L. P., Petta, J. R., Tarucha, S., and Vandersypen, L. M. K., "Spins in few-electron quantum dots," *Rev. Mod. Phys.*, vol. 79, pp. 1217–1265, Oct 2007.

[35] Heersche, H. B., de Groot, Z., Folk, J. A., van der Zant, H. S. J., Romeike, C., Wegewijs, M. R., Zobbi, L., Barreca, D., Tondello, E., and Cornia, A., "Electron transport through single $mn12$ molecular magnets," *Phys. Rev. Lett.*, vol. 96, p. 206801, May 2006.

[36] Heinrich, B., "Spin relaxation in magnetic metallic layers and multilayers," in *Ultrathin Magnetic Structures III Fundamentals of Nanomagnetism* (Bland, J. A. C. and Heinrich, B., eds.), pp. 143–210, Springer-Verlag, 2005.

[37] Heinrich, B., Urban, R., and Woltersdorf, G., "Magnetic relaxation in metallic films: Single and multilayer structures," *Journal of Applied Physics*, vol. 91, no. 10, pp. 7523–7525, 2002.

[38] Šimánek, E. and Heinrich, B., "Gilbert damping in magnetic multilayers," *Phys. Rev. B*, vol. 67, p. 144418, Apr 2003.

[39] Žutić, I., Fabian, J., and Das Sarma, S., "Spintronics: Fundamentals and applications," *Rev. Mod. Phys.*, vol. 76, pp. 323–410, 2004.

[40] J. C. Nabity Lithography Systems, *Nanometer Pattern Generation System*.

[41] Jamet, M., Wernsdorfer, W., Thirion, C., Mailly, D., Dupuis, V., Méinon, P., and Pérez, A., "Magnetization reversal of a 1000-atoms cobalt cluster," *Journal of Magnetism and Magnetic Materials*, vol. 226-230, pp. 1833 – 1834, 2001.

[42] Jamet, M., Wernsdorfer, W., Thirion, C., Dupuis, V., Mélinon, P., Pérez, A., and Mailly, D., "Magnetic anisotropy in single clusters," *Phys. Rev. B*, vol. 69, p. 024401, 2004.

[43] Jiang, W., Birk, F. T., and Davidovic, D., "Microwave coupled electron tunneling measurement of co nanoparticles," *Appl. Phys. Lett.*, vol. 99, p. 032510, 2011.

[44] Jiang, W., Birk, F. T., and Davidovic, D., "Effects of confinement and electron transport on magnetic switching in single co nanoparticles," *Sci. Rep.*, vol. 3, p. 1200, 2013.

[45] Jiang, W., Gartland, P., and Davidović, D., "Size-dependence of magneto-electronic coupling in co nanoparticles," *J. Appl. Phys.*, vol. 113, no. 22, p. 223703, 2013.

[46] Jo, M.-H., Grose, J. E., Baheti, K., Deshmukh, M. M., Sokol, J. J., Rumberger, E. M., Hendrickson, D. N., Long, J. R., Park, H., and Ralph, D. C., "Signatures of molecular magnetism in single-molecule transport spectroscopy," *Nano Lett.*, vol. 6, pp. 2014–2020, 2006.

[47] Julliere, M., "Tunnelling between ferromagnetic films," *Phys. Lett. A*, vol. 54, pp. 225–226, 1975.

[48] Katine, J. A., Albert, F. J., Buhrman, R. A., Myers, E. B., and Ralph, D. C., "Current-driven magnetization reversal and spin-wave excitations in co /cu /co pillars," *Phys. Rev. Lett.*, vol. 84, p. 3149, 2000.

[49] Kittel, C., *Introduction to Solid State Physics*. Wiley, 2004.

[50] Kleff, S., Delft, J. v., Deshmukh, M. M., and Ralph, D. C., "Model for ferromagnetic nanograins with discrete electronic states," *Phys. Rev. B*, vol. 64, p. 220401, 2001.

[51] Kleff, S. and von Delft, J., "Nonequilibrium excitations in ferromagnetic nanoparticles," *Phys. Rev. B*, vol. 65, p. 214421, Jun 2002.

[52] Kouwenhoven, L. P., Marcus, C., McEuen, P., Tarucha, S., Westervelt, R., and Wingreen, N. in *Mesoscopic Electron Transport* (Kouwenhoven, L. P., Sohn, L. L., and Schon, G., eds.), p. 549, Elsevier and Amsterdam, 1997.

[53] Kurkijärvi, J., "Intrinsic fluctuations in a superconducting ring closed with a josephson junction," *Phys. Rev. B*, vol. 6, pp. 832–835, Aug 1972.

[54] Lederman, M., Schultz, S., and Ozaki, M., "Measurement of the dynamics of the magnetization reversal in individual single-domain ferromagnetic particles," *Phys. Rev. Lett.*, vol. 73, pp. 1986–1989, 1994.

[55] Lopez-Diaz, L., Torres, L., and Moro, E., "Transition from ferromagnetism to superparamagnetism on the nanosecond time scale," *Phys. Rev. B*, vol. 65, p. 224406, May 2002.

[56] Lounasmaa, O. V., *Experimental principles and methods below 1 K.* Academic Press, 1974.

[57] Luis, F., Petroff, F., Torres, J. M., García, L. M., Bartolomé, J., Carrey, J., and Vaurès, A., "Magnetic relaxation of interacting co clusters: Crossover from two- to three-dimensional lattices," *Phys. Rev. Lett.*, vol. 88, p. 217205, May 2002.

[58] Malec, C. E., *Transport in graphene tunnel junctions.* PhD thesis, School of Physics, Georgia Institute of Technology, August 2011.

[59] Mannini, M., Pineider, F., Sainctavit, P., Danieli, C., Otero, E., Sciancalepore, C., Talarico, A. M., Arrio, M.-A., Cornia, A., Gatteschi, D., and Sessoli, R., "Magnetic memory of a single-molecule quantum magnet wired to a gold surface," *Nat. Mater.*, vol. 8, pp. 194–197, 2009.

[60] Martinez, E., Lopez-Diaz, L., Torres, L., and Garcia-Cervera, C., "Thermal activation in permalloy nanorectangles at room temperature," *Physica B: Condensed Matter*, vol. 372, pp. 286 – 289, 2006.

[61] Maruyama, T., Shiota, Y., Nozaki, T., Ohta, K., Toda, N., Mizuguchi, M., Tulapurkar, A. A., Shinjo, T., Shiraishi, M., Mizukami, S., Ando, Y., and Suzuki, Y., "Large voltage-induced magnetic anisotropy change in a few atomic layers of iron," *Nature Nanotechnology*, vol. 4, no. March, p. 158, 2009.

[62] Michalak, L., Canali, C. M., and Benza, V. G., "Electron-magnon coupling and nonlinear tunneling transport in magnetic nanoparticles," *Phys. Rev. Lett.*, vol. 97, p. 096804, 2006.

[63] Miyazaki, T. and Tezuka, N., "Giant magnetic tunneling effect in fe/al2o3/fe junction," *J. Magn. Magn. Matter.*, vol. 139, pp. 231 – 234, 1995.

[64] Myers, E. B., Ralph, D. C., Katine, J. A., Louie, R. N., and Buhrman, R. A., "Current-induced switching of domains in magnetic multilayer devices," *Science*, vol. 285, pp. 867–870, 1999.

[65] Néel, L., "Théorie du traînage magnétique des ferromagnétiques en grains fins avec applications aux terres cuites," *Ann. Géophys*, vol. 5, p. 99, 1949.

[66] Núñez, A. S. and Duine, R. A., "Effective temperature and gilbert damping of a current-driven localized spin," *Phys. Rev. B*, vol. 77, p. 054401, Feb 2008.

[67] Ono, K., Shimada, H., Kobayashi, S., and Outuka, Y., "Magnetoresistance of ni/nio/co small tunnel junctions in coulomb blockade regime," *Journal of the physical society of Japan*, vol. 65, p. 3449, 1996.

[68] Ono, K., Shimada, H., and Outuka, Y., "Enhanced magnetic valve effect and magneto-coulomb oscillations in ferromagnetic single electron transistor," *Journal of the physical society of Japan*, vol. 66, p. 1261, 1997.

[69] Orozco, E. B., Wernsdorfer, W., Barbara, B., Benoît, A., Mailly, D., and Thiaville, A., "Uniform rotation of magnetization measured in single nanometer-sized particles," *J. Appl. Phys*, vol. 87, pp. 5097–5098, 2000.

[70] Orozco, E., Wernsdorfer, W., Barbara, B., Hasselbach, K., Benoit, A., and Mailly, D., "Single particle measurement showing agreement with the model of uniform rotation," *Magnetics, IEEE Transactions on*, vol. 34, pp. 979–981, 1998.

[71] Oxford Instruments, *Operator's Handbook*.

[72] Paige, D., Szpunar, B., and Tanner, B., "The magnetocrystalline anisotropy of cobalt," *J. Magn. Magn. Mater.*, vol. 44, no. 3, pp. 239 – 248, 1984.

[73] Papaconstantopoulos, D., *Handbook of the band structure of elemental solids*. Plenum Press New York, 1986.

[74] Parcollet, O. and Waintal, X., "Spin torque in a nanomagnet coupled to noncollinear ferromagnetic electrodes," *Phys. Rev. B*, vol. 73, p. 144420, Apr 2006.

[75] Petta, J. R. and Ralph, D. C., "Studies of spin-orbit scattering in noble-metal nanoparticles using energy-level tunneling spectroscopy," *Phys. Rev. Lett.*, vol. 87, p. 266801, 2001.

[76] Ralph, D. C., Black, C. T., and Tinkham, M., "Spectroscopic measurements of discrete electronic states in single metal particles," *Phys. Rev. Lett.*, vol. 74, p. 3241, 1995.

[77] Rebei, A. and Parker, G. J., "Fluctuations and dissipation of coherent magnetization," *Phys. Rev. B*, vol. 67, p. 104434, Mar 2003.

[78] Richardson, R. C. and Smith, E. N., *Experimental Techniques In Condensed Matter Physics At Low Temperatures*. Addison-Wesley, 1998.

[79] Rossi, E., Heinonen, O. G., and MacDonald, A. H., "Dynamics of magnetization coupled to a thermal bath of elastic modes," *Phys. Rev. B*, vol. 72, p. 174412, Nov 2005.

[80] Roukes, M. L., Freeman, M. R., Germain, R. S., Richardson, R. C., and Ketchen, M. B., "Hot electrons and energy transport in metals at millikelvin temperatures," *Phys. Rev. Lett.*, vol. 55, pp. 422–425, Jul 1985.

[81] Salinas, D. G., Gueron, S., Ralph, D. C., Black, C. T., and Tinkham, M., "Effects of spin-orbit interactions on tunneling via discrete energy levels in metal nanoparticles," *Phys. Rev. B*, vol. 60, p. 6137, 1999.

[82] Sarkar, A., Kapoor, S., Yashwant, G., Salunke, H. G., and Mukherjee, T., "Preparation and characterization of ultrafine co and ni particles in a polymer matrix," *The Journal of Physical Chemistry B*, vol. 109, no. 15, pp. 7203–7207, 2005.

[83] Shimada, H., Ono, K., and Ootuka, Y., "Magneto-coulomb oscillation in ferromagnetic single electron transistors," *J. Phys. Soc. Jpn*, vol. 67, p. 1359, 1998.

[84] Slonczewski, J. C., "Conductance and exchange coupling of two ferromagnets separated by a tunneling barrier," *Phys. Rev. B*, vol. 39, p. 6995, 1989.

[85] Slonczewski, J. C., "Current-driven excitation of magnetic multilayers," *Journal of Magnetism and Manetic Materials*, vol. 159, pp. L1–L7, 1996.

[86] Smith, N., "Modeling of thermal magnetization fluctuations in thin-film magnetic devices," *Journal of Applied Physics*, vol. 90, no. 11, pp. 5768–5773, 2001.

[87] Stiles, M. D., Halilov, S. V., Hyman, R. A., and Zangwill, A., "Spin-other-orbit interaction and magnetocrystalline anisotropy," *Phys. Rev. B*, vol. 64, p. 104430, Aug 2001.

[88] Stoner, E. C. and Wohlfarth, E. P., "A mechanism of magnetic hysteresis in heterogeneous alloys," *Philosophical Transactions of the Royal Society of London. Series A, Mathematical and Physical Sciences*, vol. 240, no. 826, pp. 599–642, 1948.

[89] Sun, J., "Current-driven magnetic switching in manganite trilayer junctions," *J. Magn. Magn. Matter.*, vol. 202, p. 157, 1999.

[90] Tamion, A., Raufast, C., Orozco, E. B., Dupuis, V., Fournier, T., Crozes, T., Bernstein, E., and Wernsdorfer, W., "Magnetization reversal of a single cobalt cluster using a rf field pulse," *J. Magn. Magn. Mater.*, vol. 322, p. 1315, 2010.

[91] Thirion, C., Wernsdorfer, W., and Mailly, D., "Switching of magnetization by nonlinear resonance studied in single nanoparticles," *Nature Mater.*, vol. 2, p. 524, 2003.

[92] Thomas, L., Lionti, F., Ballou, R., Gatteschi, D., Sessoli, R., and Barbara, B., "Macroscopic quantum tunnelling of magnetization in a single crystal of nanomagnets," *Nature*, vol. 383, p. 145, 1996.

[93] Tijiwa Birk, F., *Spin electronics in metallic nanoparticles*. PhD thesis, School of Physics, Georgia Institute of Technology, March 2011.

[94] Tsoi, M., Jansen, A. G. M., Bass, J., Chiang, W.-C., Seck, M., Tsoi, V., and Wyder, P., "Excitation of a magnetic multilayer by an electric current," *Phys. Rev. Lett.*, vol. 80, p. 4281, 1998.

[95] Tsujikawa, M. and Oda, T., "Finite electric field effects in the large perpendicular magnetic anisotropy surface Pt/Fe/Pt(001): A first-principles study," *Phys. Rev. Lett.*, vol. 102, p. 247203, Jun 2009.

[96] Tung, C., Said, I., and Everett, G. E., "Magnetic anisotropy constants of fe and ni at 77, 4.2, and 1.09 k: Interdomain configuration transitions in ni," *J. Appl. Phys*, vol. 53, no. 3, pp. 2044–2046, 1982.

[97] Urban, R., Woltersdorf, G., and Heinrich, B., "Gilbert damping in single and multilayer ultrathin films: Role of interfaces in nonlocal spin dynamics," *Phys. Rev. Lett.*, vol. 87, p. 217204, Nov 2001.

[98] Usaj, G. and Baranger, H. U., "Anisotropy in ferromagnetic nanoparticles: Level-to-level fluctuations of a collective effect," *Europhys. Lett.*, vol. 72, no. 1, p. 110, 2005.

[99] van der Molen, S. J., Tombros, N., and van Wees, B. J., "Magnetocoulomb effect in spin-valve devices," *Phys. Rev. B*, vol. 73, p. 220406, Jun 2006.

[100] Victora, R. H., "Predicted time-dependence of the switching field for magnetic-materials," *Phys. Rev. Lett.*, vol. 63, pp. 457–460, 1989.

[101] Waintal, X. and Parcollet, O., "Current-induced spin torque in a nanomagnet," *Phys. Rev. Lett.*, vol. 94, p. 247206, 2005.

[102] Waintal, X. and Brouwer, P. W., "Tunable magnetic relaxation mechanism in magnetic nanoparticles," *Phys. Rev. Lett.*, vol. 91, p. 247201, 2003.

[103] Washburn, S. and Webb, R. A., "Quantum transport in small disordered samples from the diffusive to the ballistic regime," *Rep. Prog. Phys.*, vol. 55, p. 1311, 1992.

[104] Wei, Y. G., Malec, C. E., and Davidovic, D., "Saturation of spin-polarized current in nanometer scale aluminum grains," *Phys. Rev. B*, vol. 76, p. 195327, 2007.

[105] Weisheit, M., Fähler, S., Marty, A., Souche, Y., Poinsignon, C., and Givord, D., "Electric field-induced modification of magnetism in thin-film ferromagnets.," *Science*, vol. 315, p. 349, January 2007.

[106] Wernsdorfer, W., Orozco, E. B., Hasselbach, K., Benoit, A., Barbara, B., Demoncy, N., Loiseau, A., Pascard, H., and Mailly, D., "Experimental evidence of the néel-brown model of magnetization reversal," *Phys. Rev. Lett.*, vol. 78, pp. 1791–1794, 1997.

[107] Wernsdorfer, W. and Sessoli, R., "Quantum phase interference and parity effects in magnetic molecular clusters," *Science*, vol. 284, pp. 133–135, 1999.

[108] Wolf, S. A., Awschalom, D. D., Buhrman, R. A., Daughton, J. M., von Molnar, S., Roukes, M. L., Chtchelkanova, A. Y., and Treger, D. M., "Spintronics: A spin-based electronics vision for the future," *Science*, vol. 294, p. 1488, 2001.

[109] Yakushiji, K., Ernult, F., Imamura, H., Yamane, K., Mitani, S., Takanashi, K., Maekawa, S., and Fujimori, H., "Enhanced spin accumulation and novel magnetotransport in nanoparticles," *Nature Mater.*, vol. 4, p. 57, 2005.

[110] Yakushiji, K., Mitani, S., Takanashi, K., Takahashi, S., Maekawa, S., Imamura, H., and Fujimori, H., "Enhanced tunnel magnetoresistance in granular nanobridges," *Appl. Phys. Lett.*, vol. 78, p. 515, 2001.

[111] Yoon, M., Kim, Y., Kim, Y., Volkov, V., Song, H., Park, Y., and Park, I.-W., "Superparamagnetic properties of nickel nanoparticles in an ion-exchange polymer film," *Materials Chemistry and Physics*, vol. 91, no. 1, pp. 104 – 107, 2005.

[112] Zhang, S. and Zhang, S. S.-L., "Generalization of the landau-lifshitz-gilbert equation for conducting ferromagnets," *Phys. Rev. Lett.*, vol. 102, p. 086601, Feb 2009.

[113] Zyazin, A. S., van den Berg, J. W., Osorio, E. A., van der Zant, H. S., Konstantinidis, N. P., Leijnse, M., Wegewijs, M. R., May, F., Hofstetter, W., Danieli, C., and others, "Electric field controlled magnetic anisotropy in a single molecule," *Nano Lett.*, vol. 10, no. 9, pp. 3307–3311, 2010.

VITA

Wenchao Jiang was born in a small city named Lianyungang on the east coast of China in 1987. He spent 18 peaceful years in that city, which is also known as the hometown of the "Monkey King". He went to Fudan University in Shanghai to start his adventure in science. After graduating from Fudan University with a B.S. in physics in 2009, he moved to Atlanta, Georgia for his PhD program in Georgia Institute of Technology.

In Georgia Tech, he joined Professor Dragomir Davidovic's lab to study the quantum mechanical phenomena in ferromagnetic nanoparticles. His skills and knowledge were test in 2014 after which he was granted a PhD degree.